Development of a process for characterization of Nd:YAG crystals

A Thesis
Submitted to the Faculty
of the

Worcester Polytechnic Institute

in partial fulfillment of the requirements for the
Degree of Master of Science
in
Mechanical Engineering

by

Mark T. Bronski

January 20 2003

Approved:

Prof. Ryszard J. Pryputniewicz, Major Advisor

Prof. Richard D. Sisson, Member, Thesis Committee

Prof. Raymond R. Hagglund, Member, Thesis Committee

Prof. Cosme Furlong, Member, Thesis Committee

Dr. Holger Schlueter, TRUMPF Inc., Farmington, CT, Member, Thesis Committee

Prof. John M. Sullivan, Graduate Committee Representative

SUMMARY

The objectives of this thesis were to develop a methodology for the measurement of laser beam characteristics from a single cavity laser and to establish a preliminary guideline that would determine which crystals were acceptable for use in production of laser devices. These objectives were achieved by developing the experimental procedures and by statistical analysis of the data obtained. However, additional future work is needed to independently confirm the results of this thesis.

Efficient and reliable operation of a lamp-pumped Nd:YAG laser is highly dependent on the crystal from which the beam is derived. However little attention is given to the quality of the laser beam produced by each crystal. Although many factors influence the output beam, the power dependent focal length is of particular importance. Unfortunately, direct measurement of the crystal focal length is not possible with a Nd:YAG laser beam. This is because the single cavity laser functions as both a resonator and amplifier simultaneously. Therefore, a method was developed that measured the caustic of the laser beam after it had emerged from the resonator and been focused by means of a focusing element. The caustic of the beam was analyzed utilizing a beam analyzer that calculated the beam focusability factor and the beam waist size. From this information, the waist diameter at the outcoupler mirror was calculated using Gaussian beam propagation principles. A resonator model was developed based on the self-repeating ABCD matrix that allowed for the determination of the induced thermal lens based on the input power. Several approaches to model the thermal lensing effect were taken, each with increasing complexity. As a result, three parameters were evaluated

with the intention of using one or more as a means to classify good and bad crystals. They were the crystal sensitivity factor, the beam focusability factor, and the beam waist size at the measurement plane. Calculation of the crystal sensitivity factor, M^{-1}, was based on the developed resonator model and numerous approximations of the crystal behavior. Thus, after calculating the M^{-1} factor as a function of input power, no distinguishable pattern was seen. However, the beam focusability factor and the beam size, both showed distinct regions that separate good and bad crystals. Statistical analysis performed on the data supports a preliminary conclusion that these two parameters may be used as a quality control measure. These parameters are measured using existing internationally accepted procedures and are therefore the best currently available tools for determination of the quality of Nd:YAG crystals.

TABLE OF CONTENTS

LIST OF FIGURES

LIST OF TABLES

NOMENCLATURE

b	transverse derivative
c	speed of light in vacuum (2.9×10^8 m/s)
d	distance
dn/dT	dependence of the refractive index on temperature
f	focal length
f''	focal length of crystal caused by end face distortions
g_1, g_2	resonator parameters
h	Planck's constant, 6.62×10^{-34} Js
h_c	convective heat transfer coefficient
i	complex number operator
k	thermal conductivity
k_w	wave number
l	deviation from flatness of end faces
n	index of refraction
n_i	integral number of half wavelengths
n_s	variation in index of refraction due to stress
n_T	variation in index of refraction due to temperature change
n_0	index of refraction at center of crystal
n_2	downward curvature
q	complex beam parameter
r	radius of crystal
r_0	outer radius of crystal
w_0	beam radius
w_{T0}	beam waist radius
w_1, w_2	beam spot sizes
x,y,z	Cartesian coordinates

z_R	Rayleigh length
A	cross sectional area of crystal
A_0	amplitude at center of beam waist
$A(r,z)$	amplitude distribution along radial and axial directions
A, B, C, D	coefficients of the ABCD matrix
C_ϕ	tangential photoelastic constant of Nd:YAG crystal
C_r	radial photoelastic constant Nd:YAG crystal
E	energy level
K'	beam propagation factor
L	length
L_0	length parameter
L_1, L_2	distances from lens to reference plane
M	equivalent ABCD matrix
M^{-1}	crystal sensitivity factor
M^2	beam focusability factor
P_a	power absorbed by crystal
P_{in}	input power
Q	heat generated per unit volume
R	radius of curvature of beam wavefront
R_d	radius of deformation curvature
R_1, R_2	radii of mirrors
T	temperature
T_F	temperature of coolant
α	coefficient of thermal expansion
β	characteristic focal length of crystal
ϕ	angle from beam to reference axis
φ	longitudinal phase
λ	wavelength
λ_0	wavelength of light in a vacuum

ν	frequency
θ	divergence angle
θ_0	full divergence angle
Δl	change in length of crystal

1. INTRODUCTION

Current market demand for high power continuous wave Nd:YAG lasers is driving the development of innovative and efficient approaches to the manufacturing and testing processes for these lasers. Sales of lamp-pumped solid-state lasers reached $750 million during 2001. Even in the uncertain economy, demand for lasers is expected to grow. According to current estimates, the non-diode laser market will reach $2 billion in the year 2002 (Kincade and Anderson, 2002).

The essential component found in a Nd:YAG laser is the crystal responsible for the generation of the laser beam. However, the quality control procedures imposed on this component are not entirely representative of its importance in the overall laser system. Any deviations from the laser manufacturer specifications may lead to the possibility that the performance of the laser will be degraded to an unacceptable level. The single crystal growth process used to produce the crystals remains an extremely delicate and sensitive process (Hecht, 1994). Thus, any disturbances during the growth of the boule may only become apparent when the crystal is finally installed and operated in a laser cavity. Furthermore, the current quality control procedures imposed on the crystal by the manufacturer may not necessarily guarantee a crystal that will perform to the desired level. In order to produce a high-power Nd:YAG laser it is necessary to demonstrate control of the thermo-optical and thermomechanical properties of the crystal (Mudge et al., 2000). New quality control measures must be developed and implemented in order to ensure optimal manufacture and operation of the laser device.

A proposed method of ensuring the desired performance level is to test new crystals in a single cavity laser test stand. Doing so will allow for a number of important characteristics of the crystal to be measured actively while the laser is operational (Schlueter and Markille, 2002). One of the most important characteristics is the maximum laser power that can be extracted from the crystal. In addition to this, a method will be developed to test the optical characteristics of the crystal. One method to accomplish this will be the measurement of the thermal lens created within the crystal. This information can then be further analyzed and correlated with the input power to the laser device. From this, the crystal sensitivity factor can be extracted. This factor will relate the variation in the focal length to the corresponding change in input power. Using this information, it should be possible to determine an acceptable range of values that can be used as the quality control guidelines. This will result in an offline quality control mechanism that will be used for determining if a crystal meets certain criteria before it is installed in a laser device. As a result of this, the time required for final assembly and testing of the laser system will be significantly decreased. The examination of the laser crystal will become more deterministic and will greatly improve the production process for the laser device.

2. BRIEF HISTORY OF THE LASER

Albert Einstein first postulated the concept of using light energy in 1917. He developed the idea of stimulated emission of radiation from ground state atoms. Einstein explained that in the presence of a field of excited photons, other atoms are stimulated to emit additional photons to add to the original field. And remarkably, the emitted photons would go in the same direction and have the same frequency as the original stimulating field (Forward, 1979).

The foundation for modern day lasers was developed in 1954 by Charles Townes with the creation of a MASER. This acronym was defined as Microwave Amplification by Stimulated Emission of Radiation. This invention confirmed the notion of spontaneous emission and led to the creation of a laser. In 1958, Charles Townes and Arthur Schawlow devised the idea of the first visible laser while performing research at Bell Laboratories, however they did not actually construct one (Lucent, 1998). Ted Maiman invented the first ruby (visible light) laser shortly thereafter in 1960 at Hughes Research Laboratories. Maiman's laser used ruby as the excitation medium that was pumped by a helicoidal flashtube. The ruby crystal formed a plane parallel cavity, by having the ends polished and coated with silver. It was enclosed by an aluminum cylindrical cavity and cooled by air (Talbot, 2002). The first laser utilizing gas as the excitation medium, Helium and Neon, was developed by Ali Javan in 1961 at Bell Laboratories (Bellis, 2002). The first Nd:YAG laser was also developed at Bell Laboratories shortly thereafter in 1964 by J. E. Geusic, H. M. Markos, and L. G. Van Uiteit (Steen, 1998).

3. BASIC PRINCIPLES OF LASER OPERATION

Any atomic system (atoms, ions, etc.) can only exist in discrete energy states. A change in energy states (transition between two energy states or quanta) requires the absorption or emission of a photon. The wavelength of the absorbed or emitted radiation is given by Bohr's frequency relation

$$E_2 - E_1 = h\nu_{21} \quad , \tag{1}$$

where E_1 and E_2 are two discrete energy levels, ν_{21} is the frequency corresponding to the energy change, and h is the Planck's constant equal to 6.62×10^{-34} Js.

At thermal equilibrium, the lower energy states in the material are more heavily populated than the higher energy states. Under the correct conditions, a substance will absorb energy from an incident electromagnetic wave, thereby raising the atoms from a lower energy level to a higher one. This is the underlying principle behind the operation of a laser. An external energy pump source is required to transfer electrons from a lower energy level to a higher level, thus creating a population inversion of electrons in the laser medium. It should be noted that it is not possible to have a population inversion at thermal equilibrium (Koechner, 1999). A passing electromagnetic wave of appropriate frequency, incident on the excited laser material will be amplified because the incident photons cause the electrons present in the higher energy levels of the laser medium to drop to a lower level and thereby emit additional photons. This allows for the extraction of energy from the atomic system of the laser medium and the transfer of this energy to the incident radiation field. The release of the energy stored in the upper quanta by interaction with an electromagnetic wave is based on stimulated emission. Thus allowing

us to define the term LASER, that is an abbreviation for Light Amplification by Stimulated Emission of Radiation. The excitation of a material to allow for more atoms in a higher energy state than in lower levels will allow this material to amplify an incident radiation field at a frequency corresponding to the energy level difference. An interesting effect of this follows Einsteins predictions that the stimulated emission is identical to the stimulating radiation field. Meaning that the emitted field has the same directional properties, same polarization, phase, and spectral characteristics as the stimulating field. This accounts for the extremely high degree of coherence exhibited by emitted laser light. In solid-state lasers the energy levels and the associated transition frequencies result from the different quantum energy levels, or allowed quantum states of the electrons orbiting about the nuclei of atoms. In the case of the Nd:YAG laser, the Neodymium ions define the energy levels and thus the characteristics of the laser.

The Nd:YAG laser crystal has a defined absorption spectrum within which it absorbs energy incident on the crystal. In order to maximize energy transfer from the pump source the emission spectrum for the arc lamps must be a close match with the absorption spectrum of the crystal. The emission spectrum for a Krypton arc lamp is shown in Fig. 3.1. The absorption spectrum of Nd:YAG laser crystals is shown in Fig. 3.2.

From Fig. 3.2 is clear that Nd:YAG absorbs predominately in the emissive range of the arc lamps. The two important pumping bands in Nd:YAG crystals are in the regions of 730-760 nm and 790-820 nm.

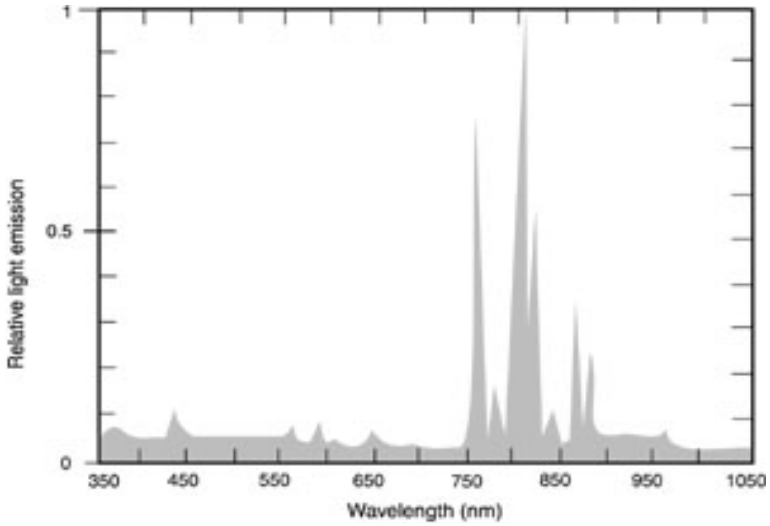

Fig. 3.1. Krypton emission spectrum.

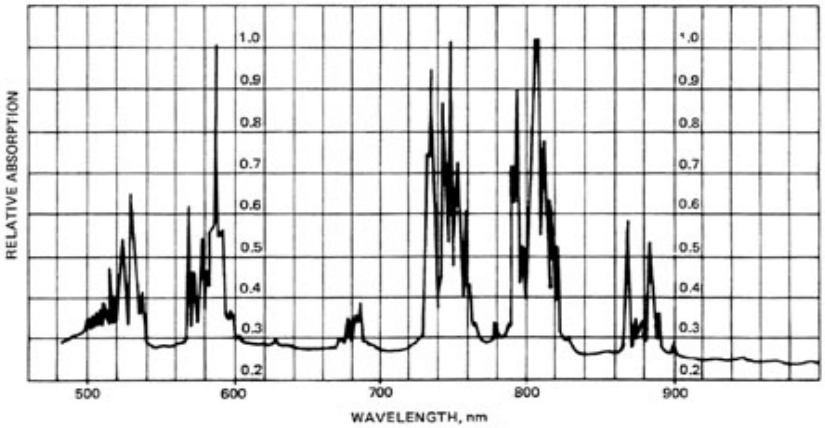

Fig. 3.2. Nd:YAG absorption spectrum.

Optical energy may also be absorbed at the shorter wavelength bands, but this is inefficient and the presence of too much light in the ultraviolet region will damage the rod by increasing its absorption, which leads to overheating of the crystal (CORD, 2002).

New developments in this field include the use of diode lasers as a pumping source that can be tuned to emit laser light at a particular wavelength. In the case of Nd:YAG lasers, a wavelength 808 nm will provide optimal energy coupling thus greatly increasing efficiency of the device. Efficiencies on the order of 10% are expected from these new technologies (Schlueter and Markille, 2002).

4. Nd:YAG LASERS

The Nd:YAG laser is the most common member of a family of lasers that are commonly grouped together as solid-state lasers. It was invented in 1964 and has remained in a continuous development and improvement process to the present day. The YAG laser follows the same operating principles as a ruby laser, however a different crystal substrate and active ions are used. The crystal substrate is Yttrium Aluminum Garnet ($Y_3Al_5O_{12}$) commonly known as YAG, with some of the Yttrium ions removed and replaced with Neodymium ions (Koechner, 1999).

The excitation process follows the same four level system structure prevalent in ruby lasers; an energy diagram of the transitions is shown in Fig. 4.1.

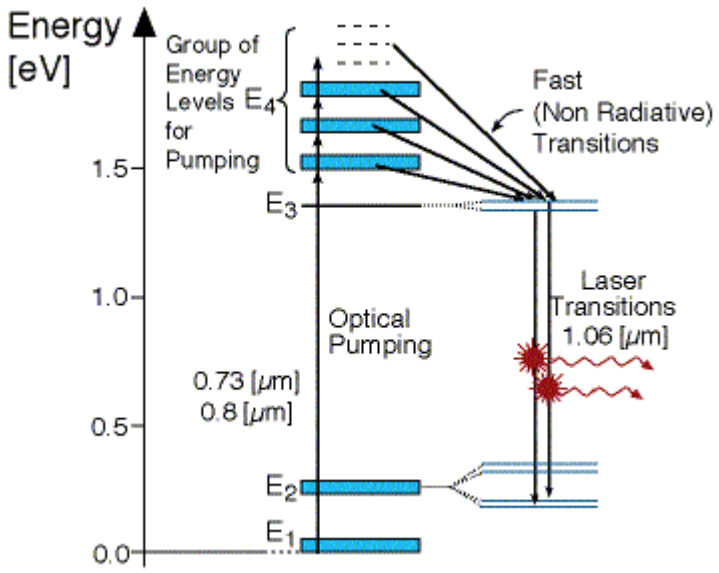

Fig. 4.1. Energy level diagram for Nd:YAG.

Ground state electrons at the E_1 level are excited to the E_4 energy state. At this point, the high-energy electrons undergo rapid, non-emissive decay to the E_3 level. Laser transition occurs during the drop from the E_3 to the E_2 level. This drop corresponds to a wavelength of 1.06 μm. The wavelength of the laser transition serves to characterize the different types of lasers, as each lasing material will emit laser light at a different wavelength. It is also possible, using frequency doubling, to have Nd:YAG lasers with a wavelength of 532 nm (HAAS, 1994)

The Nd:YAG laser is very inefficient in the conversion of input energy to useful laser light; typically Nd:YAG lasers are only approximately 2% efficient. The greatest losses are due to thermal effects and are associated with heat removal from the arc lamps and cavity (Bronski et al., 2002; Bronski and Machate, 2002). A breakdown of losses experienced by the laser system is shown Fig. 4.2.

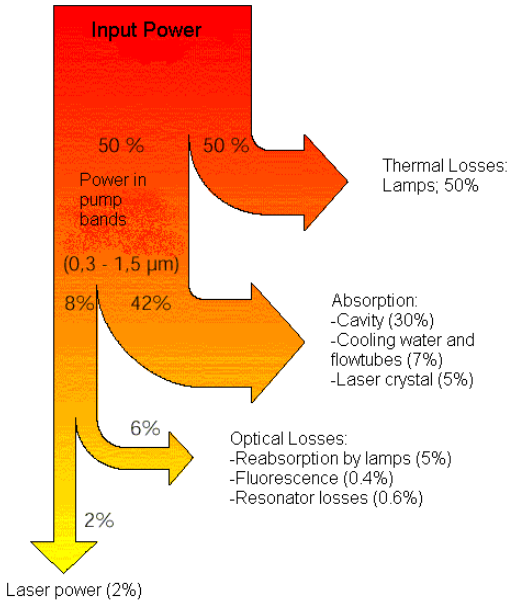

Fig. 4.2. Energy losses in a Nd:YAG laser.

In spite of their inefficiency, Nd:YAG lasers with over 30 years in operation have become the most versatile laser systems in use today. They have enjoyed widespread acceptance by the military serving as a range finders and target designators, by the medical community as surgical tools, and by the manufacturing sector where they serve a wide variety of roles, including welding, cutting, and drilling.

5. Nd:YAG COMPONENTS

A multitude of complex components come together in order to form an operational laser system. These components are each designed with a specific function and must operate at optimum levels in order to ensure an efficient laser. In the following sections, the major components of the laser will be discussed. Particular attention will be paid to resonator design theory and operational characteristics. However, other subsystems that are important to the overall operation of a laser, such as power supplies and cooling subsystems, will not be discussed within the scope of this thesis.

5.1. Resonator

The resonator, is perhaps the most important subassembly of any laser. Inside the resonator, energy supplied by an electromagnetic field is transferred to the laser medium that, in turn, causes spontaneous emission of additional energy, while the cooling system removes the excess heat generated by the excitation of the active element. The role of the resonator is to maintain an electromagnetic field configuration whose losses are replenished by the amplifying medium through stimulated emission (Koechner, 1999). Mirrors located in the resonator reflect photons along its optical axis, thus amplifying the beam and replenishing the energy that is extracted from the resonator, and other losses. Energy is extracted from the resonator using a partially transmissive mirror in order to fulfill the function for which the laser was designed. Additional losses are caused by optical elements within the resonator and by heat generation within the resonator

(Bronski et al., 2002; Bronski and Machate, 2002). The stimulated emission grows on each pass through the laser medium until it reaches an equilibrium level (Hecht, 1994). The gain of the system is held constant, as defined by the saturated gain coefficient. The saturated gain coefficient is always smaller then the small signal gain coefficient, prevalent during laser startup in the absence of stimulated emission (Koechner, 1999)

The regenerative laser oscillator is a combination of two components: the optical amplifier and the optical resonator. The resonator must be composed of several essential components shown in Fig. 5.1.

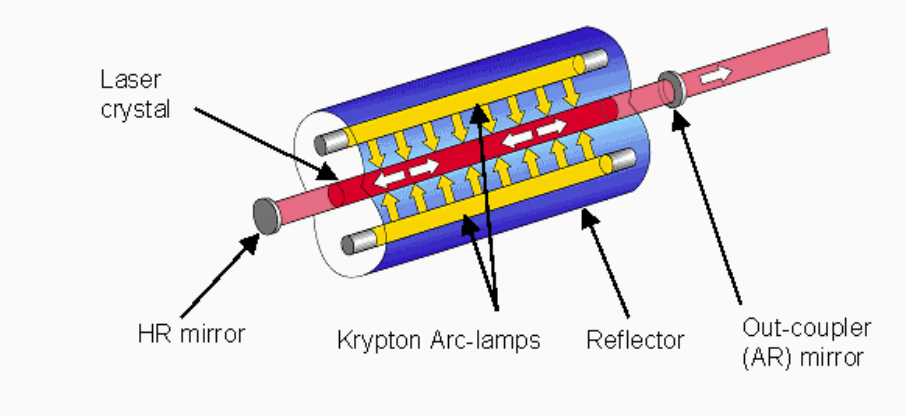

Fig. 5.1. Major components of a resonator.

The pump energy source is responsible for the population inversion in the laser medium, thus leading to energy storage in the upper energy levels. If the supplied energy field is sufficiently large to overcome the internal losses of the system, and having been triggered by some spontaneous radiation emitted along the axis of the laser, the system will start to oscillate between the two end mirrors. The resonator defines the spectral,

directional, and spatial characteristics of the laser radiation. Mirrors must be located on both sides of the resonator to allow oscillation to occur. One mirror should be nearly 100% reflective, and the other should be partially transmissive to allow a fraction of the laser energy to be extracted from the resonator. The degree of transmissivity is dependent on the application of the laser. These mirrors are commonly made from quartz glass and are supplied with a high-reflectivity (HR) coating for the approximately 100% reflective mirror and an anti-reflective (AR) coating on the partially transmissive mirror. In theory, the resonator could amplify itself to infinity if both mirrors used were 100% reflective. However, this is not possible due to internal losses within the cavity (Koechner, 1999).

Length dimensions of the resonators for Nd:YAG lasers are usually significantly larger than the laser wavelength to allow for laser oscillation. Resonators are usually open in order to drastically reduce the number of modes that can oscillate within the laser device. In open resonators, only the few modes corresponding to a superposition of waves traveling nearly parallel to the resonator axis have sufficiently low losses to allow for laser oscillation (Svelto, 1998). The most basic plane-plane (Fabry-Perot) resonator will be used as an example, Fig. 5.2.

In order to have constructive oscillations within the resonator, the length L must be equal to an integral number n_i of half-wavelengths

$$L = \frac{n_i \lambda}{2} \quad , \tag{2}$$

where λ is the wavelength.

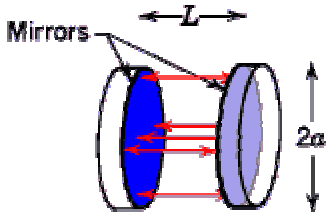

Fig. 5.2. Fabry-Perot resonator.

In addition, a necessary condition is that the electric field of the electromagnetic standing wave be zero on the two mirrors. Following this statement, the resonant frequencies ν, are then expressed in terms of *c* representing the speed of light

$$v = n\left(\frac{c}{2L}\right) \quad . \tag{3}$$

The initial simplicity of the plane-plane resonator is immediately offset by the practical difficulty of aligning the mirrors accurately enough to allow for "stable" operation of the laser. The term "stable" is defined by complex concepts. However, for simplicity at the time being, a more lenient definition will be used. A slightly more involved definition will be established later. In a simplified case, the threshold of stability is reached if a light ray initially parallel to the axis of the laser cavity can be reflected indefinitely back and forth between the two end mirrors. However, if it is now assumed that a light ray is slightly out of alignment with the optical axis of the resonator, a stable resonator should also be able to continually reflect this misaligned beam. In order to be able to accomplish this, the resonator must have some net focusing power. This, in the simplest case, is supplied by at least one of the mirrors, that possesses some degree of curvature. The plane-parallel resonator will meet the threshold condition for stability provided it is precisely aligned, but can not itself provide the required focusing

power needed to focus a misaligned light ray. In the case of a Nd:YAG laser, the crystal itself will provide the necessary focusing power due to the thermal lensing effect, thus allowing stable operation (Hecht, 1992). The crystal behaves like a thick lens with a refractive power that is dependent on the input energy (Dascalu et al., 1998).

Resonators that fail to meet the above stability criteria are referred to as unstable, due to the light rays diverging away from the optical axis of the resonator. Many different configurations of unstable resonators exist, one example having two differently sized mirrors, so that the light reflected from the larger mirror will escape around the outer edges of the smaller one. Both, stable and unstable, types have various advantages and disadvantages, along with different mode patterns. A stable resonator concentrates the light along the optical axis, making this oscillator particularly efficient in extracting energy from the center of the laser medium, but neglecting the outer area. The beam profile resembles a Gaussian distribution, with the peak energy density located at the center. This type of resonator is typically used with low-gain and continuous wave lasers, such as HeNe and Nd:YAG lasers.

An unstable resonator will concentrate the energy along the outer surfaces of the laser material and have zero energy along the optical axis. This type of resonator is typically more efficient because it utilizes more of the available area of the laser material. This configuration works best for high-gain pulsed lasers. Although the doughnut shaped beam has an intensity null in the near field, it smoothes out at greater distances from the laser, giving a more uniform energy distribution.

Of particular importance in the operation and utilization of a laser is the mode type of the resultant beam. Most lasers do not operate with only one mode, rather the output beam is an interference pattern of all modes within the resonator. The final beam shape may also be altered by means of beam shaping optics, however, significant losses can be expected. Resonators have two types of modes, transverse and longitudinal. Transverse modes are best seen in the cross-sectional profile of the beam. Longitudinal modes correspond to different resonances in the laser cavity occurring at different frequencies or wavelengths within the gain bandwidth of the laser. In most applications, only the transverse modes are of importance. Work done in the early stages of laser development classified transverse modes based on the number of nulls that appear across the beam cross section in the two axis directions. The fundamental mode, following a Gaussian distribution with the intensity peak at the center is known as TEM_{00}. The index is numbered depending on the number of nulls in a particular axis, common examples are shown in Fig. 5.3.

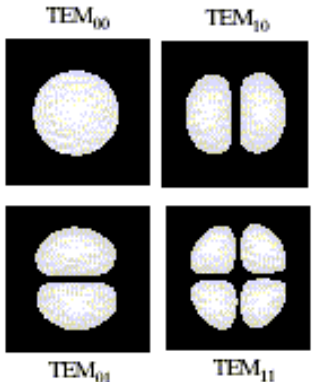

Fig. 5.3. Common TEM modes.

Currently only stable solid-state resonators are used in the material processing fields (Ifflaender, 2001). It was mentioned previously that different criteria defining a stable resonator exist and, at this point, a rigorous definition will be established using the complex beam parameter; the complex beam parameter is discussed in detail in Chapter 7.

A closer examination of the laser resonator shows that as the beam makes a round trip through the resonator, it encounters two reference planes (mirrors) at each pass. Using principles of Gaussian beam propagation, that will be further discussed in Chapter 7, we can define the criteria for a stable resonator. During a one way pass through the resonator, the beam will make the following path. Starting at the HR mirror, the beam will have a particular diameter that will vary as it travels the distance from the HR mirror to the crystal, passes through the crystal, and onto the AR mirror. Thus, the pass through the resonator consists of three ABCD matrices. The first matrix represents the pass through free space until the beam reaches the "input" surface of the crystal, the second matrix models the focusing power of the crystal between the "input" and "output" surfaces that is assumed to act as a simple thin lens, and the last matrix is used to model the free space propagation, i.e., from the "output" surface of the crystal to the second mirror. The complex beam parameter is determined at the first mirror using the radius of curvature and beam size. This parameter is frequently used in conjunction with the ABCD matrices to model optical systems, as will be further explained in Chapter 7. After defining a reference plane, the complex beam parameter can then be propagated through the resonator and back to its original reference plane. Taking into account the

return trip of the beam back to the original reference plane, we now have a total of six matrices representing a round-trip through the resonator. Multiplication of these six matrices will lead to the equivalent ABCD matrix "*M*" for the oscillator,

$$M = \begin{vmatrix} A & B \\ C & D \end{vmatrix} \quad . \tag{4}$$

Using Eq. 4, the complex beam parameter product, q, at different locations within the resonator is determined to be (Siegman, 1986)

$$q = \frac{Aq + B}{Cq + D} \quad , \tag{5}$$

where

$\begin{vmatrix} A & B \\ C & D \end{vmatrix}$ is the matrix corresponding to a full round trip through the resonator.

The resonator is considered stable when the following stability criterion is fulfilled:

$$\left(\frac{A + B}{2} \right)^2 < 1 \quad . \tag{6}$$

A stable resonator will have a confined and finite TEM_{00} mode radius, that will also remain true for unlimited mirrors and unlimited medium size (Ifflaender, 2001). A value for the complex beam parameter determined at one plane must be reproduced after a round-trip in order for the resonator to be considered stable. The procedure outlined above is demonstrated for the HL506D laser in Appendix A. The corresponding numerical solutions for the complex beam parameter can be determined using (Ifflaender, 2001)

$$\frac{1}{q} = \frac{D - A}{2B} \pm \frac{i}{2B} \sqrt{4 - (A + D)^2} \quad , \tag{7}$$

where *i* is the complex number operator. In order for the beam radius to remain in the real domain, the expression under the square root sign must be positive (Ifflaender, 2001).

5.1.1. Plane-parallel resonators

The laser system test stand that was used in this thesis utilized a plane parallel resonator with flat mirrors. In this case, the radius of curvature of the front and rear mirrors is equal to infinity. The active medium of the laser when placed inside the resonator cavity will alter the length of the optical path through the cavity, and also change the mode configuration.

The change in the optical path occurs due to the thermal lensing of the crystal and the stress birefringence effect. The majority of the perturbation is a result of the thermal lensing of the laser crystal. This effect can be modeled by a simple thin lens with an effective focal length of f. It should be noted, that the thin lens model is only a first order approximation of the system. The YAG crystal exhibits much more complex behavior that will be explained later, however, for simplicity a thin lens will be used to establish a working model of the resonator. Now, using the thin lens model, the focal length of the crystal can be determined. With the focal length, it is possible to determine resonator stability using two resonator parameters. These parameters are functions of the resonator length and the optical components within the resonator, they are defined as

$$g_1 = 1 - \frac{L_2}{f} - \frac{L_0}{R_1} \quad , \tag{8}$$

$$g_2 = 1 - \frac{L_1}{f} - \frac{L_0}{R_2} \quad , \tag{9}$$

where $R_1$and R_2 are the radii of each mirror, L_0 is defined as

$$L_0 = L_1 + L_2 - \left(\frac{L_1 L_2}{f} \right) \quad , \tag{10}$$

f is the focal length of the thermal lens, and L_1 and L_2 are the distances from each mirror to the thermal lens. Because the YAG crystal was modeled as a single thin lens located equidistant from each mirror, the focal length of the lens can be used to determine the resonator parameters that are frequently used to define resonator stability on the g_1g_2 stability diagram shown in Fig. 5.4.

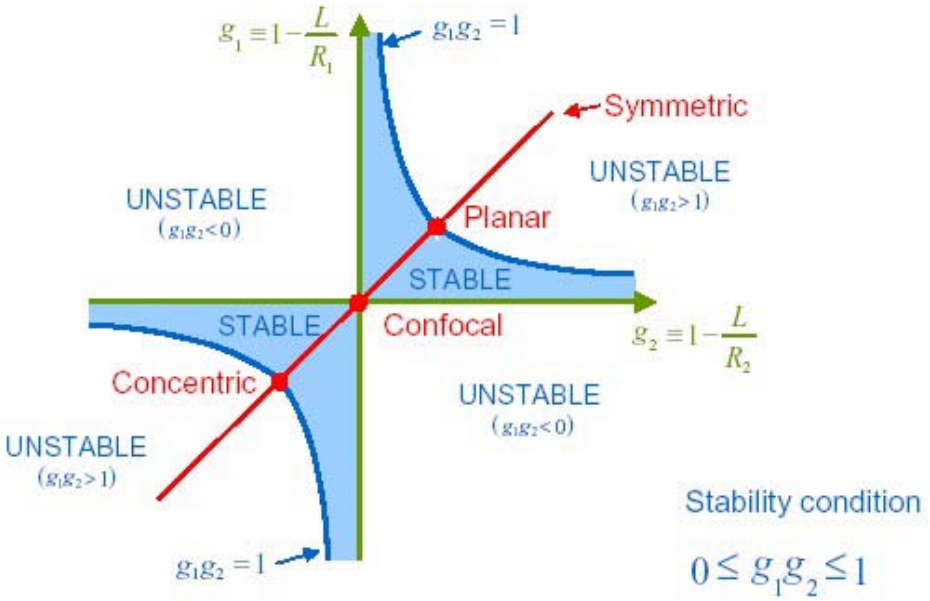

Fig. 5.4. The g_1g_2 stability diagram (Kaivola, 2002).

If both mirrors are identical and have infinite radii of curvature, we can say that the ratio between the resonator parameters and the spot size remains constant (Koechner, 1999), i.e.,

$$\frac{w_1^2}{w_2^2} = \frac{g_2}{g_1} \quad , \tag{11}$$

where w_1 and w_2 are the waist spot sizes, and g_1 and g_2 are the corresponding resonator parameters, respectively. Also, identical mirrors require that the resonator operates only along the symmetric axis shown in Fig. 5.4. Simplifying Eq. 11 it is seen that the waist diameters at both mirrors will be identical and hence the resonator parameters must be equal. It is important to note that the waist diameter of the TEM_{00} mode at one mirror in any resonator can be determined by utilizing the resonator parameters. Knowing this, the resonator parameters can be defined in terms of the focal length, f, and the beam waist radius can be defined in terms of the resonator parameters as

$$g = g_1 = g_2 = 1 - \frac{L}{2f} \quad , \tag{12}$$

$$w_1^2 = w_2^2 = \left(\frac{\lambda L}{\pi}\right)\left(1 - g^2\right)^{-\frac{1}{2}} \quad , \tag{13}$$

respectively, where L is the length of the resonator, λ is the wavelength of the laser beam, and f is the focal length of the thermal lens.

5.2. Nd:YAG crystals

The YAG crystal has become widely used in many commercial and military applications, and is by far the most important solid-state laser medium available (VLOC, 2002). YAG crystals are currently the only widely used solid-state material that is capable of continuous wave operation (CORD, 2002). As mentioned previously, it is a single crystal of $Y_3Al_5O_{12}$ where some of the Yttrium ions have been removed and substituted by trivalent Neodymium ions. Neodymium ions were chosen due to the similarity in size, being only slightly larger then the Yttrium ions, so as not to upset the cubic crystal lattice of the crystal, and also because of optimum pumping characteristics. Nd:YAG is grown as a single crystal, almost always in the <111> direction using the Czochralski method. This process produces the great majority of all available single crystals available today. Utilizing this process, crystals are grown as boules, or ingots, shown in Fig. 5.5 from which individual rods are core drilled (VLOC, 2002).

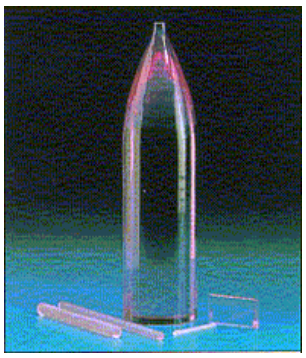

Fig. 5.5. Nd:YAG boule (VLOC, 2002).

Typical boule sizes are on the order of 100 mm diameter, with length dependent on the desired application for the crystal. Due to the high melting point of Nd:YAG, crystal growth is conducted in a high temperature crucible fabricated from iridium (VLOC, 2002). All Nd:YAG crystals grown by this method exhibit a bright core running along the length of the crystal, giving each crystal a pinkish tint. The drawback with this procedure is the slow growth rate, typically on the order of 0.5 mm/hour, growing a crystal typically requires at least thirty-five days (VLOC, 2002). Hence, crystals produced using this method are rather expensive. Although this method has been used for over 40 years, no superior alternative to growing Nd:YAG crystals has been developed, as of this time. Continuous developments and improvements over its lifespan, have allowed the crystal to currently be capable of generating over seven hundred Watts from a single cavity. More importantly, in the quest for higher laser power, cavities have been coupled together in order to obtain even more power. Currently the most powerful commercially available lamp pumped Nd:YAG lasers are capable of producing over 6 kW of power (Kumkar, 2002).

5.3. Optical and physical properties

The Nd:YAG crystal exhibits extremely attractive qualities that enable it to be used as a laser medium. In order to be a suitable host, the crystal substrate should be transparent to the pump light, absorb very little at the laser wavelength, and have good mechanical properties as a heat conductor.

Due to the great thermal stresses that the crystal is subjected to as a result of lamp pumping, it is important that the material has a good thermal conductivity and a low coefficient of thermal expansion. These characteristics are important in order to ensure that heat is removed efficiently and that the crystal does not significantly alter its size during operation. The melting point of the crystal must also be high enough so that the applied energy field and corresponding heat generation will not raise the crystal to the melting level.

The optical characteristics of the crystal make it an ideal choice for a laser material. The crystal itself is optically isotropic crystal possessing a cubic structure that is characteristic of garnets. This laser material has a great advantage in that each cavity can be operated as either (1) an oscillator in a stable or unstable configuration, or (2) as a simple amplifier cavity. Common optical characteristics of the Nd:YAG crystal are shown in Table 5.1.

Table 5.1. Optical properties of Nd:YAG crystal.

Property	**Value**
Index of refraction	1.82
Extinction ratio	30 dB
dn/dT	$7.3 \cdot 10^{-6}$ K^{-1}
Stimulated emission cross section	$2.8 \cdot 10^{-19}$ cm^2

The physical properties of the crystal are also very attractive, the structure is stable from the lowest temperatures up to the melting point, and no solid-solid phase

transformations of the Nd:YAG crystal have been reported (Koechner, 1999). Common physical properties of the Nd:YAG crystal are shown in Table 5.2.

Table 5.2. Physical properties of Nd:YAG crystal.

Property	`
Young's modulus	310 GPa
Poison's ratio	0.27 (estimated)
Specific heat	0.14 cal/(g °C)
Coefficient of thermal expansion	$7.8 \cdot 10^{-6}$/°C
Density	4.56 g/cm^3
Melting point	1970 °C

The strength and hardness of YAG are slightly lower than those of ruby, however, the crystal can still be produced using normal fabrication techniques and does not pose any serious breakage problems with normal handling. Attempts to drastically increase the doping levels of the Neodymium ions in order to achieve higher gain have resulted in the creation of distortions within the crystal lattice structure due to the Neodymium ions being slightly larger than their Yttrium counterparts, as well as shortening of the fluorescent lifetime. The current doping level limit is approximately 2% Neodymium by atomic weight (Koechner, 1999).

Manufacturing specifications for YAG crystals are extremely important, but are highly dependent on the application of the laser. Typically controlled features and the corresponding tolerances for the Nd:YAG crystals are listed in Table 5.3. Flat and parallel end faces are perhaps the most important features to ensure perpendicularity to the optical axis of the crystal and the laser device; deviations from the specifications may

have drastic effects by shifting the path of the beam. Parallelism of the faces, along with constant crystal diameter and barrel roughness are also crucial parameters in order to retain as many symmetric features as possible.

Table 5.3. Tolerances on a Nd:YAG crystal.

Tolerance type	Numerical tolerance
Flatness of ends	λ/10
Parallelism of end faces	± 4 arc sec
Perpendicularity of end faces	± 5 minutes
Physical dimensions (length)	± 0.5 mm
Physical dimensions (diameter)	± 0.025 mm

Barrel roughness, defined as the roughness of the outer surface of the crystal has been found to be influential in determining the maximum power output of the crystal, and is also critical in determining the stress fracture limit (Schlueter and Markille, 2002). Manufacturers of crystals usually perform an extinction ratio test, by measuring the power level of light of different polarizations that passes through the crystal. The experimental procedure consists of passing a HeNe laser beam through two polarizer blocks, which are located before the crystal and are initially aligned to each other. After passing through both polarizers, the beam enters the Nd:YAG crystal, and after emerging from the crystal the power level is measured. Two measurements of the power are conducted, first with both polarizer blocks aligned to each other and the second with one of the polarizers rotated. The difference in power transmitted through the crystal is proportional to the magnitude of birefringence (VLOC, 2002). Further evaluation of the

stressed areas in the crystal is possible using a Twyman-Green interferometer, that uses a HeNe laser to show an interference pattern of the crystal (VLOC, 2002).

6. METHODS AVAILABLE FOR LASER BEAM MEASUREMENTS

During the initial alignment and over the course of the laser life span, it becomes necessary to quantitatively measure certain beam parameters. Measurable parameters may include: beam position, power level, intensity profile, divergence, focal point, and the M^2 factor.

The power output of the laser is perhaps the easiest to measure. This measurement can be performed using a device similar to a calorimeter that will measure the change in temperature of a material that is placed in the path of a laser beam, and correlate that to the corresponding energy heating it. This measurement typically takes only several minutes, over the entire power range of the laser device, and requires no extensive modifications to the laser. It is important that during the measurement the laser beam is operated with the focusing lens removed. Failure to do so will result in the laser beam melting through the power meter. An example of a power curve obtained using a Coherent power meter is shown in Appendix B.

During the alignment stages, “tape” shots done with crosshairs are frequently utilized. An example of a fixture used for “tape” shots is shown in Fig. 6.1.

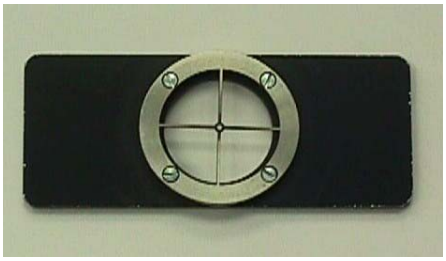

Fig. 6.1. Fixture used for tape shots.

To facilitate the alignment process, photographic paper is used that reacts with the laser at the particular wavelength. The crosshairs are used to ensure that all quadrants of the burnt photographic paper are symmetric, Fig. 6.2.

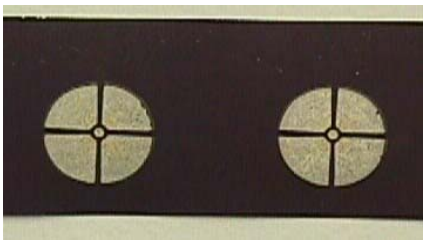

Fig. 6.2. Beam profiles on phtographic paper.

The general procedure is to shoot the laser beam at the photographic paper that is located behind the crosshairs, but not to burn through it, hence only low power levels, or very short pulse times are required. Using two crosshairs coaxially aligned and taking two separate tape shots, it is possible to determine if the laser beam is perpendicular to the specified plane. This procedure is vital when aligning optical components, such as the incouplers that serve to focus the beam into a fiber optic cable. However, this method does not provide a three-dimensional picture of the beam and hence can hide many possible imperfections of the beam. By measuring the resultant profile shown on the burnt photographic paper, the spot size of the laser beam can be determined.

The intensity profile of the laser beam is also simple to measure using a CCD camera and the corresponding software package (Spiricon, 2002). However, before the beam can be measured it must be drastically attenuated so as not to burn through the sensing element. The camera determines the shape of the beam in two-dimensions based

on the activated pixels of the camera, and the intensity sensed by each pixel. The result of this is a black and white or, depending on the software package used, a color rendition of the beam shape, with brightness of the pixels signifying the power level in a black and white system. Sophisticated computer algorithms and hi-end cameras can turn this information into a three-dimensional picture that displays the beam shape. A problem occurring when using cameras stems from the calibration procedure. This is caused by the baseline setting of the camera not being adjusted properly, thus causing problems with the background noise. When the beam waist is located at the CCD camera, it is possible that it only covers a very small number of pixels. Thus any background noise present over a large number of non-illuminated pixels would cause a significant error in the measurement (Roundy, 1994). Numerous firms, such as PRIMES (2002) and Spiricon (2002) have developed complex methodologies to specifically address this problem and present results representative of the actual laser beam

A simple methodology to measure the divergence of the beam is to first determine the beam diameter as it exits the laser. Then, allow the beam to propagate a precisely known distance to another location where the diameter of the spot size can be accurately measured. The divergence is simply calculated as the amount the beam diameter expands per unit length.

The focal point and the M^2 factor are difficult to measure manually and require special equipment. Usually the focal point is determined theoretically and is verified by beam analyzer devices that follow ISO standards. In general terms, the M^2 value is an indicator of how close the beam is to the perfect theoretical Gaussian shape, it will be

more specifically defined in Section 6.1. In order to maximize efficiency at the workpiece the beam must have a uniform shape. An example of a current product available to measure the M^2 factor uses a CCD camera and two deflection mirrors mounted on a highly accurate movable platform. By movement of the platform and the two deflection mirrors, it is possible to lengthen the beam path and measure the "caustic" of the beam. The caustic of the beam allows the experimenter to obtain a complete picture of the beam within several Rayleigh ranges of the focal point. The Rayleigh range of a beam is defined as the depth of focus for a focused Gaussian beam and is defined in Eq. 34. The caustic is typically defined once the location of the beam waist is known. Typically, the caustic is measured over a span greater than four Rayleigh ranges of the beam (DIN, 1999). Measurement of the caustic coincides with measurement of the beam focusability factor. The measurement apparatus manufactured by Spiricon Inc. is shown in Fig. 6.3. A detailed description of how beam analyzers function, with particular attention paid to the PRIMES FocusMonitor will be presented in Section 8.2.1.

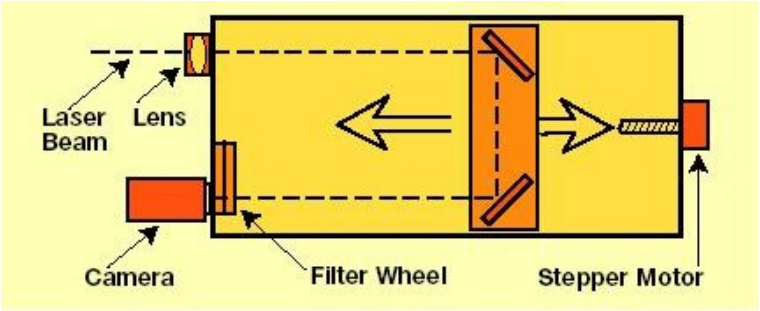

Fig. 6.3. YAG:MAX beam analyzer (Spiricon, 2002).

Accurate and precise measurement of the beam is critical to the efficient and acceptable operation of the laser. Current developments include integration of the measurement system as an in-line device that samples a small fraction of the beam and is able to record beam parameters during actual working conditions of the laser.

6.1. Beam focusability factor

The beam focusability factor has been used for a number of years as a method of evaluating laser performance. This quantifiable factor also known as M^2, is a measure of how close a laser beam is to a perfect Gaussian beam. A perfect laser beam will have an M^2 equal to one, whereas an imperfect beam will have a value greater than one. Recently, the International Standards Organization defined standards and specifications for the measurement and use of the M^2 factor that will serve as a guideline for quality measurement of all laser beams (Spiricon, 2002).

All radially symmetric laser beams can be characterized by the following three parameters, the position of the beam waist, the diameter of the beam waist, and the far-field divergence angle of the beam. The last parameter is defined as one-half of the full divergence angle given by Eq. 39 (Koechner, 1999). Using these parameters, it is possible to calculate the beam diameter at any other point along the propagation axis of the beam. With this information, the beam focusability factor can also be determined. Determination of this factor is frequently accomplished using beam analyzer systems that record the size of the laser beam. Usually it is desirable to obtain this information from the caustic of the beam and throughout multiple Rayleigh ranges. The Rayleigh range is

defined as the distance the beam must travel in order for its diameter to enlarge by a factor of √2. Conducting measurements over several Rayleigh ranges allows the beam analyzer to automatically determine the location of the beam waist that is defined as the point in the propagation path where the beam diameter has the smallest value.

The standards that have been developed for the measurement of the beam focusability factor are listed under EN ISO (International Standards Organization) 11146 for the United States or in DIN (Deutsche Industrie Norm) 11146 for European industry (DIN, 1999). The procedures for proper measurement of both radially symmetric and non-symmetric beams are described in great detail within the documents of DIN (1999). For the purposes of the experiments that will be conducted as part of this thesis, it can be assumed that the YAG laser produces a radially symmetric beam. This simplifies the calculations required for the determination of M^2. However, all of these calculations are now performed by computer algorithms developed by the beam analyzer manufactures, following the ISO regulations. The ISO standards explicitly define how the beam analyzer should be aligned to the laser beam and how it should be used with a laser device.

In order to measure the necessary beam parameters required for the calculation of the beam focusability factor, the analyzer must be positioned perpendicular to the propagation axis of the beam in order to ensure accurate intensity distribution. The measurement must be performed near the beam waist, regardless of whether the waist is created by an additional lens in the system, or if it is the natural focus point. The measurements must be repeated at a number of locations in the vicinity of the focal point,

in order to correctly locate the focal point. The requirements according to ISO standards is that at least 10 measuring planes should be used, with the measurement repeated at least 5 times at each plane. Half of the measurements shall be distributed within one Rayleigh length on either side of the beam waist, and approximately half of them should be distributed beyond two Rayleigh lengths from the beam waist (DIN, 1999). Doing so will ensure that the beam analyzer will be able to determine the location of the beam waist and obtain an accurate representation of the beam.

6.2. Nd:YAG crystal sensitivity factor

The crystal sensitivity factor, otherwise known as M^{-1}, presents a very important relationship between the pump power into the laser and the corresponding variation in the focal length of the crystal. The analytical determination of this factor will be presented below. Using the equations defined, the thermal lensing, along with the crystal sensitivity factor, is modeled analytically in Appendix C.

The thermal lens of the crystal is a result of the high thermal stresses generated within the crystal during pumping. The thermal lensing effect is thus highly dependent on the pumping power and the efficiency of the cooling system. The effects of the thermal lens are extremely important and cannot be neglected in the design and production of laser systems. Also, it should be noted that in the case of pulsed laser systems, thermal equilibrium cannot be reached at a repetition rate lower than 5 Hz (Dascalu et al., 1998). This can be ignored in this case because a continuous wave laser

is used. The net result of thermal stresses is a degradation in the laser beam quality due to the thermal lensing and possible fracture of the laser crystal if the thermally induced stress exceeds the tensile strength of the material (Clarkson and Hanna, 1998).

In order to determine the theoretical focal length of the crystal, we must first define the effect of variation of the index of refraction that is both stress and temperature dependent. This effect is shown by

$$n(r) = n_0 + \Delta n(r)_T + \Delta n(r)_s \quad , \tag{14}$$

where $n(r)$ is the radial variation in the index of refraction, n_0 is the index of refraction at the center of the crystal, $n(r)_T$ is the temperature dependent change in the refractive index, and $n(r)_s$ is the stress dependent change. Now, it will be useful to define the heat generated per unit volume, Q, in the laser crystal as

$$Q = \frac{P_a}{\pi r_0^{\,2} L} \quad , \tag{15}$$

where L is the length of the crystal, r_0 is the outer radius of the crystal, and P_a is the power absorbed by the crystal when a steady state condition is reached. This means that the heat absorbed is equal to the heat removed by the coolant from the crystal surface and is defined by

$$P_a = 2\pi r_0 L h_c \left[T(r_0) - T_F\right] \quad , \tag{16}$$

where h_c is the convective heat transfer coefficient, T_F is the coolant temperature, and $T(r_0)$ is the temperature at the outer surface of the crystal.

Now using the relationship defined in Eq. 14, the temperature dependent variation in the index of refraction is determined by the variation of temperature between the outer

wall and the center of the laser crystal. Along with the utilization of a material property relating the change in the index of refraction per unit temperature, the variation due to the thermal effects is defined by (Koechner, 1999)

$$\Delta n(r)_T = [T(r) - T(0)]\left(\frac{dn}{dT}\right) \quad , \tag{17}$$

where *T(0)* is the temperature at the center of the crystal, *T(r)* is the temperature at distance *r* away from the center of the crystal, and *dn/dT* is the dependence of the index of refraction on temperature. Now, Eq. 17 can be rewritten in alternate form based on the heat generation defined in Eq. 15 resulting in (Koechner, 1999)

$$\Delta n(r)_T = -\frac{Q}{4k}\left(\frac{dn}{dT}\right) r^2 \quad , \tag{18}$$

where *k* is the thermal conductivity. The temperature profile as a function of radius, *T(r)*, is then determined to be

$$T(r) = T(r_0) + \left(\frac{Q}{4k}\right)\left(r_0^{\,2} - r^2\right) \quad , \tag{19}$$

where $T(r_0)$ is the temperature at outer surface, *k* is the thermal conductivity, and r_0 is the outer radius of the crystal.

The index of refraction is frequently modeled using simple principles in order to approximately define the behavior of the index of refraction in the crystal as it is pumped with optical energy. However, in order to more accurately represent the actual optical behavior of a crystal, much more detailed expressions governing the behavior of the index of refraction must be developed. It has been shown that the index of refraction undergoes a quadratic variation with the radius, thus an optical beam will experience a

quadratic spatial phase variation as it propagates along the crystal axis (Ifflaender, 2001). This is similar to the effect caused by a spherical lens and hence the index of refraction can be modeled by (Koechner, 1999)

$$n(r) = n_0\left(1 - \frac{2r^2}{b^2}\right) \quad , \tag{20}$$

where *b* is defined as the transverse derivative. However, before the transverse derivative term can be defined, the concept of a quadratic duct must be explained. If one assumes a light beam of finite radius propagating through a crystal, the portion of the beam closest to the outer edge of the crystal encounters a region with a lower index of refraction than the portion at the center of the crystal. This results in the outer portion of the beam traveling faster due to a lower value of the index of refraction, whereas the inner portion of the beam is traveling through a region with a higher index and thus must travel slower. The result of this is that the beam is continually being bent towards the central axis of the crystal, this concept defines a stable quadratic duct. Now using the above concepts, it can be shown that the index of refraction will vary both radially and axially. Defining this variation in the index of refraction we have (Siegman, 1986)

$$n(r,z) = n_0(z) - \frac{1}{2}n_2(z)r^2 \quad , \tag{21}$$

where $n_0(z)$ is the variation along the axis of the crystal, and $n_2(z)$ is defined by

$$n_2(z) \equiv -\left.\frac{\partial^2 n(r,z)}{\partial r^2}\right|_{r=0} \quad . \tag{22}$$

The parameter defined in Eq. 22 represents downward curvature of the index at the central axis. Using this parameter and the index of refraction along the axis of the crystal, we can define the *b* term in Eq. 20 as (Siegman, 1986)

$$b^2 = \frac{n_2}{n_0} \quad . \tag{23}$$

Illustrating this concept of a duct with a radially varying index of refraction we have Fig. 6.1.

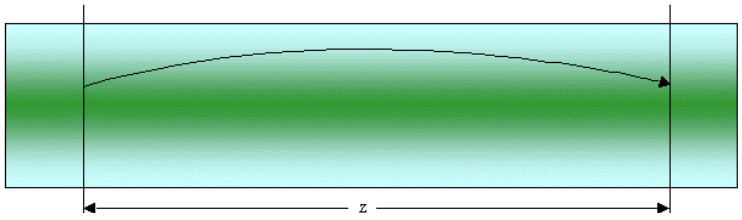

Fig. 6.1. Ray propagation in a duct.

The focal length of a quadratic duct, like that found in a Nd:YAG crystal, is approximated by (Koechner, 1999)

$$f \cong \frac{b^2}{4n_0 L} \quad , \tag{24}$$

where it is assumed that the focal length *f* is very long as compared to the length of the crystal, *L*. The total variation of the refractive index due to thermal and stress effects is represented by (Koechner, 1999)

$$n(r) = n_0 \left[1 - \frac{Q}{2k} \left(\frac{1}{2n_0} \frac{dn}{dT} + n_0^2 \alpha C_{r,\phi} \right) r^2 \right] \quad , \tag{25}$$

where n_0 is the index of refraction at the center of the crystal, α is the coefficient of thermal expansion, and $C_{r,\phi}$ are the polarization dependent elastooptical coefficients of Nd:YAG. The change of the refractive index due to the thermal strain is dependent on the polarization of the incident light. Thus, two elastooptical coefficients are required as shown in Eq. 25, one coefficient for the tangential component of the light and one for the radial component.

The focal length of a lens with a varying index of refraction, according to Eq. 25, is then given by (Koechner, 1999)

$$f = \frac{k}{QL}\left(\frac{1}{2}\frac{dn}{dT} + \alpha C_{r,\phi} n_0^3\right)^{-1} \quad . \tag{26}$$

However, the deformation of the end faces of the crystal also contributes to the overall variation in the focal length of the crystal. Experimental data have shown that for cylindrical crystals, stresses causing distortions of the end face flatness were found to occur within a region of approximately one radius of the crystal, as measured from the end face. The deviation from flatness of the end faces, *l(r)*, is obtained from the thermal expansion of the material as shown by

$$l(r) = \alpha r_0 \left[T(r) - T(0)\right] \quad , \tag{27}$$

where α is the coefficient of thermal expansion, r_0 is the region of the crystal over which expansion occurs, and *T(0)* is the temperature at the center of the crystal. The resultant curvature radius of the deformation is then determined by (Ifflaender, 2001)

$$R_d = -\left(\frac{d^2 l}{d^2 r}\right)^{-1} \quad , \tag{28}$$

and can be approximated using

$$R_d \cong \frac{r_0^2}{\Delta l} \quad , \tag{29}$$

where r_0 is the outer radius of the crystal, and Δl is the change in the length of the crystal (Ifflaender, 2001). The resulting focal length of a crystal caused by the end face distortions, f'', can be obtained using the thick lens formula for geometric optics, to be (Koechner, 1999)

$$f'' = k\left[\alpha Q r_0 (n_0 - 1)\right]^{-1} \quad , \tag{30}$$

where k is the thermal conductivity, α is the coefficient of thermal expansion, Q is defined in Eq.15, r_0 is the outer radius of crystal, and n_0 is the index of refraction at the center of the crystal. And finally, the overall focal length of the crystal, summing together the temperature and stress dependent variations along with the distortion of the end faces, can be shown to be (Koechner, 1999)

$$f = \frac{kA}{P_a}\left(\frac{1}{2}\frac{dn}{dT} + \alpha C_{r,\phi} n_o^3 + \frac{\alpha r_0 (n_0 - 1)}{L}\right)^{-1} \quad , \tag{31}$$

with A being the cross sectional area of the crystal, and P_a being the heat absorption.

Now, knowing the focal length of the laser crystal it is possible to relate this information to the input power provided to the system. Relation of these two parameters results in the crystal sensitivity factor, M^1, that is defined by

$$M^{-1} = \frac{d\left(\frac{1}{f}\right)}{dP_{in}} \quad , \tag{32}$$

where f is the focal length of the crystal and P_{in} is the input power to the laser.

This factor will allow one to see how the optical power varies in response to a change in the input power to the system. This factor is very important during the design phases of the laser in order to ensure that the resonator will remain functional throughout the entire operating power range. The laser system must be able to handle a multitude of variations that affect the crystal sensitivity factor, including the aging of the lamps, power supply, and cooling system fluctuations.

7. GAUSSIAN BEAM OPTICS

In order to set the groundwork for calculations that will be used during this thesis, the basics of Gaussian beam propagation will be briefly presented. Although the beam created by a Nd:YAG laser is complex and contains multiple modes, a simplified analysis can be performed by assuming that the beam is a simple Gaussian beam with the fundamental TEM_{00} mode. This results in a radially symmetrical beam with an amplitude distribution, *A(r,z)*, in the radial, *r*, and axial, *z* directions, that can be represented by (Ifflaender, 2001)

$$A(r,z) = A_0 \frac{w_{T0}}{w_0} \exp\left[-r^2 \left(\frac{1}{w_0^2} + \frac{ik}{2R} \right) + i\left(k_w z - \varphi\right) \right] \quad , \tag{33}$$

where A_0 is the amplitude at the center of the beam at the waist, w_{T0} is the beam waist radius, w_0 is the beam radius at a given point along the propagation length, and R is represented by $R(z)$ defined as the curvature of the wavefront. The Rayleigh length, z_R, is defined as

$$z_R = \frac{\pi {w_{T0}}^2}{\lambda} \quad . \tag{34}$$

The wave number, k_w can be determined from

$$k_w = \frac{2\pi}{\lambda} \quad . \tag{35}$$

And the longitudinal phase, φ, is defined as

$$\varphi = \arctan\left(\frac{z}{z_R} \right) \quad . \tag{36}$$

The beam spot size as a function of position, as it propagates along the optical axis, can be determined using

$$w_0^2(z) = w_{T0}^2\left[1+\left(\frac{z}{z_R}\right)^2\right] \quad , \tag{37}$$

where w_{T0} is the waist radius, z is the distance from a reference plane, and z_R is the Rayleigh length. Defining the origin of the coordinate system at the waist of the beam, the radius of curvature of the wavefront can be determined as (Ifflaender, 2001)

$$R(z) = z_R\left(\frac{z_R}{z}+\frac{z}{z_R}\right) \quad . \tag{38}$$

The two parameters, w_{T0} and z_R, used in Eqs 37 and 38 are then the determining factors of a Gaussian beam, from which all other desirable parameters can be determined. The divergence of the beam depicts how much the beam diameter enlarges as it travels a specified distance. The waist of a laser beam has some notable characteristics. At the beam waist, the radius of curvature must be infinite ($R = \infty$), and the beam will have the smallest spot size throughout the propagation path. Thus, the full divergence angle, θ_0, of the fundamental mode beam will be determined by (Koechner, 1999)

$$\theta_0 = \lim_{z\to\infty}\frac{2w_0(z)}{z} = \frac{2\lambda}{\pi w_{T0}} = 1.27\frac{\lambda}{(2w_{T0})} \quad , \tag{39}$$

where λ is the wavelength of the laser beam, and w_{T0} is the spot size at the waist. Now, using the definition for determining the beam size along the propagation path as shown in Eq. 37, and the radius of curvature, Eq. 38, it is possible to develop a complex beam parameter that is extremely useful when propagating Gaussian beams through optical

systems. This parameter, $q = q(z)$, can be calculated at any point along the propagation path and is defined as (Ifflaender, 2001)

$$\frac{1}{q} = \frac{1}{R} - \frac{i\lambda}{\pi w_0^2} \quad , \tag{40}$$

and,

$$q = \frac{R\pi w_0^2}{\pi w_0^2 - i\lambda R} \quad , \tag{41}$$

where R is the radius of curvature of the wavefront, w_0 is the radius of the beam, and λ is the laser beam wavelength. Equation 40 allows us to define the beam radius, w_0, and radius of curvature, R, in terms of q, as shown in the following equations (Ifflaender, 2001):

$$w_0^2 = -\frac{\lambda}{\pi}\left(\mathrm{Im}\frac{1}{q}\right)^{-1} \quad , \tag{42}$$

$$R = \left(\mathrm{Re}\frac{1}{q}\right)^{-1} \quad . \tag{43}$$

The complex beam parameter in conjunction with the ABCD methodology provides a first order approximation in paraxial optical systems.

In order to describe ray propagation throughout an optical system, the ABCD matrix system was devised. Also referred to as ray matrices, they are widely used to describe the propagation of geometrical optical rays through paraxial optical elements (Siegman, 1986). A beam can be characterized at any point in its path along the optical axis by knowing the angle ϕ formed with the optical axis, and the axial distance d_1 relative to a given reference point. However, this method will only hold for systems

where the angle ϕ is small, this is frequently referred to as the paraxial approximation. Mathematically, this approximation is valid if the following condition is met:

$$\sin\phi \cong \tan\phi \cong \phi \quad . \tag{44}$$

If the beam starts at an arbitrary origin, the curvature can be determined by

$$R_1 = \frac{d_1}{\phi_1} \quad , \tag{45}$$

where d_1 is the distance from reference point, and ϕ_1 is the angle measured from the reference axis. If the beam travels further down the propagation path a distance L, the parameters d_1 and ϕ_1 change according to

$$d_2 = (1 \times d_1) + (L \times \phi_1) \quad , \tag{46}$$

$$\phi_2 = (0 \times d_1) + (1 \times \phi_1) \quad , \tag{47}$$

respectively. Equations 46 and 47 can be combined in a single matrix equation (Ifflaender, 2001)

$$\begin{vmatrix} d_2 \\ \phi_2 \end{vmatrix} = \begin{vmatrix} 1 & L \\ 0 & 1 \end{vmatrix} \begin{vmatrix} d_1 \\ \phi_1 \end{vmatrix} \quad , \tag{48}$$

and in general terms using the ABCD matrix, as

$$\begin{vmatrix} d_2 \\ \phi_2 \end{vmatrix} = \begin{vmatrix} A & B \\ C & D \end{vmatrix} \begin{vmatrix} d_1 \\ \phi_1 \end{vmatrix} \quad . \tag{49}$$

The coefficients A, B, C, and D, characterize the paraxial focusing properties of the element in consideration. With these definitions we can connect input and output displacements and slopes for a variety of paraxial optical elements (Siegman, 1986).

The propagation of a beam through any material that is homogenous and isotropic can be represented by its "*M*" matrix that is equal to

$$M = \begin{vmatrix} A & B \\ C & D \end{vmatrix} \quad . \tag{50}$$

Thus, any first order optical element, e.g., lens, mirror, etc., can be represented by the equivalent *M* matrix. Common forms of the matrix for various situations can be found in Ifflaender (2001). Also, the ray matrix determinant of any basic element must satisfy the following relation when using the generalized slope definition (Siegman, 1986)

$$AD - BC = 1 \quad . \tag{51}$$

The equivalent *M* matrix for a system of optical elements is equal to the product of the matrices representing each element. Going back and reexamining the complex beam parameter shown in Eq. 40, we can now define it in terms of an ABCD matrix as

$$q_2 = \frac{Aq_1 + B}{Cq_1 + D} \quad . \tag{52}$$

This allows the *q* value to be transformed by optical elements in the system. The equations that transform the beam parameters are (Ifflaender, 2001)

$$\frac{1}{R_2} = \frac{\dfrac{AC + (AD + BC)}{R_1} + BD\left(\dfrac{1}{R_1^2} + \dfrac{\lambda^2}{\left(\pi w_1^2\right)^2}\right)}{\left(A + \dfrac{B}{R_1}\right)^2 + \left(\dfrac{B\lambda}{\pi w_1^2}\right)^2} \quad , \tag{53}$$

where *R* is the radius of curvature. The beam size w_2, is determined by

$$w_2^2 = w_1^2\left[\left(A + \frac{B}{R_1}\right)^2 + \left(\frac{B\lambda}{\pi w_1^2}\right)^2\right] \quad , \tag{54}$$

and the divergence angle, θ is

$$\theta^2 = w_1^2\left[\left(C + \frac{D}{R_1}\right)^2 + \left(\frac{D\lambda}{\pi w_1^2}\right)^2\right] \quad . \tag{55}$$

Equation 52 will allow us, with the knowledge of the complex beam parameter at a specified point, to propagate the beam through any arbitrary optical elements or systems and recalculate the new *q*-value at a chosen location, thus being able to also determine new beam size and divergence values (Newport, 2002b).

8. CAUSTIC MEASUREMENT ON Nd:YAG LASER

In order to be able to determine the focal shift in the laser crystal, measurements will need to be performed on an operational laser device. The caustic of the laser beam will be measured at varying power levels through the operating range of the device. In order to mount the required beam analyzer the laser had to undergo minor modifications in order to accept the new instrumentation. The functionality of the original instrumentation and expanded capability of the additional PRIMES beam analyzer are explained in Section 8.1.

8.1. Methodology

Measurements were carried out utilizing a single cavity HAAS laser system, capable of generating over 750 W of power, Fig. 8.1. The laser was configured to allow for power measurements utilizing a Coherent power meter and the ability to view the YAG beam by means of a CCD camera. However, for this experiment, the expanded capabilities of this diagnostic equipment were not required. Output power of the laser was not a measured parameter during the course of this experiment. Moreover, the viewing capabilities of the CCD camera were limited when compared to the PRIMES measurement device. The CCD camera was only capable of producing a two-dimensional picture, while the PRIMES FocusMonitor generated a three-dimensional representation. Thus, neither the power measurement device nor the CCD camera were used in the course of conducting experimental trials. The laser unit offered several

options for guiding the beam. The possible beam paths and measurement devices are shown in Fig. 8.2.

Fig. 8.1. TRUMPF HL506D laser (TRUMPF, 2002).

Because a plane wavefront YAG laser beam was not available for direct measurement of the crystal sensitivity factor, the following approach was used. The YAG beam was generated using a single cavity resonator with plane AR and HR mirrors. The power dependent focal length of the YAG crystal was therefore influenced by the resonator parameters g_1 and g_2. For a symmetrical resonator, these parameters are defined as (Koechner, 1999)

$$g = g_1 = g_2 = 1 - \frac{L}{2f} \quad , \tag{56}$$

where L is the length of the resonator, and f is the focal length of the YAG crystal. Because of the variation in the focal length of the crystal, the waist size of the laser beam

is dependent on the pump power. By measuring the waist size at a point outside of the resonator and propagating the beam backwards to the AR mirror, the pump power dependent focal lengths and thereby the crystal sensitivity factors were determined.

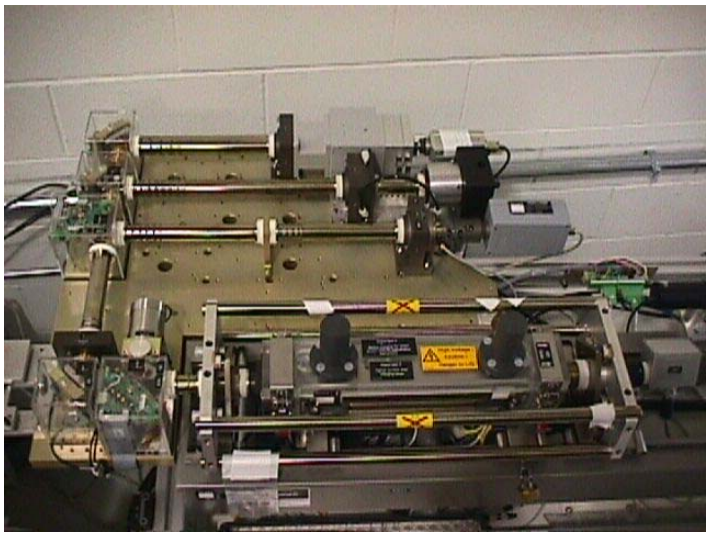

Fig. 8.2. Configuration of the HL506D laser.

Measurement of these parameters was accomplished by determining the beam focusability factor, M^2. The derivation of the beam propagation factor and the beam focusability factor can be summarized using the following relations (DIN, 1999)

$$K' = \frac{1}{M^2} = \frac{4\lambda_0}{\pi} \frac{1}{n w_{T0} \theta} = \frac{4\lambda}{\pi} \frac{1}{w_{T0} \theta} \quad , \tag{57}$$

where K' is the beam propagation factor, M^2 is the beam focusability factor, λ_0 is the wavelength of beam in a vacuum, λ is the actual wavelength of beam, θ is the divergence angle of the beam, w_{T0} is the beam waist radius, and n_0 is the index of refraction along the axis of the crystal.

A beam analyzer system was used to measure the M^2 factor. Because the M^2 factor is an invariant property of the laser beam, the waist radius can be propagated backwards to the outcoupler mirror. At this point, the focal length was determined as a function of the beam waist size. The change in the focal length was then used in conjunction with the change in input power to determine the crystal sensitivity factor.

8.2. Measurement procedure

In this thesis, the YAG beam was analyzed using a PRIMES FocusMonitor system. This system along with the accompanying software package is capable of a multitude of measurements. Of interest in this thesis were the measurements of the beam waist size located at the focal point, and the beam focusability factor. Custom fixtures were fabricated to attach the FocusMonitor and absorber to the laser device shown in Fig. 8.3. The YAG beam, as it emerged from the resonator was propagated through a focusing element used to ensure that the beam does not become too large for the measuring device. It was also important that the power density was high enough so that the signal to noise ratio was greater than 10-20 to 1, this allowed the FocusMonitor to effectively measure the beam. Upon passing through this lens shown in Fig. 8.4, the beam encountered a second 90º bending mirror that bent the beam in the direction of the PRIMES system. The beam then passed through the analyzer and entered the absorber.

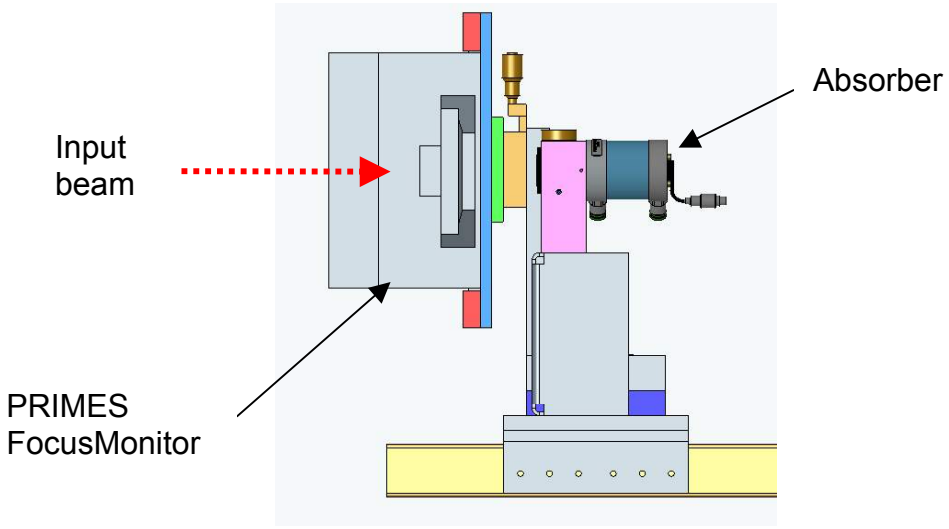

Fig. 8.3. Model of the measuring apparatus and mounting fixtures.

A schematic of the entire system is shown in Fig. 8.4. The preliminary experimental setup used in order to verify feasibility of the measurements is shown in Fig. 8.5.

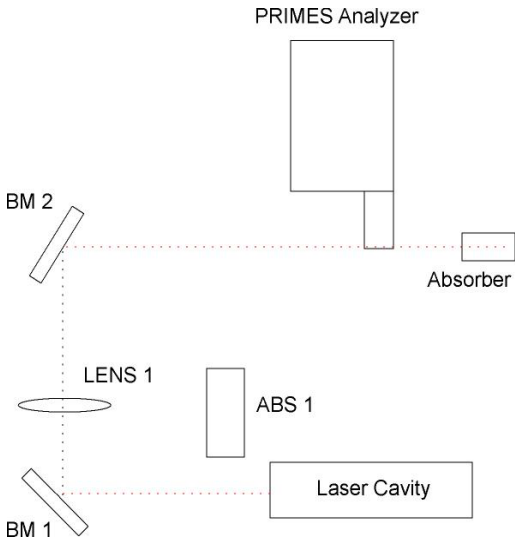

Fig. 8.4. Experimental setup used with PRIMES FocusMonitor.

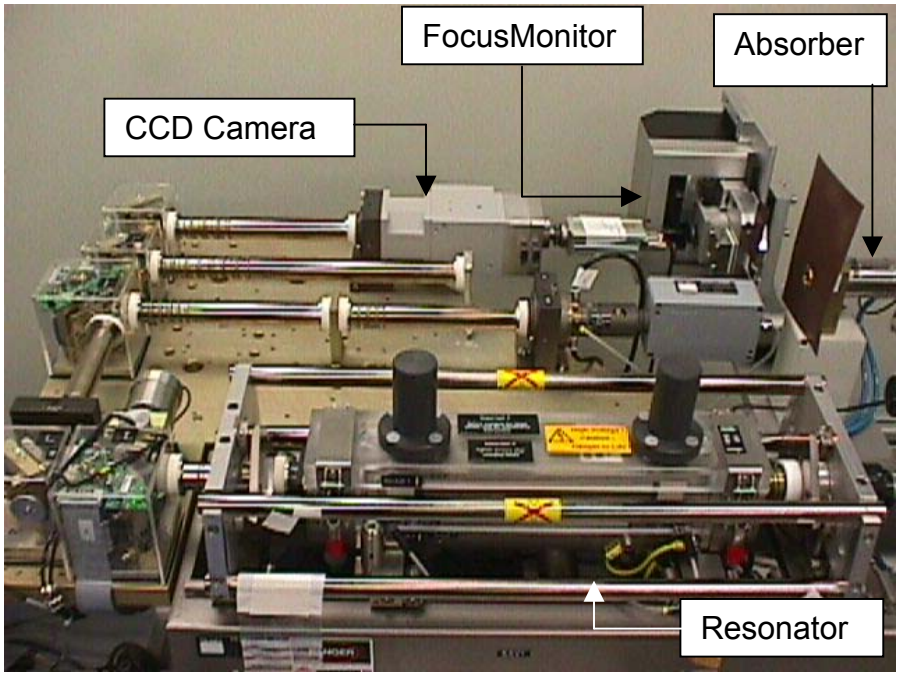

Fig. 8.5. Preliminary experimental setup.

8.2.1. PRIMES system operation

The current state-of-the-art measuring systems are capable of measuring all of the essential parameters of the beam. The best and most comprehensive systems have a provision to allow for measurements of the beam caustic that is of vital importance in almost all laser applications. The PRIMES FocusMonitor analysis system, Fig. 8.6, consists of a rotating measuring tip that samples the beam during each revolution. The tip is located within a movable platform that also houses the detector unit, this stage is allowed to move away from the PRIMES housing in order to sample the beam. At the top end of the measuring tip, a minute hole is located through which a small potion of the

beam is extracted for measurement, Fig. 8.7. Movement is also possible in the *Z* direction (35mm working range) that allows for measurements throughout the beam caustic.

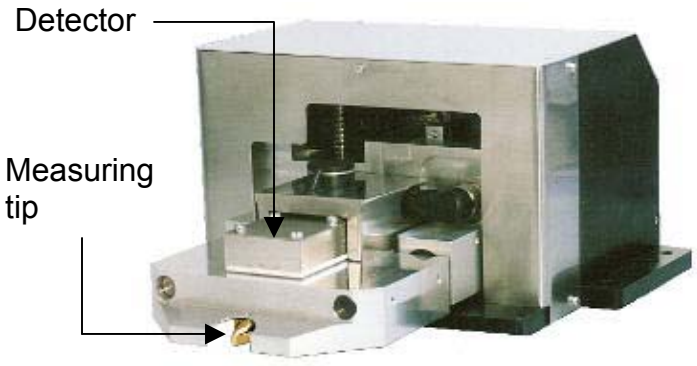

Fig. 8.6. PRIMES FocusMonitor (PRIMES, 2002).

Using two mirrors, the sampled beam is guided to a stationary detector, as shown in Fig. 8.7. The signal generated on the detector is digitized and analyzed by software algorithms. Measurements are repeated at multiple points within the working range of the *Z*-axis of the FocusMonitor. Readings are taken in accordance to guidelines set forth by ISO standard 11146 (PRIMES, 2002). The device will analyze the beam within a span of at least four Rayleigh ranges and generate a graphical representation of the beam caustic. Because of the large span over which the beam is measured and the variation of the power intensity, the signal to noise ratio must not be lower than 10:1; values lower than this will not allow the device to distinguish the beam from the ambient conditions.

The results of the caustic measurement are presented in graphical format for the user. The FocusMonitor will automatically determine the focal point location of the beam along with the beam size, the beam focusability factor, and the Rayleigh range.

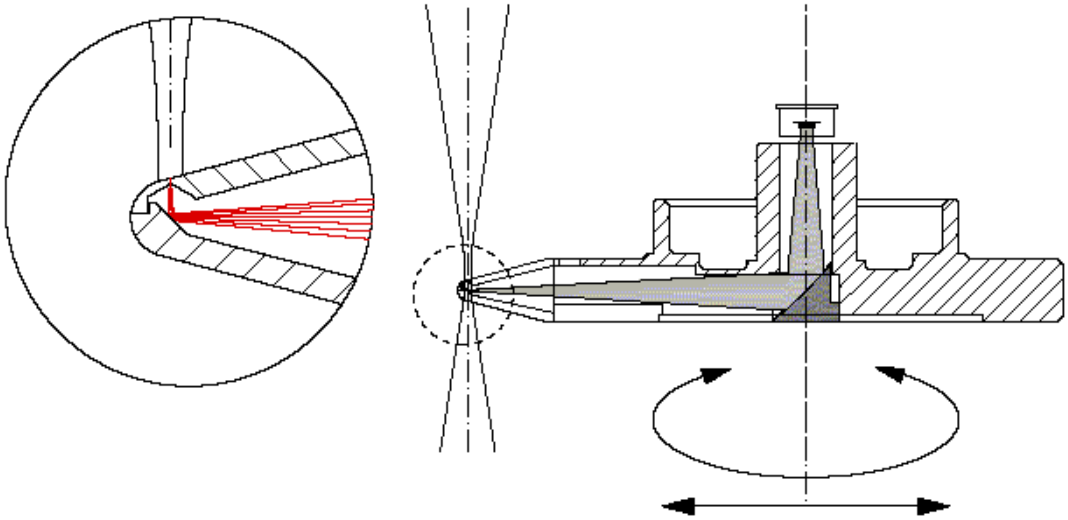

Fig. 8.7. Beam entrance to the FocusMonitor (PRIMES, 2002).

A two-dimensional representation of the beam diameter is also provided. The beam radius and the M^2 factor provided at the focus point, were used to reverse propagate the beam to the AR mirror.

8.2.2. Measured parameters

The FocusMonitor should be optimally positioned so that the focus point of the beam will be located roughly in the middle of the working range of the device. This allows the FocusMonitor to measure the caustic of the beam. Using the software provided by PRIMES, a multitude of measured parameters is available for use. Allowing the device to complete a caustic measurement cycle results in a total graphical

representation of the beam. Of primary importance is the resultant M^2 value of the beam. As already noted this is an invariant property of the beam and, as such, the variables that determine the value of the beam focusability factor are extremely useful. Because the M^2 factor is calculated directly from the waist size within the resonator, this information is used to calculate the focal length of the crystal.

8.2.3. Calculation procedure

By changing the input power, the beam size at the output mirror is affected due to the varying thermal lens inside the crystal, thus directly influencing the beam size, w_0 at the measuring point. By making use of beam propagation laws, and calculating the beam size in the resonator from the measured beam radii, it is possible to determine the resonator parameters as a function of input power by utilizing (Koechner, 1999)

$$w_1^2 = \left(\frac{\lambda L}{\pi}\right)(1-g_2)^{-1/2} \quad , \tag{58}$$

where L is the resonator length, λ is the wavelength of beam, and g_2 is the resonator parameter. Using the resonator parameter from Eq. 58, the focal length of the thermal lens formed is equal to

$$f = -\frac{1}{2}\frac{L}{(g_2 - 1)} \quad . \tag{59}$$

With the focal length of the crystal, based on Eq. 59 it is possible to determine the crystal sensitivity factor from Eq. 32.

8.2.4. Analytical calculations

The results obtained from the experiments were compared to theoretical values obtained by following the procedures outlined in Section 6.2, and demonstrated in Appendix A. In order to determine the heat generation by the system, additional information was collected from the laser. The crystal temperature, as well as input and output coolant temperatures, were required to calculate the amount of heat removed from the crystal. Using this information and the material properties for the laser crystal, it is possible to determine the theoretical focal length of the laser crystal based on the input power.

9. EXPECTED USES FOR RESULTS

Results obtained in the thesis will serve to improve the production process for the Nd:YAG lasers. By testing the optical behavior of each crystal prior to installation in a production laser, it should be possible to establish a general range of acceptable crystal sensitivity factors and focal lengths that are suitable for use in a laser device. This will ensure that the crystals in each laser will exhibit approximately the same optical characteristics. As a result of this, the alignment process will be simplified and may proceed at a much faster pace. Because the quality of the crystals would be verified off-line from the production line, final assembly and testing time would also be reduced. Further evaluation of the crystal sensitivity factor may lead to its establishment as a material parameter that could be specified to the vendor. This would be particularly important during the design stages for new lasers or the optimization of current products. This factor may also be utilized to determine the optimal pumping power into each cavity. By having a relation between the focal point and the pump power, and also knowing the optimal location of each focal point, it may be possible to optimize the pump characteristics of the laser to ensure optimal beam coupling between each cavity and thus maximize power output.

10. EXPERIMENTAL PROCEDURE

The procedures used to measure the laser beam are presented in sections below. Several experimental factors, however, must be mentioned prior to the presentation of the results. Five of the crystals used were tested in their own respective cavity assemblies. The remaining three were installed in a spare cavity that was utilized for test purposes. The laser device, and corresponding optical guidance system, were allowed to reach thermal equilibrium by operating the laser at the rated output power for 15 minutes prior to conducting the experiments. None of the optical components were water cooled. It should also be noted that the input power level deviated from the nominal values during the course of the experiments. However, this variation was at a maximum ± 0.1 kW, and did not produce a significant effect in the measurements.

Multiple attempts were made, in accordance with standardized test procedures outlined in DIN (1999) in order to obtain results that were representative of the complex behavior of the Nd:YAG crystal. Findings and recommendations for future areas to be researched are also presented below.

10.1. Equipment setup and configuration

The PRIMES FocusMonitor was mounted on a fixture that allowed for the translation of the unit in the vertical and horizontal plane. This fixture was then mounted on a linear slide that allowed for the axial position of the device to be varied along the propagation axis of the laser beam. In order to correctly position the device relative to

the beam, an alignment aid was provided with the FocusMonitor package. It consisted of a sheetmetal part with a small hole that corresponded to the location of the beam; when aligned correctly the beam passed through the opening of the sheetmetal part. This allowed the beam to propagate past the FocusMonitor, without interfering with it. To assist in prealignment, the HeNe alignment laser of the HL503D was used. Once the coarse alignment was complete using the supplied alignment aid, it was ensured that the FocusMonitor was positioned perpendicular to the propagation path of the laser beam. This was accomplished by performing a series of tape shots, the procedures for which were outlined in Chapter 6. In order to facilitate the perpendicularity alignment an additional sheetmetal fixture was fabricated. The fixture was fabricated from 2mm sheetmetal with two cross hairs located 150 mm apart. After performing the coarse alignment, the FocusMonitor was removed and the alignment fixture was secured to the FocusMonitor mounting plate. The centers of the cross hairs were designed so that they would coincide with the sampling hole of the measuring tip. The tape shots taken at both cross hairs should appear identical. If this was not the case, adjustments were made to correctly position the FocusMonitor mounting fixtures. Once this step was complete, measurements proceeded further.

Additional tools that were used to assist in the positioning of the components were InfraRed (IR) radiation catchers and IR cameras. They were used to verify the positioning of various components relative to the beam path. The IR catchers used were small reactive plates that glow green when incident IR light strikes the plate. However, due to their small size and power dissipation limitations, only extremely small power

levels were used, typically on the order of two Watts. By use of the IR catcher, it was possible to determine if the beam was incident at the center of a component. This proved particularly useful when positioning the focusing lenses and absorber. The IR camera was also very useful during the measurement cycle of the FocusMonitor. The camera allowed the experimenter to visualize the beam as it was sampled. This provided an additional means to ensure that the beam was at the correct location.

Following the correct positioning of all required components, the laser power was incrementally increased and the system was examined for proper operation. Before measuring the beam with the FocusMonitor, the beam was first allowed to pass through the modified optical system and into the absorber. This was performed in order to ensure that the beam would be incident on the absorber throughout the entire power range. A sheet of photographic paper was affixed along the outer edges of the absorber to aid in the recognition of any stray beams.

10.2. Measurement using the FocusMonitor device

The FocusMonitor has several software settings that must be adjusted prior to using the device. This includes the wavelength of the laser beam to be measured, the axis travel limits that determine the working range of the device, the number of pixels defining the measurement window in each axis direction, and of particular importance, the beamfind settings. The beamfind settings are used by the FocusMonitor to locate the

beam and determine the optimal window size for measurement. A more in-depth review of these settings is presented in Section 10.2.1.

The energy density on the detector was of particular importance to ensure that an adequate signal to noise ratio was achieved. This was very important particularly at low input power levels to ensure that the FocusMonitor does not analyze data that are not specifically a component of the laser beam. At low input powers, the signal to noise ratio was about 4 to 1. This value increased corresponding to the input power to the laser. The signal to noise ratio is recommended to be at least 10 –1 by PRIMES (2002).

10.2.1. Beamfind function of the FocusMonitor

Two components comprise the beamfind settings, they are: the trigger value, and a percent value. The trigger value sets the reference level of the measuring system, and the percent value represents the percentage value by which the trigger value must be breached in order for the FocusMonitor to register a signal. The percentage value is related to the signal to noise ratio required by the detector. For this experiment a trigger value of 150 and a percentage of 15% were used. This allowed the detector to detect a signal with the relatively low input power of 6.5 kW. The beamfind function serves to locate the beam within the operational range of the FocusMonitor. The measurement window is limited to 8x8 mm. Using an internal algorithm, the FocusMonitor initially attempts to locate the laser beam within the largest measuring window. Once the beam is located, the measurement window is decreased in size to zoom in on the area that

encloses the beam. This process is repeated in steps until the window is the minimum size that still captures the entirety of the beam. For Nd:YAG beams, the profile of the beam remained generally circular throughout the majority of the power range. However, when operating under high input power, usually in the vicinity of 15.5 kW and above, two noticeable symmetric "wings" were formed along the outer edge of the beam. These wings tended to elongate the beam along one axis, for which the program must correct. The automatically calculated measurement window settings must be closely monitored for each measurement plane. Generally, the program did a very good job at determining the correct window size, however, attention must be paid to ensure that the window did not clip off any portions of the beam. Clipping of the beam due to incorrect window size was very noticeable, as a much lower M^2 value was generated than would be expected.

10.2.2. Measurement of beam caustic

The FocusMonitor is capable of automatically measuring the beam caustic and determining the characteristic quantities for the laser device. For measurement of the caustic the FocusMonitor was positioned roughly at the focal point of the preceding focusing lens in the optical system. At this location, single measurements were initially performed at low input power to ensure that the device was able to locate the beam using its internal beamfind function. Following this, the caustic was measured with a constant input power to the laser. Measurements were conducted over a span of roughly 10 cm, and data were obtained for a total of 10 planes. For this thesis only a single pass through

the beam was performed at each plane and no averaging of the data was performed. Roughly half of the measurement planes were located on one side of the beam waist and the other half on the opposite side. After the FocusMonitor completed measurements of the caustic, the individual planes were manually reviewed for optimal choice of the measurement window, and altered if necessary. The measurement of a plane was repeated if the measurement window needed to be changed.

The beam caustic was measured at predefined power levels, commencing at 6.5 kW of input power and increasing in 1 kW intervals. The largest input power measured was determined by referring to a power curve for each respective crystal, an example of which is shown in Appendix B. The maximum input power tested was based on where the maximum output power was attained as shown on the power curve.

10.3. Iterations of the experimental design

Several iterations of the experimental setup were performed in order to obtain acceptable results, they are explained further in Sections 10.3.1 through 10.3.3.

10.3.1. Measurement of the raw unfocused beam

The first attempt was to measure the raw beam without installing any additional components to the laser. However, after performing several tape shots in the area where the FocusMonitor was to be located, it was determined that the beam size was too large

for the FocusMonitor. The beam was measured to be approximately 12 mm in diameter. However, the limitations of the FocusMonitor limit the maximum beam size to 8 mm square. Thus, the raw beam could not be measured using the FocusMonitor, additionally the energy density would be much too low at this beam size to be measured accurately.

10.3.2. Measurement of the beam using a lens with f = 398.6 mm

In order to focus the beam to decrease the spot size and increase the energy density, a bi-convex lens with a focal length of 398.6 mm was mounted on the optical plate of the laser, preceding the FocusMonitor. The FocusMonitor was positioned so that the measuring tip was located roughly at the focal point created by the lens. However, acceptable results were also not attainable using this configuration. The energy density at low input power levels remained too small to allow the beam to be sampled. Readings were obtained at high input power levels near the threshold operating zone of the laser, however this was not acceptable for this experiment.

10.3.3. Measurement of the beam using a lens with f = 98.2 mm

The final experimental configuration is presented in Fig. 10.1. In order to obtain valid results, a focusing lens was required that would allow sampling of the beam through a majority of the power range of the laser device. A plano-convex lens with a focal length of 98.2 mm was installed in the optical path. This resulted in a drastic shortening

of the focal length from the configuration discussed in Section 10.3.2 and enabled the beam to be focused to a smaller spot size. This allowed for drastically smaller beam diameters and correspondingly the energy density was increased to a level that enabled the FocusMonitor to measure the beam effectively. This setup allowed for measurements to be conducted over the majority of the operating range of the laser. Measurements were taken beginning at 6.5 kW of input power. This level was determined to be acceptable as the laser is very rarely operated at such low input power levels. Normal operating conditions of the laser are usually at the maximum rated power. This corresponds to an input power of approximately 13.2 kW and above.

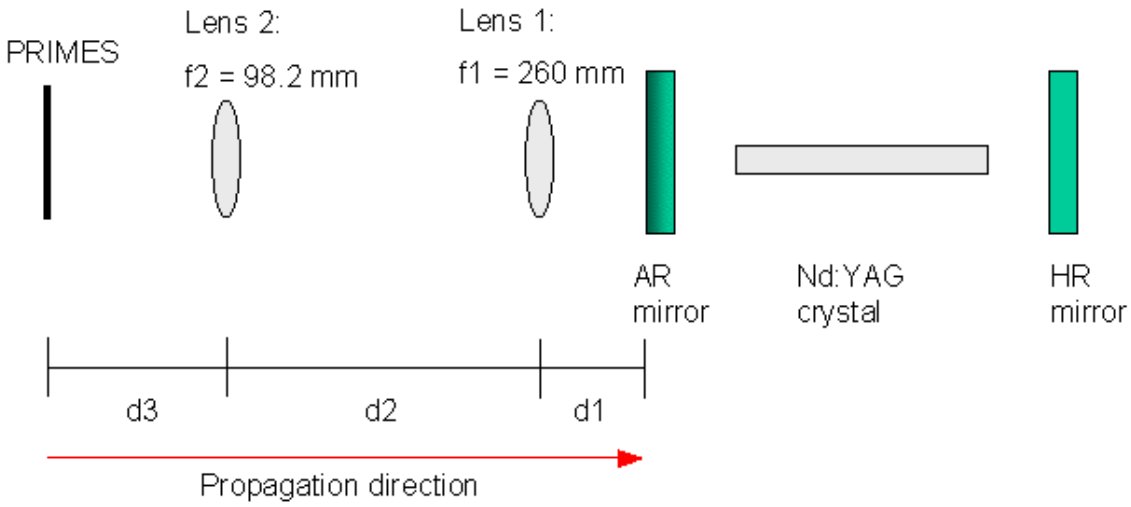

Fig. 10.1. Final experimental configuration.

10.4. Deficiencies in FocusMonitor setup

The FocusMonitor is capable of measuring a Nd:YAG beam with only minor modifications to the OEM configuration. The setup of the FocusMonitor used in this experiment was the minimum required by PRIMES for measurement of Nd:YAG beams. Measurements of the beam were possible using this setup, however, better results arise when using the PRIMES recommended configuration described in Section 10.4.1 (PRIMES, 2002). For the purpose of this thesis the sole modification required was the installation of a special measuring tip purposely designed for the measurement of Nd:YAG beams. The stock pyroelectric detector originally installed on the FocusMonitor was capable of measuring both CO_2 and Nd:YAG laser beams (PRIMES, 2002).

10.4.1. Recommended setup for FocusMonitor

The setup of the FocusMonitor as recommended by PRIMES allows for more accurate measurements of the laser beam characteristics. Measurements conducted using the conventional Nd:YAG tip, will usually conclude that the measured beam is smaller than the actual size (PRIMES, 2002). This is due to the high divergence angle of the beam and the incapacity of the measuring tip to transfer all of this energy to the detector. The divergence of the beam also plays a large role in the sensitivity of the measurements to the incidence angle of the beam onto the FocusMonitor. However, with the acquisition of an appropriate Hi-Div (high-divergence) measuring tip also referred to as an

integrator, or integrating element, the incidence angle sensitivity is drastically reduced (PRIMES, 2002). The sensitivity of the FocusMonitor for both types of measuring tips is shown in Fig. 10.2.

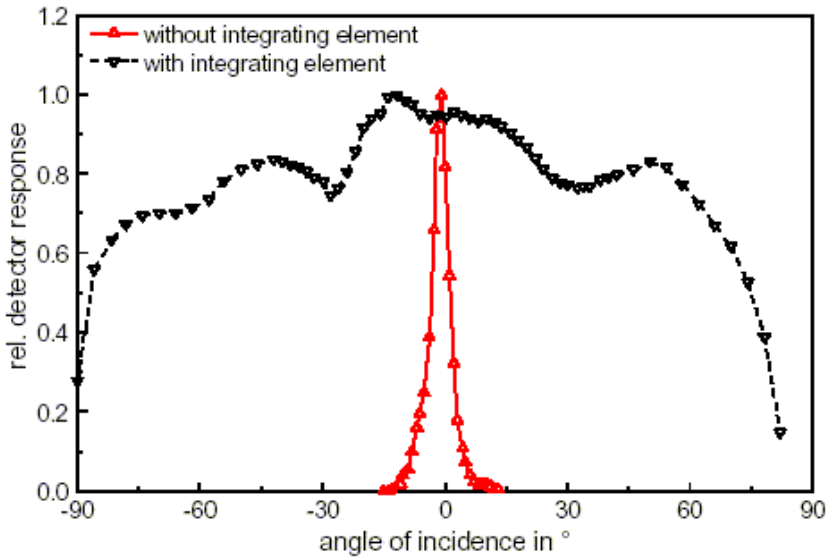

Fig. 10.2. Sensitivity of PRIMES measuring tips (PRIMES, 2002).

The functionality of the Hi-Div measuring tip is best summarized by describing the sampling hole as an integrator that collects information from the beam to be measured. This is accomplished by placing a body of diffuse material directly behind the pinhole. The radiation propagating through the pinhole is then scattered, allowing the beam to spread over a larger area and, in effect, loose the information about the divergence of the sampled beam (PRIMES, 2002). The detector then sees the information passed to it by the integrator. This configuration allows for more flexibility in the experimental setup. The FocusMonitor may be slightly misaligned to the

propagation axis of the beam and still provide meaningful results. The detector that senses the information relayed to it by the measuring tip is also changed to a photodiode detector as opposed to the stock pyroelectric detector; the photodiode detector is particularly well suited for visible to near IR radiation (PRIMES, 2002).

11. EXPERIMENTAL DETERMINATION OF CRYSTAL PARAMETERS

Each crystal was installed and tested in the single cavity laser using the experimental procedures outlined in Chapter 10. The data obtained from the experimental trials were further used to calculate the focal length of each crystal and the crystal sensitivity factors. However, multiple methodologies of the analysis procedure were necessary in order to obtain representative results. The results obtained are presented in Sections 11.1 through 11.3.

11.1. Calculation of the focal length

An integral requirement for the determination of the crystal sensitivity factor is the calculation of the focal length of the crystal. Different methods for calculation of the focal length were employed. The original proposed method is presented in Section 11.1.1 and a modified, more complex version is explained in Section 11.1.2.

11.1.1. Solving for focal length using "*g*" parameters

Using the beam waist radii measured at the FocusMonitor measurement plane, the complex beam parameter was determined. Following through the procedures outlined for the propagation of the *q*-value through optical systems in Chapter 7, the complex beam parameter was determined at the AR mirror, from which the beam radii were determined.

The resonator parameter was then calculated using Eq. 13. After determining the resonator parameter as a function of the input power, the focal length was calculated using Eq. 56.

11.1.1.1. Discussion

Following the calculation procedure outlined in Section 11.1.1, it was determined that the methodology utilized was unacceptable for the requirements of this thesis. The equation used to determine the *g* parameter assumes that a focusing lens is located in the middle of a resonator, and that it remains constant throughout the power range of the laser. However, in the case of a Nd:YAG laser, the lens is governed by the thermal lensing effect that is dependent on the pump power of the laser. The calculations for the *g* parameter resulted in either complex values or values that did not correspond to the stability criteria defined for a resonator. Referring to Fig. 5.4, the results obtained fall in the unstable region of the g_1g_2 stability diagram. An attempt was made to use the real number component of the resonator parameter in subsequent calculations to determine the focal length. However, the values obtained did not correlate well to values that have been previously published in reference material. As a consequence of these calculations, it was determined that another methodology to model the behavior of the thermal lens was required.

11.1.2. Solving for focal length using self-repeating "*q*" parameter

Due to the inadequacy of the methodology described in Section 11.1.1, another method was developed that would model the thermal lensing effect and the behavior of the laser beam as it propagates through the resonator more effectively. The same procedure as in Section 11.1.1 was followed to determine the *q*-value at the AR mirror, at which point the beam size was also determined. However, at that point new concepts were utilized in order to develop the resonator model. Using the stable quadratic duct model of the YAG crystal, an equivalent ABCD matrix for the resonator was developed. The definition of the stable quadratic duct is based on the n_2 parameter that was discussed in Section 6.2. However, this parameter is difficult to use and interpret. Therefore, after an additional review of literature, another parameter was chosen to be used in the definition of the duct. This parameter is referred to as the characteristic focal length of a crystal, β, and is defined as (Schlueter and Markille, 2002)

$$\beta = \sqrt{\frac{4n_0}{n_2}} \tag{60}$$

where n_0 is the index of refraction, and n_2 is the downward curvature. The matrix defining the quadratic duct is (Ifflaender, 2001)

$$YAG(b) = \begin{bmatrix} \cos(bz) & (bn_0)^{-1}\sin(bz) \\ -n_0 b \sin(bz) & \cos(bz) \end{bmatrix} , \tag{61}$$

where b is as defined in Eq. 23. For the purpose of this thesis, the transverse derivative was replaced by the characteristic focal length of the crystal using the following relation:

$$b = \frac{2}{\beta} \quad . \tag{62}$$

Therefore, the matrix defined in Eq. 61 was rewritten to be expressed in terms of the β parameter. The resultant matrix for a quadratic duct is

$$YAG(\beta) = \begin{bmatrix} \cos\left(\frac{2}{\beta}z\right) & \left(\frac{2}{\beta}n_0\right)^{-1}\sin\left(\frac{2}{\beta}z\right) \\ -n_0\frac{2}{\beta}\sin\left(\frac{2}{\beta}z\right) & \cos\left(\frac{2}{\beta}z\right) \end{bmatrix} \quad . \tag{63}$$

Using the criteria for a stable resonator and self-repeating q-value defined in Section 5.1 it is known that the q-value at the AR mirror must self-repeat after a roundtrip pass through the resonator. This requirement must be fulfilled in order to have a stable, functional resonator. Knowing the complex beam parameter value at the AR mirror, the equivalent matrix can be solved for the β parameter that will allow for a self-repeating q-value. The necessary calculations for a sample crystal are presented in Appendix D.

After determining the complex beam parameter values for each corresponding pump power and solving for the corresponding β values, the resultant values for the characteristic focal length were used to model the thermal lensing effect in the crystal. The calculated β values were substituted in the matrix representing the stable quadratic duct. This resulted in a different matrix representing the duct for each corresponding pump power level. The q-value at the AR mirror was then propagated through this system to the HR mirror. Using the q-value propagated through the resonator, the beam radius was determined as a function of position within the resonator. Results of the calculations for two sample laser crystals are shown in Fig. 11.1. Crystal number 261067

passed all quality control measures and crystal number 261787f exhibited an unnatural beam profile when installed in a 4 kW laser device.

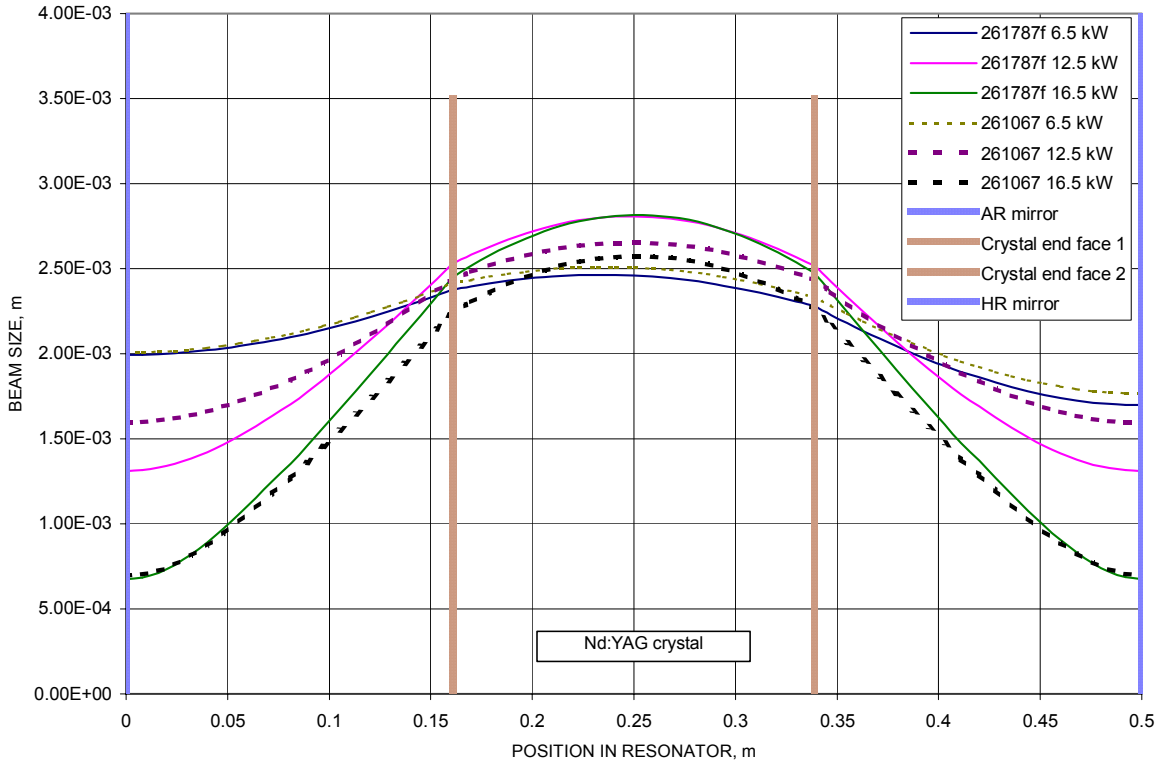

Fig. 11.1. Beam size in resonator as a function of input power.

11.1.3. Analysis and discussion of results

In performing the calculations required to determine the beam size within the resonator, several issues needed to be addressed that deal with the errors associated with the calculations. The largest source of error arises from determination of the propagation distances between optical elements. It was noted during calculation of the q-value at the AR mirror that there was always a real number component to the q-value, this can be

seen in Appendix D. This signifies that the beam has a finite curvature at the AR mirror. By definition, a beam waist is formed when the beam has a planar wavefront, thus the curvature of the beam should be infinite. This would require the real number component of the complex beam parameter to have a value of zero. The definition of a stable resonator with plane mirrors states that a beam waist must always be formed at the mirrors. Thus, the complex beam parameter should have a purely imaginary value at the AR mirror. After some analysis of the results it was determined that the distances between the optical components had the largest influence on this behavior. Because of this effect, the matrices representing the variable distance formed between the focal point and lens #2, Fig. 10.1, were adjusted to minimize the real component of the complex beam parameter. The adjustment distance was approximately 10 mm. The presence of wavefront curvature of the beam at the AR mirror also affects the symmetry of the beam size within the resonator. Larger values of beam curvature tend to shrink the beam size at the HR mirror and produce an asymmetric beam size profile.

After a closer examination of Fig. 11.1 it is seen that at the medium input power level, i.e., 12.5 kW, the accepted and rejected crystals have different beam radii at the AR mirror. This difference is also visible at the HR mirror and is more pronounced than the difference for the low or high input power plots. This input power value falls into a fragile operating region of the resonator. In the range of 8-12 kW of input power the resonator travels through the confocal point on the g_1g_2 diagram shown in Fig. 5.4 (Kumkar, 2002). This instability is further demonstrated in Fig. 11.2 where the focal lengths for all crystals are shown to vary unpredictably.

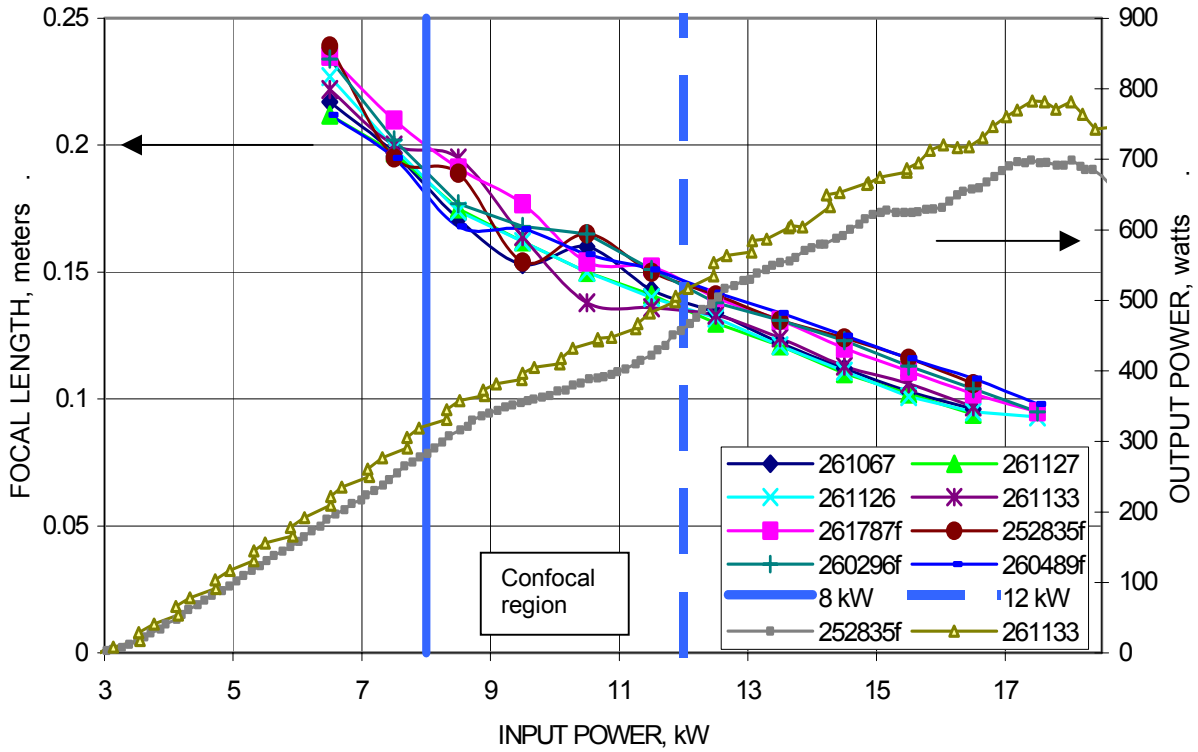

Fig. 11.2. Focal length as a function of input power.

Also, crystal number 261787f showed larger beam sizes within the crystal for input powers of 6.5 kW and 12.5 kW when compared to crystal number 261067. The larger beam sizes for the faulty crystal may be acting detrimentally on its performance when it is installed in a multi cavity laser.

The resonator and crystal models, however, remain approximations for the actual behavior of each respective component. The models do not take into account the non-pumping of the end sections of the crystal, nor any end face deformations. Also not included are any effects due to the birefringence of the crystal. Future incorporation of these factors into the model, presented as part of this thesis, may serve to provide a more

realistic representation of the resonator. However, the additional complexities in determining the effects of each factor and the modeling methodology may offset this benefit.

11.2. Solving for crystal sensitivity parameter

Using the values obtained for β to model the thermal lensing effect, it was possible to calculate the focal length of the crystal. Utilizing the approximation that the focal length of the crystal is longer than the length of the crystal, and that the crystal exhibits behavior similar to a thick lens, the focal length can be expressed as (Koechner, 1999)

$$f = \frac{\beta^2}{4n_o L} \quad . \tag{64}$$

Using Eq. 64 the focal length of each crystal can be plotted as a function of input power. This is presented graphically in Fig. 11.2. After examination of the figure, it can be seen that no concrete criteria can be established to assist in the judgment of bad crystals from good. Six of the eight crystals examined exhibit behavior in the region of 8-12 kW of input power that does not follow the general pattern prevalent after 12 kW. However, because the resonator is traveling through the confocal point in this region, behavior in this range should be not used as a quality control measure. The input power of 13.2 kW is marked on all figures, as this represents the typical working region of the laser.

Data from Koechner (1999) states that the focal power is approximately proportional to the input power, i.e.,

$$f \propto P_{in}^{-1.5} \quad . \tag{65}$$

However, in the case of the crystals evaluated as part of this thesis, the relations of the focal length to the pump power, $f(P_{in})$, were calculated to be slightly different than shown by Eq. 65, and are listed in Table 11.1, where R^2 is the correlation coefficient. This difference however, can be attributed to the difference in the characteristics of the crystals tested as part of this thesis, and those from which the published data were determined. The published data were presented for a shorter crystal and no information was provided about the dopant ratio, or type of cavity used. These factors may play an important role in the focal power of a crystal.

Table 11.1. Focal length functions of pump power.

Crystal #	Power fit curve (Ax^b)	A	b	R^2
261787f	$1.2942x^{-0.8948}$	1.2942	-0.8948	0.988
252835f	$0.9945x^{-0.7842}$	0.9945	-0.7842	0.9661
260489f	$0.8305x^{-0.7178}$	0.8305	-0.7178	0.9672
260296f	$1.1247x^{-0.8393}$	1.1247	-0.8393	0.9796
Average		*1.061*	*-0.809*	*0.975*
STDDEV		*0.1966*	*0.0758*	*0.011*
261067	$1.0725x^{-0.8427}$	1.0725	-0.8427	0.9727
261126	$1.2392x^{-0.9037}$	1.2392	-0.9037	0.993
261127	$1.123x^{-0.866}$	1.123	-0.866	0.9864
261133	$1.1954x^{-0.8842}$	1.1954	-0.8842	0.9766
Average		*1.158*	*-0.874*	*0.982*
STDDEV		*0.0742*	*0.026*	*0.009*

From Fig. 11.2 we can see that the focal length of the crystal follows the same trend after the input power has been increased past approximately 12 kW and the resonator has emerged from the confocal region. This trend remains generally linear. Two groups were formed that distinguish the good and bad crystals. In order to further investigate the quality of crystals, the average focal lengths for both good and bad crystals were calculated and compared, Fig. 11.3. The average values for the focal lengths of good and bad crystals along with the standard deviations are shown in Tables 11.3 and 11.4, respectively. Further examination of Fig. 11.3 does indeed show that good and bad crystals each occupy a distinct region. Taking into account the standard deviation (± 1 S.D.) to obtain a 68% confidence interval, obtained by using the standard deviation for each measured power level, it can be seen that both good and bad regions occupy different regions of the plot within this confidence interval. The average standard deviation values for good and bad crystals were 0.004 m and 0.005 m respectively.

Observing that the pattern after 12 kW remains close to linear, the intercept at which the average focal length crosses the 12 kW mark was examined. This was calculated using a linear regression based on the average values for input powers greater than 12 kW, shown in Fig. 11.3. The group of good crystals intercepted the 12 kW point at 0.1342 m, and the group representing the bad crystals at 0.1446 m.

The differences in the intercepts and the separation of good and bad focal length curves within the 68% confidence interval suggest that the focal length may be used as a crystal characterization tool. In order to separate the two regions, the average value was determined at power levels greater than 12 kW based on the average values for good and

bad crystals. Following this, a linear line based on the average value of all crystals measured with an equation of $y = -0.0085x+0.2414$ was fit to this curve with an R^2 value of 0.994, also shown in Fig 11.3. The average focal length of all crystals tested, is shown in Table 11.2. Although it may not be possible to draw an explicit conclusion directly from the focal length of the crystal, it may be possible to use the focal length in conjunction with other parameters to separate good and bad crystals.

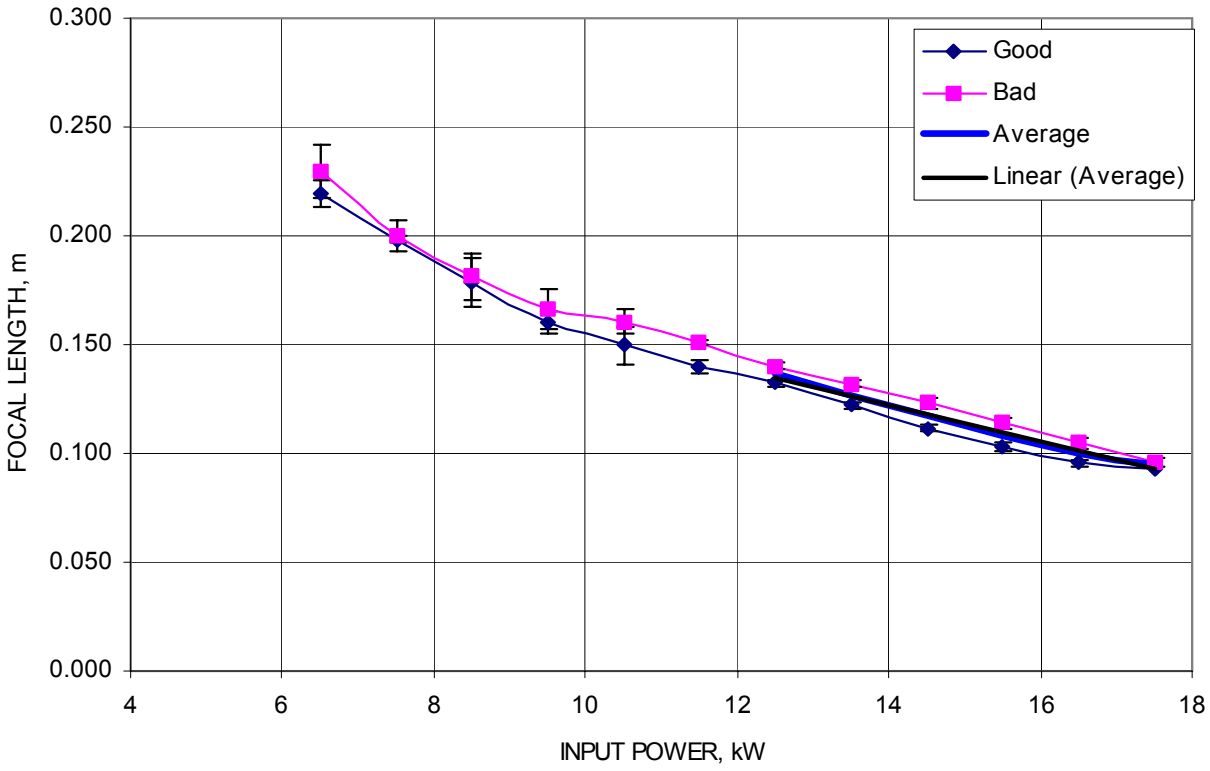

Fig. 11.3. Average focal length.

Table 11.2. Average focal length of all crystals

Input power (kW)	Average values good (m)	Average values bad (m)	Midpoint average (m)
12.5	0.132	0.140	0.136
13.5	0.122	0.132	0.127
14.5	0.112	0.123	0.117
15.5	0.103	0.114	0.109
16.5	0.096	0.105	0.100
17.5	0.093	0.096	0.095

Table 11.3. Focal length values for good crystals.

	Crystal number					
Input power (kW)	261067 (m)	261127 (m)	261126 (m)	261133 (m)	Average (m)	Std dev (m)
6.5	0.217	0.212	0.227	0.222	0.219	0.006
7.5	0.197	0.197	0.199	0.2	0.198	0.002
8.5	0.171	0.175	0.174	0.195	0.179	0.011
9.5	0.153	0.162	0.162	0.164	0.160	0.005
10.5	0.16	0.15	0.15	0.138	0.149	0.009
11.5	0.143	0.141	0.14	0.136	0.14	0.003
12.5	0.134	0.13	0.132	0.133	0.132	0.002
13.5	0.122	0.121	0.121	0.124	0.122	0.001
14.5	0.112	0.11	0.111	0.113	0.112	0.001
15.5	0.103	0.102	0.101	0.106	0.103	0.002
16.5	0.096	0.094	0.095	0.097	0.096	0.001
17.5			0.093		0.093	
Average					0.042	0.004

Table 11.4. Focal length values for bad crystals.

	Crystal number					
Input power (kW)	252835f (m)	261787f (m)	260296f (m)	260489f (m)	Average (m)	Std dev (m)
6.5	0.239	0.235	0.234	0.212	0.23	0.012
7.5	0.195	0.21	0.202	0.195	0.201	0.007
8.5	0.189	0.191	0.177	0.168	0.181	0.011
9.5	0.154	0.177	0.168	0.167	0.167	0.009
10.5	0.165	0.154	0.165	0.157	0.160	0.005
11.5	0.15	0.152	0.151	0.151	0.151	0.001
12.5	0.141	0.14	0.138	0.142	0.140	0.002
13.5	0.131	0.131	0.131	0.134	0.132	0.002
14.5	0.124	0.12	0.123	0.125	0.123	0.002
15.5	0.116	0.111	0.113	0.116	0.114	0.002
16.5	0.106	0.102	0.104	0.108	0.105	0.006
17.5		0.095	0.095	0.098	0.096	0.002
Average					0.040	0.005

Using the data obtained for the focal lengths of each crystal, the crystal sensitivity factor was determined using Eq. 32. The calculations required to determine the factor are presented in Appendix E. A graphical representation of the crystal sensitivity factor is shown in Fig. 11.4.

Referring to Fig. 11.4, the behavior of the crystal sensitivity factor within the confocal region of the resonator remains unpredictable, much like the other parameters. However, after passing through the 12 kW point and into the typical working range of the laser, the factor levels out for both good and bad crystals. Because the crystal sensitivity factor does not show distinguishable regions for acceptable and faulty crystals, it cannot be used as a classification parameter.

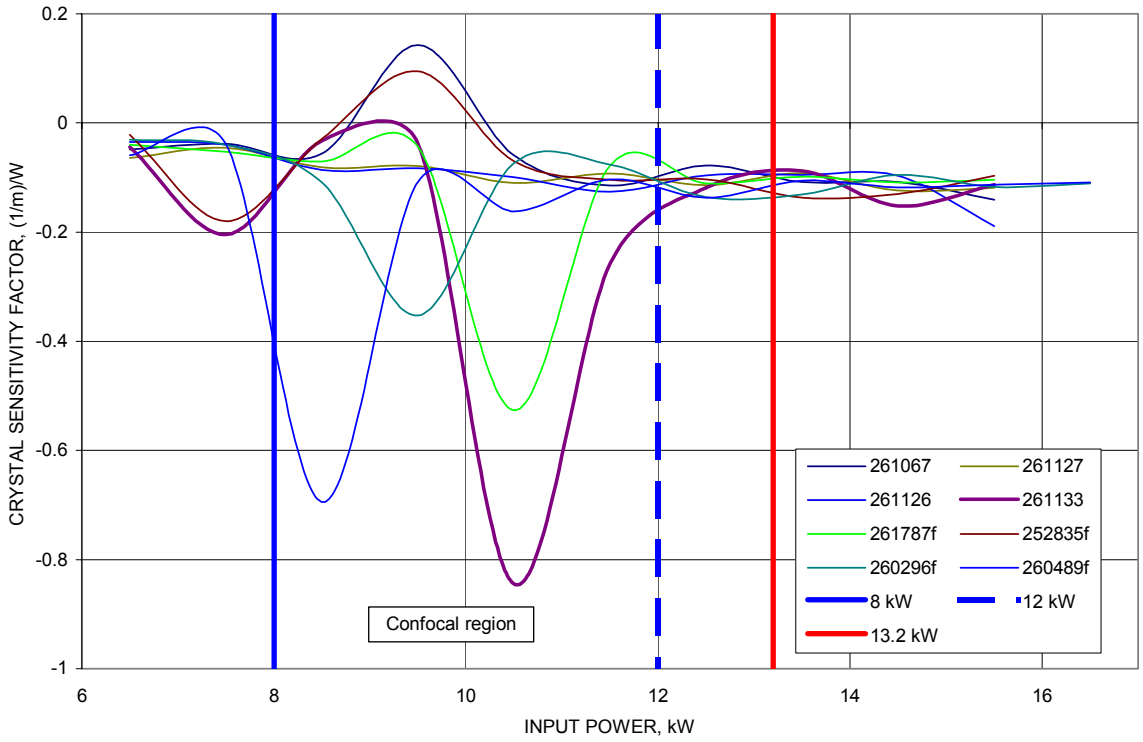

Fig. 11.4. Crystal sensitivity parameter.

11.3. Measurement of the M^2 factor

The measurement of the beam focusability factor as a function of input power was performed simultaneously with other measurements due to the functionality of the FocusMonitor. The M^2 values were calculated based on the published ISO standards using the second order moments of the energy distribution. M^2 values were obtained at each measured power level. Results for all measured crystals are shown in Fig. 11.5.

From Fig 11.5 it is seen that all crystals exhibit unpredictable behavior within the confocal region of the resonator. Because this region is not the normal operating region for the laser device in which the crystals will be installed, conclusions should not be

drawn based on this region alone. Typical input power for a crystal when installed in a 4 kW device is approximately 13.2 kW. Reviewing Fig 11.5 again, it can be seen that the M^2 values at this point all begin to decrease.

The M^2 data presented in Fig. 11.5 appears to follow a quadratic profile. Thus, trend lines were determined for each M^2 plot to aid in developing a tolerance for the separation of good and faulty crystals. The quadratic equations obtained, along with the correlation factors are presented in Table 11.5.

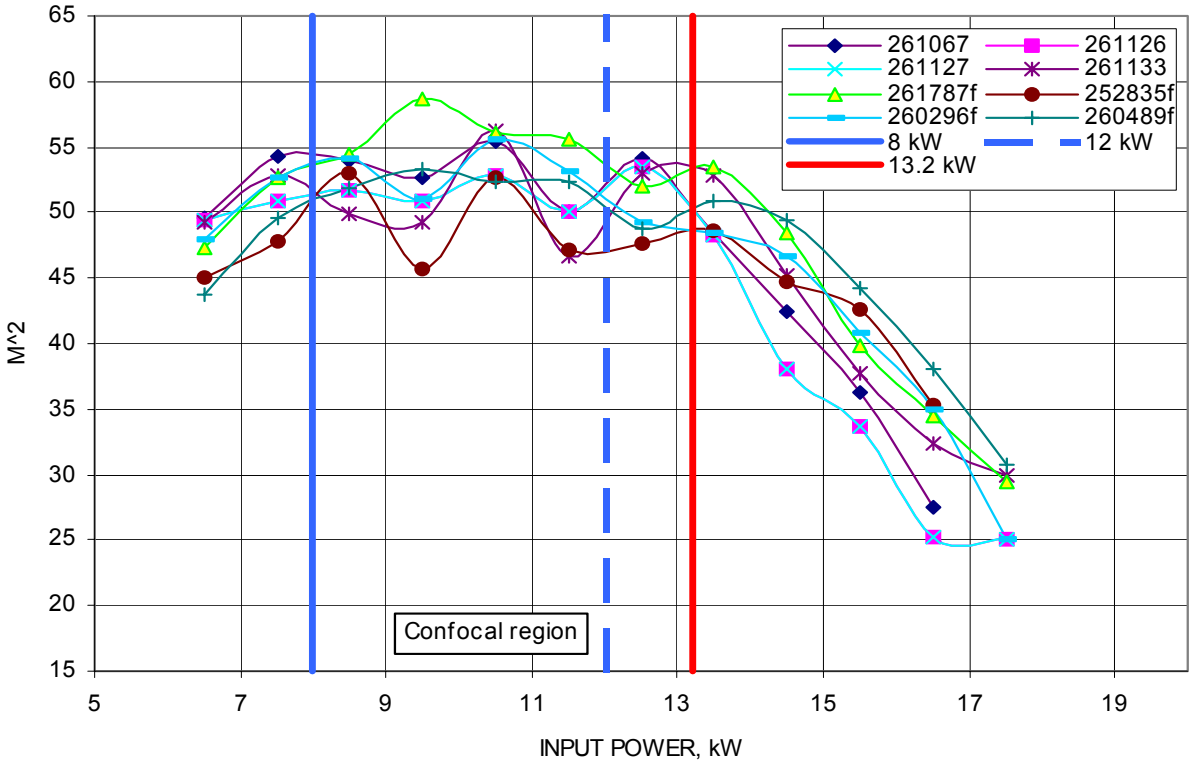

Fig. 11.5. Beam focusability factor.

Table 11.5. Quadratic fit to M^2 data.

Crystal #	Quadratic fit equation (Ax^2+Bx+C)	A	B	C	R^2
261787f	$-0.5686x^2 + 11.814x - 4.5817$	-0.5686	11.814	-4.5817	0.9719
252835f	$-0.3383x^2 + 6.9319x + 14.785$	-0.3383	6.9319	14.785	0.7563
260489f	$-0.4729x^2 + 10.197x - 1.5206$	-0.4729	10.197	-1.5206	0.9468
260296f	$-0.4893x^2 + 9.8178x + 5.1205$	-0.4893	9.8178	5.1205	0.9659
Average		*-0.4673*	*9.6901*	*3.4508*	*0.9102*
STDDEV		*0.0956*	*2.0324*	*8.573*	*0.1032*
261067	$-0.5724x^2 + 11.102x + 1.4391$	-0.5724	11.102	1.4391	0.9530
261126	$-0.4935x^2 + 9.4024x + 8.2454$	-0.4935	9.4024	8.2454	0.9397
261127	$-0.6x^2 + 11.649x - 1.8327$	-0.6	11.649	-1.8327	0.9633
261133	$-0.422x^2 + 8.3545x + 11.794$	-0.422	8.3545	11.794	0.8564
Average		*-0.5*	*10.127*	*4.9116*	*0.9281*
STDDEV		*0.08*	*1.5203*	*6.219*	*0.049*

However, examination of Table 11.5 did not allow any conclusions to be developed using the mathematical fit models. The average correlation factor between good and bad crystals differed by only (0.9281-0.9102 = 0.0179), that alone was not enough to support any conclusions. Following this, using the data obtained for each crystal and presented in Appendix F, the averages of the M^2 values for good and bad crystals were calculated and plotted, Fig. 11.6, to assist in visualizing any possible patterns of the beam focusability factor. In addition to average values of the beam focusability factor, Table 11.6, also shows the corresponding standard deviations used to determine the 68% confidence interval. It can be seen that after approximately 13.2 kW there are two prevalent regions that are occupied by the good and bad crystals. The beam focusabilty factor is on average smaller for good crystals and larger for bad crystals. Also taking into account the standard deviation for the measurements and establishing a

68% confidence interval as shown in Fig. 11.6, the beam focusability factor shows promise as a characterization value for crystals. Based on the average M^2 value for all crystals measured, a straight line was generated with an equation of $y = -5.5925x+125.19$ with an R^2 value of 0.9953, shown in Fig. 11.6 as the linear.

Table 11.6. Average values for beam focusability factor.

Input power (kW)	Good crystals		Bad crystals	
	Average	Standard deviation	Average	Standard deviation
6.5	49.15	0.4509	46.03	1.96
7.5	52.6	1.41	50.65	2.368
8.5	52.65	2.296	53.35	1.139
9.5	51.03	1.441	52.18	5.389
10.5	55.05	1.546	54.2	1.92
11.5	49.4	1.93	52.08	3.58
12.5	53.4	0.496	49.4	1.87
13.5	49.13	2.629	50.33	2.379
14.5	41.23	3.217	47.33	2.079
15.5	35.48	1.839	41.9	1.954
16.5	28.1	2.971	35.7	1.568
17.5	27.5	3.39	28.4	2.93
Average		1.96		2.43

Table 11.7. Average beam focusability factor for all crystals.

Input power (kW)	Average values good	Average values bad	Midpoint average
12.5	53.40	49.40	51.40
13.5	49.13	50.33	49.73
14.5	41.23	47.33	44.28
15.5	35.48	41.90	38.69
16.5	28.10	35.70	31.90
17.5	27.50	28.40	27.95

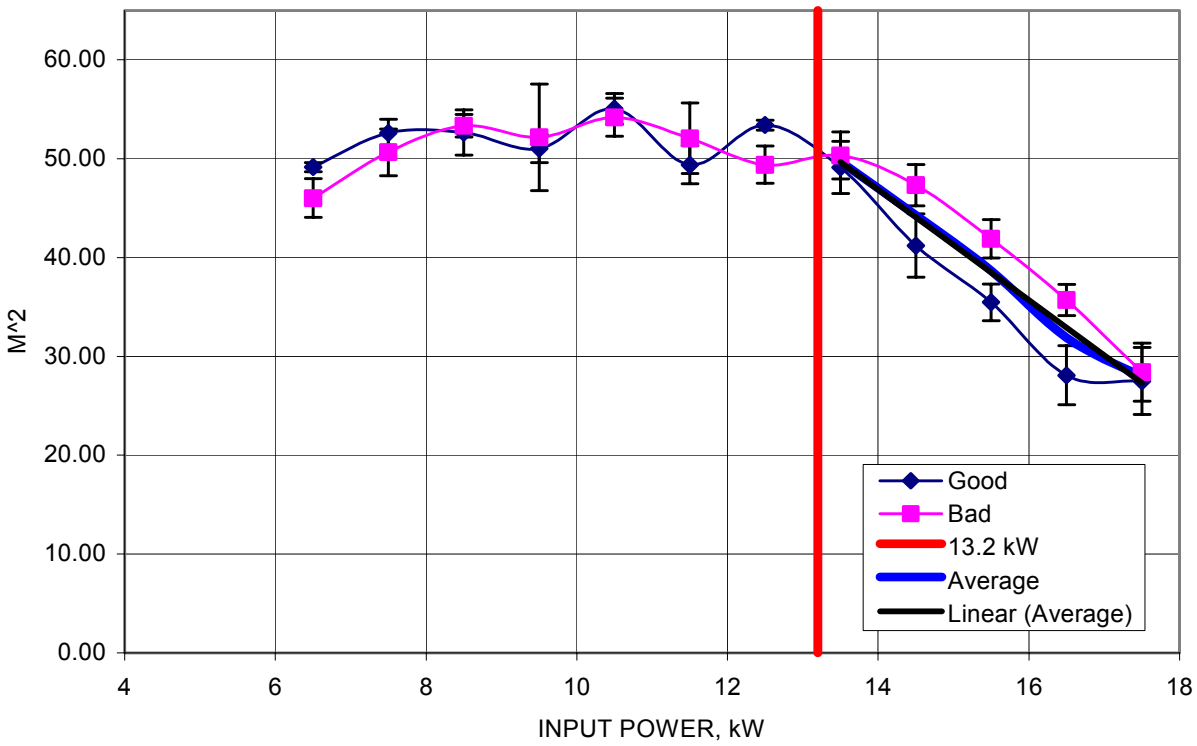

Fig. 11.6. Average beam focusability factor.

11.3.1. Measurement of the beam size

After observing the trend of the beam focusability factors to separate into two regions within the operating range of the laser, it was inferred that the beam sizes should also follow this same pattern. The beam sizes shown in Fig. 11.7 allow for the preliminary establishment of regions that can be classified as acceptable and not acceptable.

The identical approach to determine average values for both good and faulty crystals was taken as for previous measured values. Using the data obtained for all crystals shown in Appendix F, the 68% confidence interval was obtained and plotted along with the average values for both good and bad crystals, shown in Fig. 11.8.

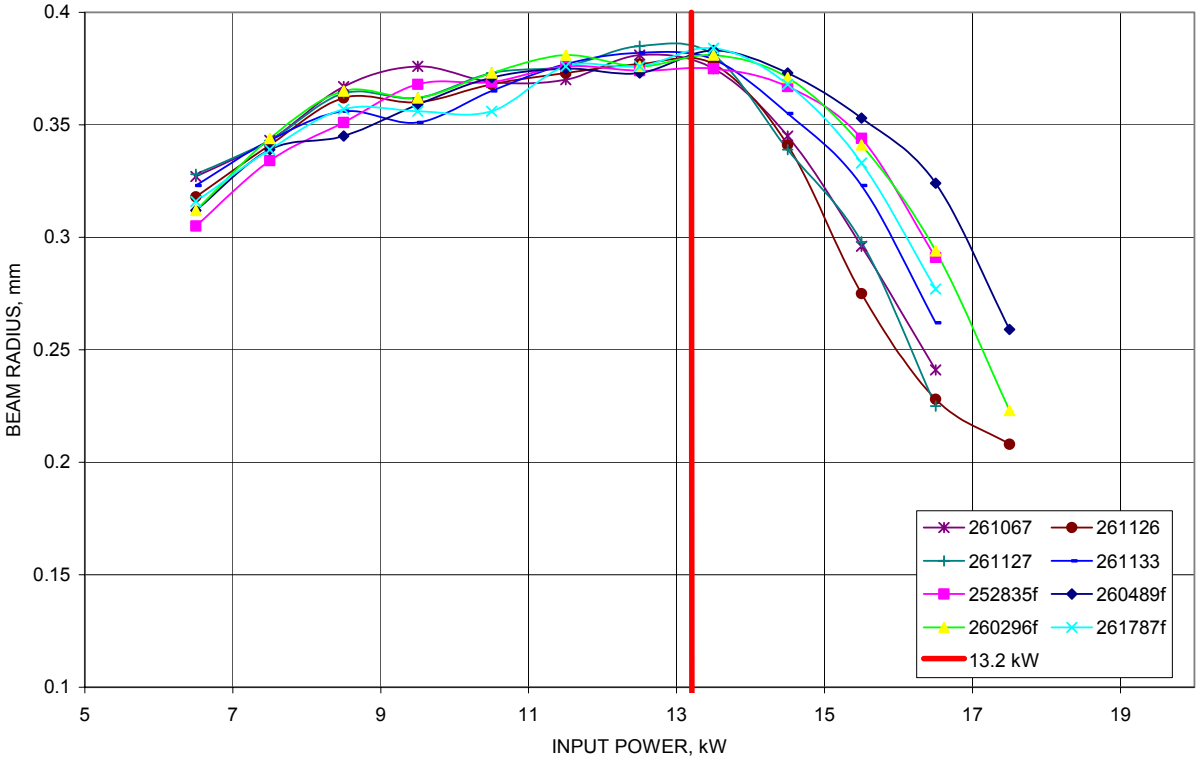

Fig. 11.7. Beam waist radius.

The average data are summarized in Table 11.8, the confidence interval is based on the standard deviations for each measured power level. The average standard deviations were 0.0071 mm and 0.0072 mm for good and bad crystals, respectively. It is clear to see that the beam size closely resembles the pattern set by the beam focusability factor. Likewise, there exists a definite difference between the acceptable and faulty crystals. In addition, the degree of separation between the two regions only allows the 68% confidence interval to include both regions in a few areas, most of which are located within the confocal region. This pattern is much more defined then the previous parameters. In order to define the point of separation between the two regions, the

average value for all crystals measured was determined, the data is summarized in Table 11.8, and is included as the linear(average) in Fig. 11.8. From this data, a straight line was drawn with an equation of $y = -0.0394x+0.9209$, and a correlation factor of R^2 equal to 0.982.

Table 11.8. Average values for beam radius.

Input power (kW)	Good crystals		Bad crystals	
	Average (mm)	Std dev (mm)	Average (mm)	Std dev (mm)
6.5	0.324	0.0045	0.311	0.0045
7.5	0.343	0.001	0.339	0.0041
8.5	0.362	0.0046	0.355	0.0085
9.5	0.362	0.01	0.361	0.0051
10.5	0.369	0.0033	0.368	0.0077
11.5	0.374	0.0032	0.377	0.0027
12.5	0.381	0.0033	0.375	0.0015
13.5	0.378	0.0026	0.381	0.0040
14.5	0.345	0.0071	0.369	0.0028
15.5	0.298	0.0196	0.343	0.0083
16.5	0.239	0.0168	0.297	0.0197
17.5	0.215	0.0092	0.24	0.0180
Average		0.0071		0.0072

Table 11.9. Average beam radius for all crystals measured.

Input power (kw)	Average Values Good	Average Values Bad	Midpoint avg
12.5	0.381	0.375	0.378
13.5	0.378	0.381	0.379
14.5	0.345	0.370	0.357
15.5	0.298	0.343	0.320
16.5	0.239	0.297	0.268
17.5	0.215	0.240	0.227

The same statistical approach was applied to model the behavior of the beam waist as was used for the beam focusability factor. Quadratic curve fitting was performed with the results shown in Table 11.10, where R^2 is the correlation factor. From the statistical analysis performed, it can be seen that the average correlation factors for the good and bad crystals differ by (0.919-0.991 = 0.038). This difference however is also not enough to develop a mathematically supported conclusion regarding the viability of using this test as a quality control method for new crystals.

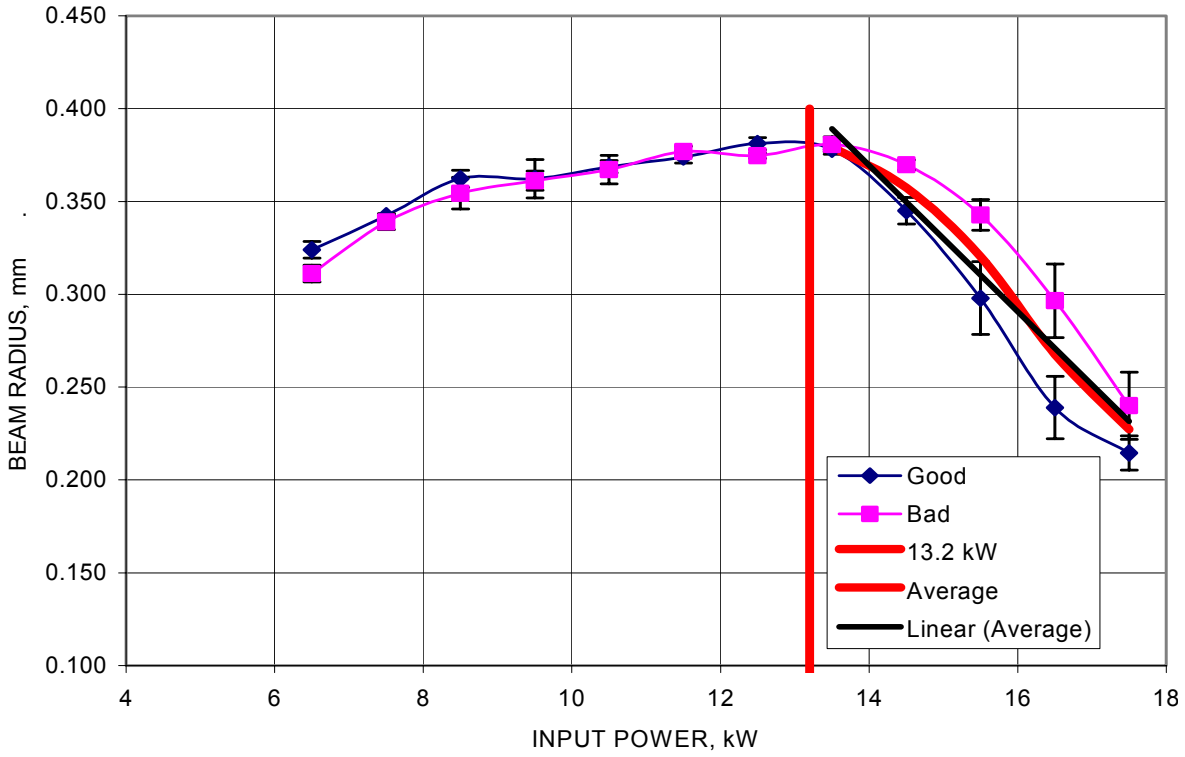

Fig. 11.8. Average beam size.

Table 11.10. Quadratic equations fit to beam size.

Crystal #	Quadratic fit equation (Ax^2+Bx+C)	A	B	C	R^2
261787f	$-0.003x^2 + 0.0683x - 0.0081$	-0.003	0.0683	-0.0081	0.8037
252835f	$-0.003x^2 + 0.0704x - 0.0261$	-0.003	0.0704	-0.0261	0.923
260489f	$-0.003x^2 + 0.0689x - 0.0191$	-0.003	0.0689	-0.0191	0.8841
260296f	$-0.0037x^2 + 0.083x - 0.0784$	-0.0037	0.083	-0.0784	0.9147
Average		*-0.0035*	*0.073*	*-0.0329*	*0.881*
STDDEV		*0.0004*	*0.007*	*0.0312*	*0.054*
261067	$-0.0039x^2 + 0.0827x - 0.0572$	-0.0039	0.0827	-0.0572	0.9209
261126	$-0.004x^2 + 0.0856x - 0.0781$	-0.004	0.0856	-0.0781	0.9402
261127	$-0.0042x^2 + 0.09x - 0.0949$	-0.0042	0.09	-0.0949	0.8939
261133	$-0.003x^2 + 0.0704x - 0.0261$	-0.003	0.0704	-0.0261	0.923
Average		*-0.004*	*0.088*	*-0.0641*	*0.919*
STDDEV		*0.0005*	*0.008*	*0.0296*	*0.019*

11.4. Discussion

After reviewing all parameters calculated and measured as part of this thesis, it was determined that the M^2 value, along with the beam size, provide the most promising methods for the characterization of laser crystals. The beam focusability factor allows for the quantitative measurement of the laser crystal behavior following standards established by the International Standards Organization. Thus, the M^2 value has already been established as the method by which lasers are judged. However, further testing of laser crystals would be required prior to the establishment of any reference M^2 values for these crystals. The measurement of the M^2 factor also allows for a complete picture of what happens within the resonator, as it is an inherent parameter of the beam source.

Crystals previously classified as faulty (i.e., bad), showed beam diameters that remained large and decreased at a slower rate as input power increased. Also, one crystal, 261133, occupies a region between the "good" and "bad" areas. This crystal was marked for further determination of possible problems during the final test phases. During these tests, the laser with this crystal installed experienced some problems while coupling the beam into the fiber. Although the problems were resolved without replacing any crystals, the source of those problems may be attributed to this crystal. However, no conclusive data are available to support this claim, at his time.

It should also be pointed out that the pattern established by the focal length coincides with the observed behavior of the beam focusability factor and beam size. Crystals with a shorter focal length have, on average, smaller beam sizes and M^2 values.

This is due to the additional focusing power of the crystal. Further investigation into this relationship should not be overlooked, as a more pronounced relationship may be present.

11.5. Additional factors to be considered

The criteria defining acceptable and faulty (i.e., bad) crystals are very broadly defined. Therefore, it is difficult to develop a single test or use a single parameter that will be able to filter out bad crystals from the production line. Currently, there are two criteria used to define "good" crystals, first, the crystal must produce above 700 W and, second, the shape of the beam must be circular with no aberrations. When initially tested, the crystal is located alone in a single cavity laser. However, when placed in a large multi-cavity laser, the behavior of the crystal may be affected. The effects may also vary dependent on whether the crystal is used as a part of the resonator or amplifier chains. The mechanical mounting methods used to secure the crystal within a cavity are also very influential on the behavior of the laser beam as it propagates through the cavity.

The fabrication techniques used to grow the Nd:YAG crystal remain a "black art." Thus, it is very difficult to determine which crystal growth variables have significant effects on the crystal sensitivity or the beam focusability factors.

12. CONCLUSIONS AND RECOMMENDATIONS

This thesis has been presented as a preliminary study of characterization methods suitable for Nd:YAG crystals. An emphasis has been placed on the optimization of the selection process for crystals that will be installed in multi-cavity Nd:YAG lasers. Laser manufacturers are striving to shorten the production time for the laser and to make its final assembly more predictable. An important area that has caused many production problems has been the crystals that are used in the lasers. It is possible that a crystal will pass all current quality control criteria, but still demonstrate undesirable behavior when installed in a multi-cavity laser device. This thesis was conducted in order to evaluate different characterization parameters of crystals that could be employed to segregate good from bad crystals.

In the experiments conducted, three parameters were tested to evaluate which would be able to distinguish between good and bad crystals. The results show that no single parameter is able to completely characterize the behavior of the Nd:YAG crystals. However, distinct patterns were observed in the beam focusability factor and beam size. Statistical methods have shown that these parameters are distinct at several locations. These findings establish regions for good and bad crystals and may be used to judge crystals before they are installed in a laser device. The beam focusability factor and the beam waist size show the most prevalent patterns, having an average separation between the average values for each power level of 3.5 and 0.025 m, respectively. Taking into account the 68% confidence interval it can be seen that these parameters show the most distinguishable trends. The focal length of the crystals, while not directly usable to

classify good and bad crystals due to a lower average separation between the regions of 0.008 m, may explain the differences in the beam focusability factor and the beam size. Due to the lower focusing power of bad crystals, a larger beam waist is produced resulting in a larger M^2 value. This agrees well with the experimental data obtained.

Both the focal length and crystal sensitivity factor are based on extensive approximations of Nd:YAG crystal behavior. A more accurate method that will model the behavior of the thermal lens of the crystal, and also a procedure to accurately determine the focal length of the crystal, should be established if these parameters are to be further explored. The crystal sensitivity factor did not have any published results for comparison. Only Koechner (1999) mentions this factor, and it is in the context of a material property. In the experiments conducted as part of this thesis, the crystal sensitivity factor was determined as a function of input power. However, its value quantifying the quality of a laser crystal must be further evaluated. The current results only show strong variations within the confocal region of the resonator, the remaining regions show stable crystal sensitivity values.

However, in order to be able to completely determine the behavior of a crystal, the effects of each variable during the crystal growth process that influence the generated laser beam must be determined. Once this is complete, it may be possible to relate the three parameters, i.e., the crystal sensitivity factor, the beam focusability factor, and the beam waist size, evaluated as part of this thesis to each variable.

The measurements that may serve to distinguish between acceptable and faulty crystals were found to be the beam focusability factor and the beam size. Both of these

parameters can be directly measured using standardized methods. Thus in the opinion of the author and based on the data obtained as part of this thesis, the beam focusability factor and the beam size are currently the only values that should be utilized for quality control measures of laser crystals. However, to increase validity of the methodology developed in this thesis, more experimental work should be performed in the future to independently confirm results presented in this volume.

13. REFERENCES

Bellis, M., 2002, "Laser History,"
http://inventors.about.com/library/inventors/bllaser.htm

Bronski, M.T., Machate, M.S., Furlong, C., and Pryputniewicz, R.J., 2002, "Power and thermal management of a lamp pumped Nd:YAG laser cavity," *Proc. IMAPS 29th Annual Symposium.*, Boxborough, MA, pp. 101-106.

Bronski, M.T., and Machate, M.S., 2002, "Nd:YAG lasers thermal effects and optimization," *Proc. SEM Graduate Students Symposium.*, SUNY Stony Brook, Long Island, NY.

Clarkson, W. A., and Hanna, D. C., 1998, "Resonator design consideration for efficient operation of solid-state lasers end-pumped by high power diode bars," *Optical Resonators-Science and Engineering*, Kluwer Academic Publishers, Dordrecht, Netherlands.

CORD, 2002, "Laser Electro/Optics Technology series,"
http://cord.org/cm/leot/course03_mod03/mod03_03.htm , Center for Occupation Research and Development, Waco, Texas.

Dascalu, T., Pavel, N., and Poterasu, M., 1998, "Optimized resonators for high energy long-pulse Nd:YAG laser," *Optical Resonators-Science and Engineering*, Kluwer Academic Publishers, Dordrecht, Netherlands.

DIN, 1999, "Pruefverfahren fuer Laserstrahlparameter," Deutsches Institut fuer Normung e.V., DIN EN ISO 11146, 1999, Berlin.

Forward, R., 1979, "Einstein's Legacy,",
http://home.achilles.net/~jtalbot/history/einstein.html

HAAS, 1994, "Nd:YAG laser Grundlagen," HAAS Laser, Schramberg, Germany.

Hecht, J., 1992, *The laser guidebook*, McGraw-Hill, New York.

Hecht, J., 1994, *Understanding Lasers: An entry level guide*, IEEE Press, New York, NY.

Ifflaender, R., 2001, *Solid-state lasers for materials processing*, Springer-Verlag, Berlin.

Kaivola, M., 2002, "Resonators,"
http://omm.hut.fi/optics/laserfysiikka/2002/resonator.pdf, Helsinki University of Technology, Helsinki, Finland.

Kincade, K., and Anderson, S., 2002,"Review and forecast of the laser markets Part I: Nondiode lasers," *Laser Focus World*, Penn-Well Corp. Nashua, NH.

Koechner, W., 1999, *Solid-state laser engineering*, Springer-Verlag, Berlin.

Kumkar, Dr. M., 2002, personal correspondence, TRUMPF Laser GmbH + Co. KG, Schramberg, Germany.

Lucent, 1998, "The invention of the laser at Bell Laboratories: 1958-1998," http://www.bell-labs.com/history/laser/contrib.html , Lucent Technologies Inc., Murray Hill, NJ.

Mathsoft, 2001, Mathcad Professional 2001, Mathsoft, Inc., Cambridge, MA.

Mudge, D., Ostermeyer, M., Veitch, P. J., Much, J., Middlemiss, B., Ottaway, D. J., and Hamilton, M.W., 2000, "Power scalable TEM_{00} CW Nd:YAG laser with thermal lens compensation," *IEEE Journal of selected topics in quantum electronics*, 6:643-649

Newport, 2002b, "Gaussian beam optics tutorial," www.newport.com/Support/Tutorials/Optics/02.asp , Newport Corp., Irvine, CA.

PRIMES, 2002, www.primes.de, PRIMES Lasermesstechnik GmbH, Pfungstadt, Germany.

Roundy, C., 1994, "M^2, what is it and why do I care?" Spiricon Inc., Utah.

Schlueter, Dr. H., and Markille, Dr. G., 2002, personal correspondence, TRUMPF Inc., Farmington, CT.

Siegman, A. E., 1986, *Lasers*, University Science Books, Sausalito, CA.

Spiricon, 2002, www.spiricon.com Spiricon Inc., Logan, Utah.

Steen, W. M., 1998, *Laser materials processing*, Springer-Verlag, Berlin.

Svelto, O., 1998, *Principles of lasers*, Plenum Press, New York.

Talbot, J., 2002, "Optical Laser," http://home.achilles.net/~jtalbot/history/ruby.html

TRUMPF, 2002, www.us.trumpf.com TRUMPF Inc., Farmington, CT.

VLOC, 2002, "VLOC YAG manufacturing process," VLOC Inc., Port Richey, FL.

APPENDIX A. Nd:YAG BEAM PROPAGATION

Using the simple thin lens model of the YAG rod that is positioned equidistant from each mirror in the resonator, the beam size at various locations will be evaluated. The equations below will be used to calculate the beam waist at the outcoupler mirrors assuming a known focal length of the rod. The focal length of the rod was taken from data published in Koechner (1999). Procedures for propagating the complex beam parameter through optical systems are developed in detail by Ifflaender (2001) and Siegman (1986). Upon exiting from the resonator, the program will advance the beam along the propagation axis to the beam analyzer.

Known parameters of the laser system are summarized in Table A.1.

Table A.1. Known parameters for laser beam.

Wavelength of YAG laser beam	$\lambda_{YAG} := 1.064\,10^{-6}$	m
Theoretical smallest value for M^2	$M_{squared} := 4.3$	

A laser beam with an M^2 value greater than one, will behave similar to a laser beam with a larger wavelength. This wavelength can be determined by multiplying the nominal value of the laser wavelength by the smallest theoretically obtainable M^2 value (TRUMPF, 2002). This is shown by

$$\lambda := \lambda_{YAG} M_{squared} \quad . \tag{A.1}$$

The resultant wavelength is then

$$\lambda = 4.575 \times 10^{-6} \text{ m} \quad .$$

The physical dimensions of the resonator are defined in Table A.2. The values were obtained by measuring the resonator frame and locations of AR and HR mirrors of the HL506D laser used in the experiments.

Table A.2. Definitions of laser system variables.

Distance front mirror to center of rod	d1 := 0.240	m
Distance from center of first rod to rear mirror	d2 := 0.240	m
Distance from rear mirror to beam expander	d3 := 0.260	m
Distance from beam expander to beam analyzer	d4 := 0.4	m
Focal length of rod (assumed from published values in Koechner, (1999) based on the average focal length of the two polarizations of light)	FL := 0.30	m
Focal length of beam collimating lens	f := 0.260	m

Dimensions summarized in Table A.2 can be related to Fig. A.1.

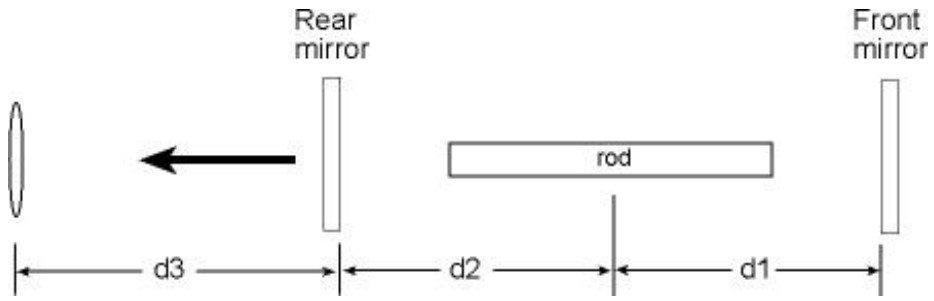

Fig. A.1. Beam propagation path.

Following the principles for defining a stable resonator as outlined in Siegman (1986), we generate the ABCD matrix for a round trip through the resonator. Referring to Fig A.2, the individual matrices can be written as

$$M1 := \begin{pmatrix} 1 & d1 \\ 0 & 1 \end{pmatrix} \quad M2 := \begin{pmatrix} 1 & 0 \\ \frac{-1}{FL} & 1 \end{pmatrix} \quad M3 := \begin{pmatrix} 1 & d2 \\ 0 & 1 \end{pmatrix} \quad M4 := \begin{pmatrix} 1 & d3 \\ 0 & 1 \end{pmatrix} \quad M5 := \begin{pmatrix} 1 & d4 \\ 0 & 1 \end{pmatrix} .$$

Matrices for return trip can be written as

$$M11 := M1 \qquad M22 := M2 \qquad M33 := M3 \ .$$

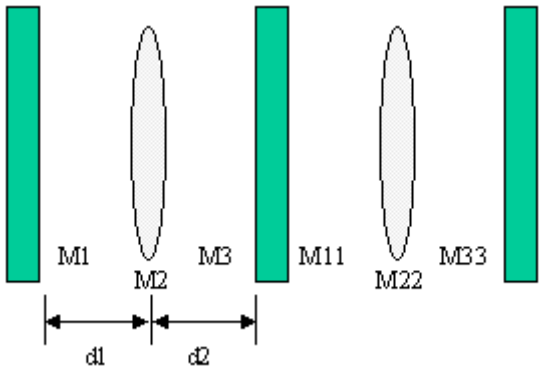

Fig. A.2. Equivalent lens diagram for a round-trip through the resonator.

The equivalent round-trip matrix through the resonator is simply the product of all of the ABCD matrices representing the system (Siegman, 1986). Therefore, the ABCD matrix for a round-trip through resonator becomes

$$RT := M33 \cdot M22 \cdot M11 \cdot M3 \cdot M2 \cdot M1 \quad . \tag{A.2}$$

Evaluation of Eq. A.2 leads to

$$RT = \begin{pmatrix} -0.92 & 0.115 \\ -1.333 & -0.92 \end{pmatrix} \quad . \tag{A.3}$$

Next, a check to determine stability of the resonator should be performed. Defining the stability criterion as

$$\left(\frac{A + B}{2} \right)^2 < 1 \quad , \tag{A.4}$$

it can be evaluated to obtain

$$\left(\frac{RT_{0,0} + RT_{1,1}}{2} \right)^2 = 0.846 \quad . \tag{A.5}$$

Based on Equations A.4 and A.5, we determine that the resonator is stable.

The *q*-value is calculated to ensure it is self-repeating by performing the following calculations. The basic definition of the *q*-value is established as

$$\text{InvQ1} := \left(\frac{\text{RT}_{1,1} - \text{RT}_{0,0}}{2 \cdot \text{RT}_{1,0}} \right) + \frac{\text{i}}{2 \cdot \text{RT}_{1,0}} \cdot \sqrt{4 - \left(\text{RT}_{0,0} + \text{RT}_{1,1} \right)^2} \quad , \tag{A.6}$$

it can be evaluated to obtain

$$\text{InvQ1} = -0.294\text{i} \quad . \tag{A.7}$$

In order to obtain the *q*-value the inverse of Eq. A.6 must be taken as

$$\text{Q1sol} := \frac{1}{\text{InvQ1}} \quad , \tag{A.8}$$

and evaluated numerically to obtain

$$\text{Q1sol} = 3.402\text{i} \quad . \tag{A.9}$$

The second *q*-value is obtained by using

$$\text{InvQ2} := \frac{\text{RT}_{1,1} - \text{RT}_{0,0}}{2 \cdot \text{RT}_{1,0}} - \frac{\text{i}}{2 \cdot \text{RT}_{1,0}} \cdot \sqrt{4 - \left(\text{RT}_{0,0} + \text{RT}_{1,1} \right)^2} \quad , \tag{A.10}$$

the inverse is taken to obtain

$$\text{Q2sol} := \frac{1}{\text{InvQ2}} \quad , \tag{A.11}$$

and evaluation results in

$$\text{Q2sol} = -3.402\text{i} \quad . \tag{A.12}$$

From Eqs A.9 and A.12 we determine the *q*-value self repeats. From the definition of a plane-parallel resonator we also know that a beam waist is formed at both mirrors (Ifflaender, 2001).

The solution obtained in Eq. A.12 can be checked by using the equivalent ABCD matrix obtained from Eq. A.2 and operating on the *q*-value as

$$\text{Qcheck} := \frac{(\text{RT})_{0,0} \cdot \text{Q2sol} + (\text{RT})_{1,0}}{(\text{RT})_{0,1} \cdot \text{Q2sol} + (\text{RT})_{1,1}} \quad , \tag{A.13}$$

and it can be evaluated to obtain

$$Qcheck = -3.402i \ . \tag{A.14}$$

Comparison of Eqs A.12 and A.14 it is seen that the results are identical.

Using the complex beam parameter *q*, the beam waist can be calculated at either mirror as

$$w_{mirror2} := \frac{\lambda_{YAG}}{\pi} \cdot \sqrt{\frac{-RT_{1,0}}{RT_{0,1}}} \ , \tag{A.15}$$

and by evaluation the beam size of

$$w_{mirror2} = 1.152 \times 10^{-6} \ m \ , \tag{A.16}$$

is obtained.

Now knowing the *q*-value at one reference plane (mirror), it can be propagated through various optical elements to a desired point. ABCD matrices are defined for each component that the beam propagates through. The location and nomenclature of the matrices and dimensions is shown in Fig. A.3.

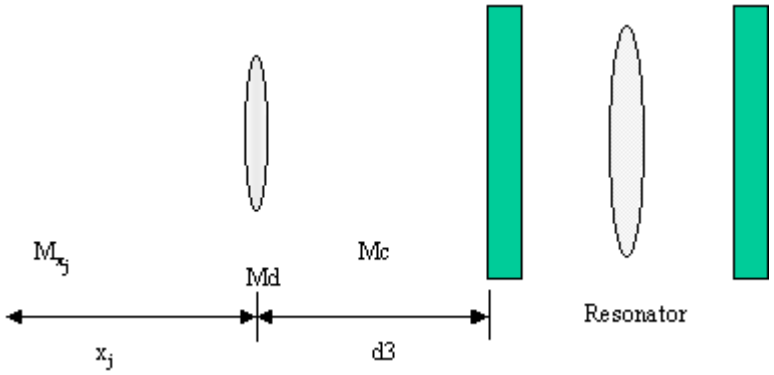

Fig. A.3. Beam propagation path outside of resonator.

The equivalent ABCD matrices for each component are defined in Table A.3.

Table A.3. Definitions of optical system variables.

Distance from AR-mirror to 1st lens	$M_c := \begin{pmatrix} 1 & d3 \\ 0 & 1 \end{pmatrix}$
ABCD for 1st lens	$M_d := \begin{pmatrix} 1 & 0 \\ \frac{-1}{f} & 1 \end{pmatrix}$
ABCD matrix to propagate beam after 1st lens	$M_{e_j} := \begin{pmatrix} 1 & x_j \\ 0 & 1 \end{pmatrix}$

A vector is defined to propagate the beam away from the lens along a straight line. The number of elements in the vector is specified as

$$j := 1..41 \quad , \tag{A.17}$$

and the vector is defined by

$$x_j := \frac{d3 \cdot (j - 1)}{10} \quad . \tag{A.18}$$

The ABCD matrices are multiplied to obtain an equivalent matrix representing the system through which the *q*-value can be propagated. The equivalent matrix is defined to be

$$M_{test_j} := M_{e_j} \cdot M_d \cdot M_c \quad . \tag{A.19}$$

Using the complex beam parameter determined in Eq. A.12, it is propagated through the system using the equivalent matrix as determined in Eq. A.19. The new complex beam parameter is determined as

$$qtest_j := \frac{\left(M_{test_j}\right)_{0,1} + Q2sol \cdot \left(M_{test_j}\right)_{0,0}}{\left(M_{test_j}\right)_{1,1} + Q2sol \cdot \left(M_{test_j}\right)_{1,0}} \quad . \tag{A.20}$$

With the new *q*-value at varying points throughout the propagation path, it is possible to determine the beam waist size as

$$\omega 1_j := \sqrt{\frac{-\lambda_{YAG}}{\pi \cdot \left(\mathrm{Im}\left(\frac{1}{qtest_j} \right) \right)}} \quad . \tag{A.21}$$

The results of Eq. A.21 are shown in Fig. A.4.

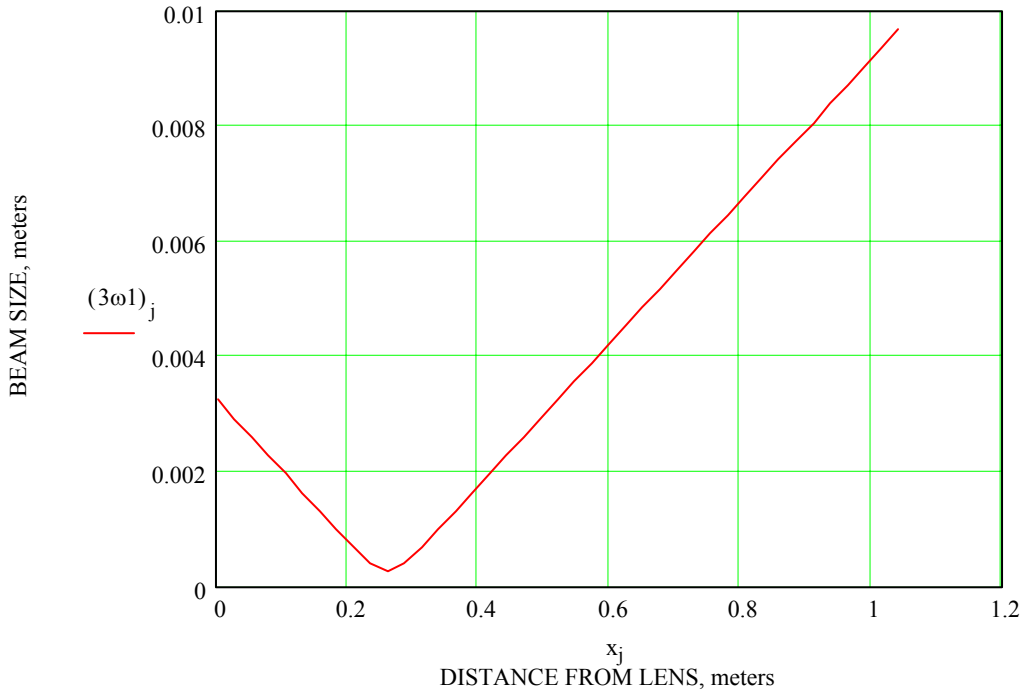

Fig. A.4. Beam size as a function of increasing distance from the focusing lens.

APPENDIX B. CHARACTERISTIC POWER CURVE OF A CRYSTAL

TRUMPF	**Characteristic curve of rod**	date: 22.11.2002 Page: 1

CRYSTAL ID: 260296-test

Manufacturer laser rod	Litton
Equipment number	E0251A0110
Reflector number upper part/ lower part	/
Examiner	M. Bronski
start value / final value / step width [W]	5 / 500 / 3
time interval [ms]	2000
Laser power control (1 = ON)	0
control reserve (1=active)	0
Maximum power	774 W @ 18.13 kW
Durchfluß Kavität Min / Max [l/h]	1420 / 1430
Tanktemperatur Min / Max [°C]	23.3 / 30.2
Maximum TKS links	50.0 °C @ 19.32 kW @ 719 W
Maximum TKS rechts	50.0 °C @ 19.21 kW @ 722 W

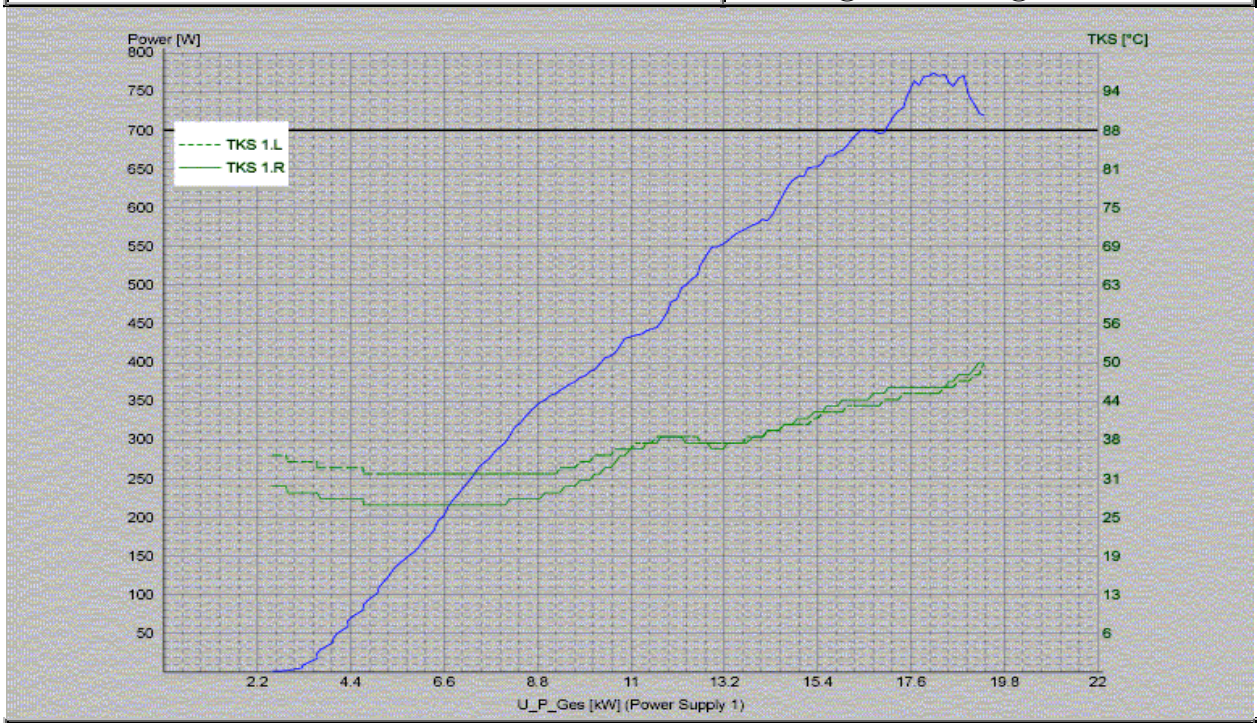

Check for minimum power required : found correct!

APPENDIX C. MATHEMATICAL DETERMINATION OF THE THERMAL LENS EFFECT

The theoretical value of the crystal sensitivity factor is determined using the equations shown below. The calculations follow procedures and equations as outlined by Koechner (1999) and Ifflaender (2001). Experimental data were obtained from a HL506D laser device on which the experiments were conducted. The data used were obtained during a power measurement program run on the laser. The calculations show the temperature dependent variation in the focal point location. All results were calculated using Mathcad software (Mathsoft, 2001).

The nomenclature and variables used are summarized in Table C.1.

Table C.1. Definition of variables.

Wavelength of YAG light	$\lambda := 1.06 \cdot 10^{-4}$	cm
Index of refraction	$n_0 := 1.82$	
Thermal refractive index change	$dn\_dT := 7.3 \cdot 10^{-6}$	$\frac{1}{C}$
Thermal expansion coefficient	$\alpha := 8.2 \cdot 10^{-6}$	$\frac{1}{C}$
Heat transfer coefficient	$h := 1.25$	$\frac{W}{cm^2 \cdot C}$
Thermal conductivity	$k := 0.13$	$\frac{W}{cm \cdot K}$
Outer radius of crystal	$r_0 := \frac{.635}{2}$	cm
Length of crystal	$L := 17.7$	cm
Cross sectional area of the crystal	$A := \pi \cdot r_0^2$	cm^2
Radius as a range variable	$r := 0, 0.001921 .. 0.317$	cm

The measured crystal temperature is then imported from a database produced by the laser control (WinLAS) during a power cycling program. Due to the large number of data points (86) the list is suppressed to conserve space. Also, the input and output powers of the laser are imported.

Temperature of the rod left side measured in ºC

$T_L :=$

	0
0	34
1	34

Temperature of the rod right side measured in ºC

$T_R :=$

	0
0	29
1	29

Input power measured in kW

$P_{in} :=$

	0
0	2.55
1	2.72

Output power measured in W

$P_{out} :=$

	0
0	2.2
1	2.2

Taking the average of the two temperature readings obtained from the surface of the crystal, we obtain the average temperature of the crystal. Mean outer crystal temperature is defined as

$$T_{outer} := \frac{T_L + T_R}{2} \qquad T(r_0) := T_{outer} \quad . \tag{C.1}$$

The coolant temperature is read from the laser control, and represents the temperature of the water in the internal storage tank. Water from the tank is used in the closed loop cooling system to cool the various laser components. This temperature can vary during the course of a power measurement cycle, however, no provision is provided in WinLAS to actively measure the tank temperature in conjunction with the other measurements. For the purposes of this analysis, it can be assumed that the temperature remains constant. Mean coolant temperature is assumed to remain constant at

$$T_F := 23 \ C \quad . \tag{C.2}$$

Using equations obtained from Koechner (1999) the heat absorption in the crystal along with the temperature distribution can be calculated using the power dissipated by the crystal defined as

$$P_a := 2\pi \cdot r_0 \cdot L \cdot h \cdot \left(T(r_0) - T_F\right) \quad . \tag{C.3}$$

From Eq. C.3, the heat generated per unit volume is obtained using

$$Q := \frac{P_a}{\pi \cdot r_0^{\,2} \cdot L} \quad . \tag{C.4}$$

Following this, the temperature at center of crystal is

$$T_c := T_F + P_a \cdot \left(\frac{1}{4\pi \cdot k \cdot L} + \frac{1}{2\pi \cdot r_0 \cdot L \cdot h} \right) , \tag{C.5}$$

and the radial temperature distribution can be expressed as

$$T(r) := \left[T(r_0) + \left(\frac{Q}{4 \cdot k} \right) \cdot \left(r_0^{\,2} - r^2 \right) \right] . \tag{C.6}$$

Using data obtained from the HL506D laser, the variation of the mean outer crystal temperature with increasing input power in shown in Fig. C.1.

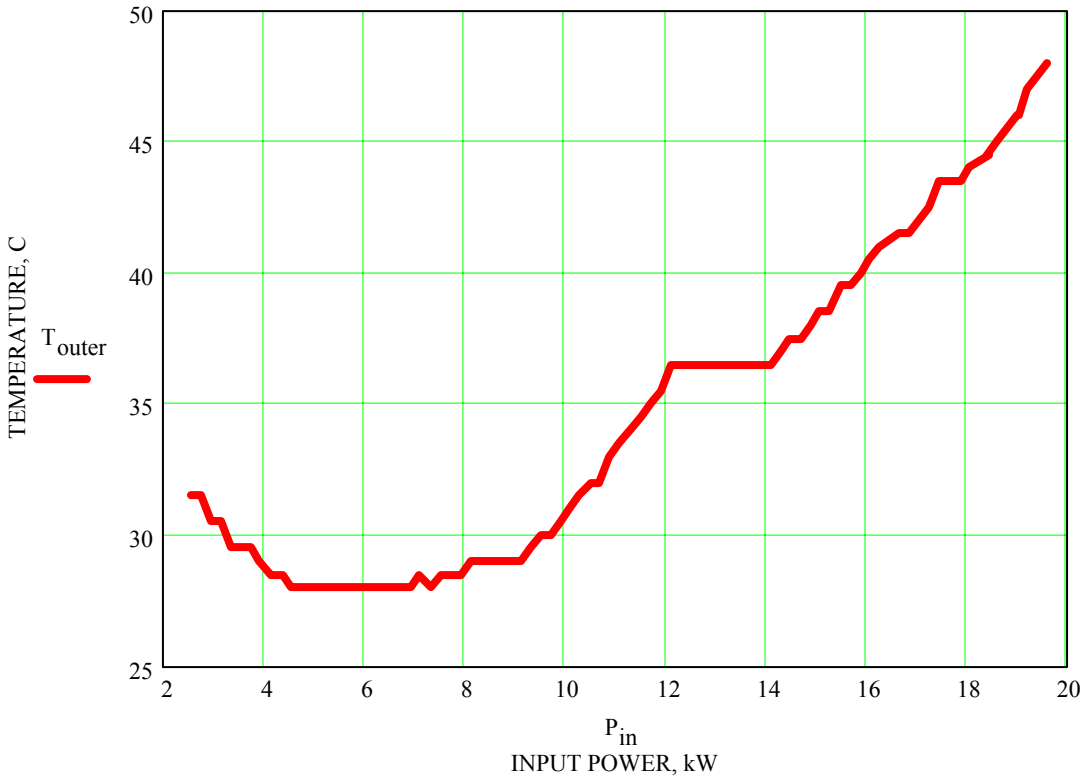

Fig. C.1. Crystal surface temperature plotted against input power.

In order to define the variation in the focal position for the two different polarizations of light, the polarization dependent photoelastic coefficients for Nd:YAG are first defined as

$$C_r := 0.017 \quad , \tag{C.7}$$

for radially polarized light, and for tangentially polarized light as

$$C_\phi := -0.0025 \quad . \tag{C.8}$$

Combining the effects of the stress and temperature dependent variation of the refractive index, and the distortion of the end faces, the expressions defined by Koechner (1999) for each polarization of light are used. The focal length for radially polarized light is expressed as

$$f_r := k \cdot \frac{A}{P_a} \cdot \left[\frac{1}{2} \cdot dn\_dT + \alpha \cdot C_r \cdot n_0^{\,3} + \frac{\alpha \cdot r_0 \cdot (n_0 - 1)}{L} \right]^{-1} \quad , \tag{C.9}$$

and the focal length for tangentially polarized light is determined by

$$f_\phi := k \cdot \frac{A}{P_a} \cdot \left[\frac{1}{2} \cdot dn\_dT + \alpha \cdot C_\phi \cdot n_0^{\,3} + \frac{\alpha \cdot r_0 \cdot (n_0 - 1)}{L} \right]^{-1} \quad . \tag{C.10}$$

The temperature dependent variation of the refractive index constitutes the major contribution of the thermal lensing, of about 20%. Effects of the end-face curvature variation account for only 6% (Koechner, 1999).

The analytically determined focal length of the crystal is shown in Fig. C.2.

The crystal sensitivity factor defines the change of focusing power of the crystal in response to a change in the input power. The laser crystal sensitivity is defined as

$$\frac{d\left(\frac{1}{f}\right)}{dP_{in}} = M^{-1} \quad . \tag{C.11}$$

In Eq. C.11, the term "M" contains all the material parameters and an efficiency factor η that relates the input power to the power dissipated as heat, and other losses.

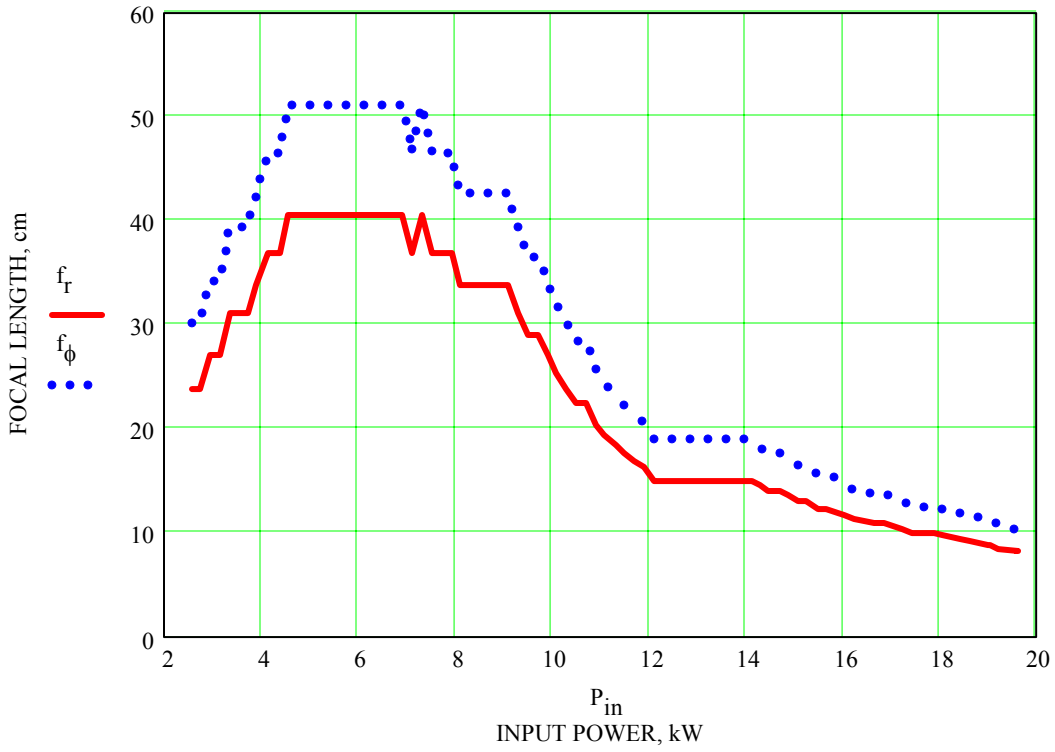

Fig. C.2. Focal length for radially and tangentially polarized light.

The change in the focal position of the crystal is first determined by calculating the individual focus locations based on the input power and the polarization of the light. This is accomplished by using Eqs C.9 and C.10. Taking the inverse of the calculated focal position, the focal power of the rod is obtained for a particular polarization.

An index must be defined in order to be able to properly calculate the variation in focal location between each measuring point. The variable *j* represents the total number of measurements used, and *i* is used as a range variable. Both variables are defined as

$$j := 86 \quad , \qquad i := 1 \,..\, j \; . \tag{C.12}$$

The focal length variations based on the input power are shown below, values are calculated for both states of polarization. The focal power of the crystal is defined as the inverse of its focal length, shown by

$$F := f_r^{-1} \; . \tag{C.13}$$

The change in the focal power for radially polarized light between each measuring point is defined as

$$Frd_i := F_i - F_{i-1} \quad . \tag{C.14}$$

Focal length variation for tangentially polarized light is defined by first taking the inverse of the focal length as

$$F\phi := f_\phi^{-1} \quad , \tag{C.15}$$

and the focal power variation between measuring points is given by

$$F\phi d_i := F\phi_i - F\phi_{i-1} \quad . \tag{C.16}$$

The results of the calculations performed in Eqs C.14 and C.16 are shown in Eqs C.17 and C.18 respectively

$Frd =$

	0
0	0
1	0
2	$-4.943 \cdot 10^{-3}$

(C.17)

$F\phi d =$

	0
0	0
1	0
2	$-3.91 \cdot 10^{-3}$

(C.18)

The incremental difference in input power between two consecutive measuring points is determined as

$$Pindiff_i := Pind_i - Pind_{i-1} \quad . \tag{C.19}$$

Defining the crystal sensitivity parameter as

$$M := \overrightarrow{\left(\frac{Frd}{1000 \, Pindiff} \right)} \quad , \tag{C.20}$$

and the input power to the laser is defined as a vector to facilitate plotting as

$$P := \overrightarrow{P_{in}} \quad . \tag{C.21}$$

The crystal sensitivity factor is shown in Fig. C.3. Koechner (1999) specifies it as a material property with a value ranging from 0.5-1.0*10^{-3} diopters/W. From Fig. .3 and comparing to the published values, we can infer that this rod is insensitive to pump power fluctuations. These results also do not correlate well to the experimentally determined values. This may be attributed to the approximations made in order to analytically determine the focal length.

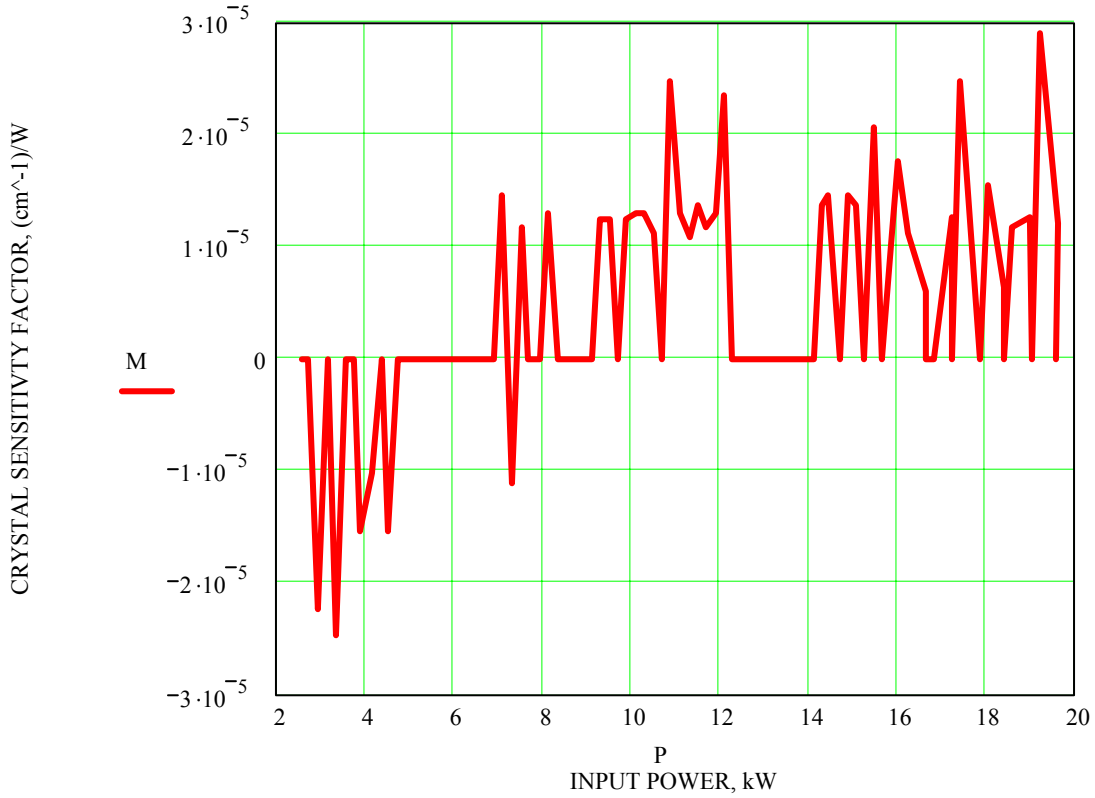

Fig. C.3. Crystal sensitivity factor plotted against input power.

APPENDIX D. RESONATOR MODEL

In order to calculate the thermal lensing effect present in the resonator, a model was developed using the stable quadratic duct approximation for the Nd:YAG crystal. The complex beam parameter values obtained at the FocusMonitor measuring plane were propagated backwards to the AR mirror, at which point the self-repeating q-value was determined. The resonator model was then solved for the appropriate characteristic focal length of the crystal that ensured a self-repeating q-value. The calculations are presented for 3 input power levels. After determining the β value the beam size within the resonator was determined.

The data used for the calculations were obtained by measurement of crystal number 261067 that passed all current quality control measures and was identified as good. The experimental setup is shown in Fig. D.1, and variable definitions are presented in Table D.1.

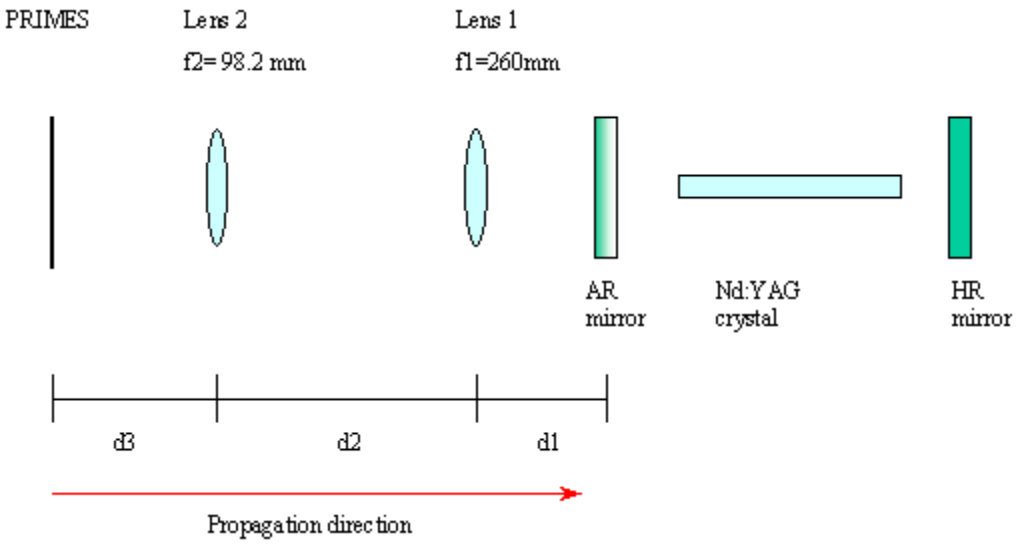

Fig. D.1. Experimental setup.

Table D.1. Definitions of laser system variables.

Distance from AR mirror to lens 1	d1 = 0.260	m
Distance from lens 1 to lens 2	d2 = 0.9445	m
Focal length of lens 1	f1 = 0.260	m
Focal length of lens 2	f2 = 0.0982	m
Length of resonator	L = 0.5	m

The wavelength of the Nd:YAG laser is

$\lambda := 1.06 \cdot 10^{-6}$ m .

The measured values at the FocusMonitor measuring plane are then defined. The beam radius is expressed in meters, and the distance, d3, from the focusing lens to the FocusMonitor is expressed in millimeters. All measured values are arranged as arrays to facilitate subsequent calculations.

The beam size, ω_P, beam focusability factor, M^2, and distance from the focusing lens to the FocusMonitor, d3, are defined as follows:

$\omega_P :=$

	0
0	0.000327
1	0.000343
2	0.000367
3	0.000376
4	0.000369
5	0.00037
6	0.000381
7	0.000375
8	0.000345
9	0.000296
10	0.000241

MSQ :=

	0
0	49.5
1	54.3
2	54
3	52.7
4	55.4
5	50
6	54.1
7	48.5
8	42.4
9	36.2
10	27.5

d3 :=

	0
0	100.83
1	100.21
2	99.63
3	98.87
4	99.03
5	98.21
6	97.45
7	96.16
8	94.76
9	93.09
10	90.93

The variable distance between the waist location determined by the FocusMonitor and lens # 2 corresponding to the different pump powers is defined in ABCD matrix format as

$$M1a := \begin{pmatrix} 1 & \frac{d3_{0,0} + 10.75}{1000} \\ 0 & 1 \end{pmatrix}, \tag{D.1}$$

$$M1b := \begin{pmatrix} 1 & \frac{d3_{6,0} + 10.5}{1000} \\ 0 & 1 \end{pmatrix}, \tag{D.2}$$

and

$$M1c := \begin{pmatrix} 1 & \frac{d3_{10,0} + 10}{1000} \\ 0 & 1 \end{pmatrix} . \tag{D.3}$$

The ABCD matrices defining the individual components, shown in Fig. .1, are defined as

$$M2 := \begin{pmatrix} 1 & 0 \\ \frac{-1}{f2} & 1 \end{pmatrix} , \tag{D.4}$$

$$M3 := \begin{pmatrix} 1 & d2 \\ 0 & 1 \end{pmatrix} , \tag{D.5}$$

$$M4 := \begin{pmatrix} 1 & 0 \\ \frac{-1}{f1} & 1 \end{pmatrix} , \tag{D.6}$$

and

$$M5 := \begin{pmatrix} 1 & d1 \\ 0 & 1 \end{pmatrix} . \tag{D.7}$$

The equivalent ABCD matrices for the optical system external to the resonator are defined using the 3 different locations for the measured beam waist, i.e.,

$$M_{eq1a} := M5 \cdot M4 \cdot M3 \cdot M2 \cdot M1a , \tag{D.8}$$

$$M_{eq1b} := M5 \cdot M4 \cdot M3 \cdot M2 \cdot M1b , \tag{D.9}$$

and

$$M_{eq1c} := M5 \cdot M4 \cdot M3 \cdot M2 \cdot M1c . \tag{D.10}$$

Numerical evaluation of Eqs D.8 through D.10 results in the following:

$$M_{eq1a} = \begin{pmatrix} -2.648 & -0.035 \\ 22.963 & -0.07 \end{pmatrix} , \tag{D.11}$$

$$M_{eq1b} = \begin{pmatrix} -2.648 & -0.026 \\ 22.963 & -0.154 \end{pmatrix} , \tag{D.12}$$

and

$$M_{eq1c} = \begin{pmatrix} -2.648 & -7.223\times 10^{-3} \\ 22.963 & -0.315 \end{pmatrix} . \tag{D.13}$$

The *q*-value is determined at the waist location using the beam waist radii. By definition, the curvature must be infinite at the beam waist, which yields

$$INVq1a := \frac{-MSQ_{0,0}\cdot\lambda\cdot\sqrt{-1}}{\pi\cdot\left(\omega P_{0,0}\right)^2} , \tag{D.14}$$

and

$$q1a := \frac{1}{INVq1a} . \tag{D.15}$$

For an input power of 6.5 kW, this results in the following complex beam parameter value at the measurement plane

$$q1a = 6.402i\times 10^{-3} .$$

The same procedure is followed to determine the complex beam parameters for input powers of 12.5 kW and 16.5 kW, resulting in

$$INVq1b := \frac{-MSQ_{6,0}\cdot\lambda\cdot\sqrt{-1}}{\pi\cdot\left(\omega P_{6,0}\right)^2} , \tag{D.16}$$

$$q1b := \frac{1}{INVq1b} , \tag{D.17}$$

$$q1b = 7.952i\times 10^{-3} ,$$

$$\mathrm{INVq1c} := \frac{-\mathrm{MSQ}_{10,0}\cdot\lambda\cdot\sqrt{-1}}{\pi\cdot\left(\omega\mathrm{P}_{10,0}\right)^2} \quad , \tag{D.18}$$

$$\mathrm{q1c} := \frac{1}{\mathrm{INVq1c}} \quad , \tag{D.19}$$

and

$$\mathrm{q1c} = 6.26\mathrm{i}\times 10^{-3} \quad . \tag{D.20}$$

The *q*-value as determined at the waist location measured by the FocusMonitor is propagated through the optical system to the AR mirror. This is performed for each chosen waist size using the appropriate equivalent matrices shown in Eqs D.8 through D.10. The propagation of the *q*-value is accomplished using

$$\mathrm{q2a} := \frac{\mathrm{Meq1a}_{0,0}\cdot\mathrm{q1a} + \mathrm{Meq1a}_{0,1}}{\mathrm{Meq1a}_{1,0}\cdot\mathrm{q1a} + \mathrm{Meq1a}_{1,1}} \quad , \tag{D.21}$$

$$\mathrm{q2b} := \frac{\mathrm{Meq1b}_{0,0}\cdot\mathrm{q1b} + \mathrm{Meq1b}_{0,1}}{\mathrm{Meq1b}_{1,0}\cdot\mathrm{q1b} + \mathrm{Meq1b}_{1,1}} \quad , \tag{D.22}$$

and

$$\mathrm{q2c} := \frac{\mathrm{Meq1c}_{0,0}\cdot\mathrm{q1c} + \mathrm{Meq1c}_{0,1}}{\mathrm{Meq1c}_{1,0}\cdot\mathrm{q1c} + \mathrm{Meq1c}_{1,1}} \quad . \tag{D.23}$$

The *q*-values at the AR mirror obtained from Eqs D.21 through D.23 are then evaluated to be

$$\mathrm{q2a} = 5.652\times 10^{-5} + 0.241\mathrm{i} \quad , \tag{D.24}$$

$$\mathrm{q2b} = 2.184\times 10^{-3} + 0.14\mathrm{i} \quad , \tag{D.25}$$

and

$$q2c = -8.899\times 10^{-4} + 0.052i \quad . \tag{D.26}$$

Using the calculated complex beam parameter values at the AR mirror, it is then possible to determine the beam waist radii for each pump power as

$$\omega_{oa} := \sqrt{\frac{-MSQ_{0,0}\cdot\lambda}{\pi\cdot\left(Im\left(\frac{1}{q2a}\right)\right)}} \quad , \tag{D.27}$$

$$\omega_{ob} := \sqrt{\frac{-MSQ_{6,0}\cdot\lambda}{\pi\cdot\left(Im\left(\frac{1}{q2b}\right)\right)}} \quad , \tag{D.28}$$

and

$$\omega_{oc} := \sqrt{\frac{-MSQ_{10,0}\cdot\lambda}{\pi\cdot\left(Im\left(\frac{1}{q2c}\right)\right)}} \quad . \tag{D.29}$$

The resultant beam sizes at the AR mirror are summarized in Table D.2.

Table D.2. Beam sizes at AR mirror.

6.5 kW input power	$\omega_{oa} = 2.006\times 10^{-3}$	m
12.5 kW input power	$\omega_{ob} = 1.596\times 10^{-3}$	m
16.5 kW input power	$\omega_{oc} = 6.96\times 10^{-4}$	m

The resonator is defined, and the Nd:YAG crystal modeled as a stable quadratic duct with two plane mirrors on either side. Matrix formulation for the stable quadratic duct was obtained from Siegman (1986). A graphical representation of the resonator model used is shown in Fig. D.2

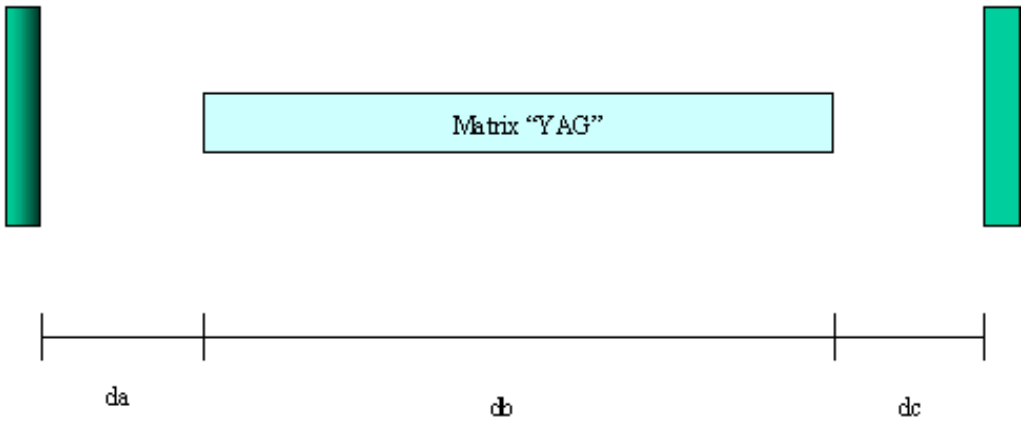

Fig. D.2. Resonator nomenclature.

The required dimensions and constants for subsequent calculations are listed in Table D.3.

Table D.3. Resonator constant values.

Distance from AR mirror to crystal	da = 0.161	m
Distance from HR mirror to crystal	dc = da	m
Length of crystal	db = 0.178	m
Index of refraction	$n_0 = 1.82$	

In order to make the quadratic duct model simpler to analyze the following substitutions were made. The transverse derivative *b*, is defined as

$$b(n_2) := \sqrt{\frac{n_2}{n_0}} \quad , \tag{D.30}$$

and is related to the characteristic focal length β by

$$b = \frac{2}{\beta} \quad . \tag{D.31}$$

Therefore, the characteristic focal length of the crystal β, can be defined in terms of the index of refraction, n_0, and the downward curvature, n_2 (Schlueter and Markille, 2002). The additional factor of 4 arises from the definition presented by Ifflaender (2001), i.e,

$$\beta^2 = 4\,\frac{n_0}{n_2} \quad . \tag{D.32}$$

The matrix representing a one way pass through the YAG crystal that is modeled as a stable quadratic duct and is defined in terms of the characteristic focal length β is

$$YAG(\beta) := \begin{bmatrix} \cos\left(\frac{2}{\beta}\cdot db\right) & \left(\frac{2}{\beta}\cdot n_0\right)^{-1}\cdot\sin\left(\frac{2}{\beta}\cdot db\right) \\ -n_0\cdot\frac{2}{\beta}\cdot\sin\left(\frac{2}{\beta}\cdot db\right) & \cos\left(\frac{2}{\beta}\cdot db\right) \end{bmatrix} . \tag{D.33}$$

The corresponding distances from the crystal to each mirror are defined by the following ABCD matrices:

$$Mx := \begin{pmatrix} 1 & da \\ 0 & 1 \end{pmatrix} , \tag{D.34}$$

and

$$My := \begin{pmatrix} 1 & dc \\ 0 & 1 \end{pmatrix} . \tag{D.35}$$

The equivalent matrix for a round trip through the resonator is then determined by

$$M_{res}(\beta) := Mx\cdot YAG(\beta)\cdot My\cdot My\cdot YAG(\beta)\cdot Mx \quad . \tag{D.36}$$

Using a guess value for the characteristic focal length based on values published in Ifflaender (2001), i.e.,

$$\beta := 0.37 \quad , \tag{D.37}$$

the equivalent matrix representing the resonator shown in Eq. D.36 can be numerically evaluated to be

$$M_{res}(\beta) = \begin{pmatrix} 0.059 & -0.085 \\ 11.747 & 0.059 \end{pmatrix} \quad . \tag{D.38}$$

Knowing that the *q*-value must self-repeat after a round trip through the resonator, equations are defined that will be used in subsequent calculations to ensure that this requirement is adhered to. One equation is required for each input power level, i.e.,

$$Q2a(\beta) := \frac{M_{res}(\beta)_{0,0} \cdot q2a + M_{res}(\beta)_{0,1}}{M_{res}(\beta)_{1,0} \cdot q2a + M_{res}(\beta)_{1,1}} \quad , \tag{D.39}$$

$$Q2b(\beta) := \frac{M_{res}(\beta)_{0,0} \cdot q2b + M_{res}(\beta)_{0,1}}{M_{res}(\beta)_{1,0} \cdot q2b + M_{res}(\beta)_{1,1}} \quad , \tag{D.40}$$

and

$$Q2c(\beta) := \frac{M_{res}(\beta)_{0,0} \cdot q2c + M_{res}(\beta)_{0,1}}{M_{res}(\beta)_{1,0} \cdot q2c + M_{res}(\beta)_{1,1}} \quad . \tag{D.41}$$

Individual solve blocks are defined in MathCad software that will solve for the characteristic focal length of the crystal to ensure a self-repeating complex beam parameter. The initial guess value is defined in Eq. D.37. The solvers employed were the conjugate gradient and Levenberg-Marquardt algorithms. Primarily the Levenberg-Marquardt nonlinear solver was used, however, the solutions obtained by this solver where sometimes grossly different from solutions obtained for adjacent power levels. In these cases the solver was changed to the conjugate gradient method and solutions again followed the established pattern. This effect was primarily prevalent during low input powers and occasionally seen in the unstable region of the resonator. High input powers (>12.5 kW) were all solved using the Levenberg-Marquardt method.

For input power of 6.5 kW, the solve block is setup to solve for β with initial conditions and requirements. The requirement that the q-value is self-repeating after a round trip through the resonator is given by

$$Q2a(\beta) = q2a \quad , \tag{D.42}$$

the MathCad generated solution for β that fulfills the requirement presented in D.42 is obtained from

$$sol := Find(\beta) \quad , \tag{D.43}$$

evaluation leads to

$$sol = 0.541 - 7.744i \times 10^{-5} \quad . \tag{D.44}$$

The matrix defined in Eq. D.39 is then evaluated based on the β value that was obtained in Eq. D.43, shown as

$$Q2a(\beta a) = 5.652\times 10^{-5} + 0.241i \quad . \tag{D.45}$$

The procedure used for the 6.5 kW input power level is followed for the 12.5 kW and 16.5 kW input powers. The MathCad output is shown below.

For input power of 12.5 kW:

Given
$Q2b(\beta) = q2b$
$solb := Find(\beta)$
$solb = 0.417 - 2.231i\times 10^{-3}$
$\beta b := solb$

For input power of 16.5 kW:

Given
$Q2c(\beta) = q2c$
$solc := Find(\beta)$
$solc = 0.351 + 3.995i\times 10^{-4}$
$\beta c := solc$

The calculated characteristic focal length values for each input power are

$$\beta a = 0.541 - 7.744i\times 10^{-5} \quad , \tag{D.46}$$

$$\beta b = 0.417 - 2.231i\times 10^{-3} \quad , \tag{D.47}$$

and

$$\beta c = 0.351 + 3.995i\times 10^{-4} \quad . \tag{D.48}$$

It should be verified that the calculated β value does indeed allow for a self-repeating q-value. The comparison is shown in Table D.4.

Table D.4. Complex beam parameter comparison.

Input power	Original *q*-value	*q*-value based on β
6.5 kW	$q2a = 5.652\times 10^{-5} + 0.241i$	$Q2a(sol) = 5.652\times 10^{-5} + 0.241i$
12.5 kW	$q2b = 2.184\times 10^{-3} + 0.14i$	$Q2b(solb) = 2.184\times 10^{-3} + 0.14i$
16.5 kW	$q2c = -8.899\times 10^{-4} + 0.052i$	$Q2c(solc) = -8.899\times 10^{-4} + 0.052i$

The focal length of the crystal based on the value of the characteristic focal length can be determined using the approximation found in Koechner (1999). Only the real portion of the characteristic focal length β as determined in Eq. D.46 through Eq. D.48 is considered. The approximation for the focal length is

$$f = \frac{\beta^2}{4\, n_0 \cdot L_{rod}} \quad . \tag{D.49}$$

The length of the crystal is defined as

$$L_{rod} := .178 \ \ m \quad . \tag{D.50}$$

The individual focal lengths of the crystal based on the input power are determined using

$$f1 := \frac{Re(\beta a)^2}{4 \cdot n_0 \cdot L_{rod}} \quad , \tag{D.51}$$

$$f2 := \frac{Re(\beta b)^2}{4 \cdot n_0 \cdot L_{rod}} \quad , \tag{D.52}$$

and

$$f3 := \frac{Re(\beta c)^2}{4 \cdot n_0 \cdot L_{rod}} \quad . \tag{D.53}$$

The focal lengths calculated in Eqs D.51 through D.53 are summarized in Table .5.

Table D.5. Power dependent focal length.

Input power	Focal length	Unit
6.5 kW	f1 = 0.226	m
12.5 kW	f2 = 0.134	m
16.5 kW	f3 = 0.095	m

A vector is defined that will allow for the incremental propagation of the beam from the AR mirror to the crystal, this will allow for the beam size to be plotted as a function of position within the resonator in later calculations.

$$j := 1..21 \ , \tag{D.54}$$

$$x1_j := \frac{da \cdot (j - 1)}{20} \ . \tag{D.55}$$

The vector is then defined as the equivalent ABCD matrix as

$$section4_j := \begin{pmatrix} 1 & x1_j \\ 0 & 1 \end{pmatrix} \ . \tag{D.56}$$

The vector defined in Eq. D.56 is then used to incrementally propagate the q-value determined at the AR mirror to the surface of the crystal, i.e.,

$$q_{AR\_roda_j} := \frac{(section4_j)_{0,0} \cdot q2a + (section4_j)_{0,1}}{(section4_j)_{1,0} \cdot q2a + (section4_j)_{1,1}} \ , \tag{D.57}$$

$$q_{AR\_rodb_j} := \frac{(section4_j)_{0,0} \cdot q2b + (section4_j)_{0,1}}{(section4_j)_{1,0} \cdot q2b + (section4_j)_{1,1}} \ , \tag{D.58}$$

and

$$q_{AR\_rodc_j} := \frac{(section4_j)_{0,0} \cdot q2c + (section4_j)_{0,1}}{(section4_j)_{1,0} \cdot q2c + (section4_j)_{1,1}} \ . \tag{D.59}$$

The beam size can be determined using the results of Eqs D.57 through D.59 and

$$\omega_{Ffacea_j} := \sqrt{\frac{-\lambda \cdot MSQ_{0,0}}{\pi \cdot \left(Im\left(\frac{1}{q_{AR\_roda_j}} \right) \right)}} , \tag{D.60}$$

$$\omega_{Ffaceb_j} := \sqrt{\frac{-\lambda \cdot MSQ_{6,0}}{\pi \cdot \left(Im\left(\frac{1}{q_{AR\_rodb_j}} \right) \right)}} , \tag{D.61}$$

and

$$\omega_{Ffacec_j} := \sqrt{\frac{-\lambda \cdot MSQ_{10,0}}{\pi \cdot \left(Im\left(\frac{1}{q_{AR\_rodc_j}} \right) \right)}} . \tag{D.62}$$

In order to model the behavior of the beam through the crystal, the *q*-value determined at the front face of the crystal must be propagated through the remainder of the crystal. This will be accomplished using the characteristic focal length β that was calculated previously. The "db" term within the matrix that represents the length of the crystal was replaced by a vector to enable the beam to be propagated incrementally through the crystal.

The *q*-value is first determined at the front face of the crystal as

$$q2_{Froda} := \frac{q2a \cdot Mx_{0,0} + Mx_{0,1}}{q2a \cdot Mx_{1,0} + Mx_{1,1}} , \tag{D.63}$$

$$q2_{Frodb} := \frac{q2b \cdot Mx_{0,0} + Mx_{0,1}}{q2b \cdot Mx_{1,0} + Mx_{1,1}} , \tag{D.64}$$

and

$$q2_{Frodc} := \frac{q2c \cdot Mx_{0,0} + Mx_{0,1}}{q2c \cdot Mx_{1,0} + Mx_{1,1}} \quad . \tag{D.65}$$

The vector describing the incremental propagation of the beam through the crystal is defined as

$$k := 1..21 \qquad x2_k := \frac{db \cdot (k-1)}{20} \quad . \tag{D.66}$$

The value calculated for the characteristic focal length is then substituted in the matrix representing the Nd:YAG crystal given by Eq. D.33. The calculation procedure is outlined in detail for an input power of 6.5 kW as shown by Eqs D.67 through D.69 The same procedure is followed for other input power values.

The characteristic focal length value defined in Eq. D.46 is substituted in to the matrix representing the Nd:YAG crystal to obtain

$$YAG_{roda_k} := \begin{bmatrix} \cos\left(\frac{2}{\beta} \cdot x2_k\right) & \left(\frac{2}{\beta} \cdot n_0\right)^{-1} \cdot \sin\left(\frac{2}{\beta} \cdot x2_k\right) \\ -n_0 \cdot \frac{2}{\beta} \cdot \sin\left(\frac{2}{\beta} \cdot x2_k\right) & \cos\left(\frac{2}{\beta} \cdot x2_k\right) \end{bmatrix} . \tag{D.67}$$

The q-value determined at the front face of the crystal given by Eq. D.63 is propagated through the crystal using

$$Q_{YAGroda_k} := \frac{\left(YAG_{roda_k}\right)_{0,0} \cdot q2_{Froda} + \left(YAG_{roda_k}\right)_{0,1}}{\left(YAG_{roda_k}\right)_{1,0} \cdot q2_{Froda} + \left(YAG_{roda_k}\right)_{1,1}} \quad . \tag{D.68}$$

The beam size is calculated using the results from Eq. D.68 to get

$$\omega_{Rfacea_k} := \sqrt{\frac{-\lambda \cdot MSQ_{0,0}}{\pi \cdot \left(Im\left(\frac{1}{Q_{YAGroda_k}}\right)\right)}} \quad . \tag{D.69}$$

The procedure remains the same for other input power levels. In the following, the MathCad output is shown for input power levels of 12.5 kW, and 17.5 kW.

For input power of 12.5 kW:

$$\beta = 0.417 - 2.231i \times 10^{-3} \quad , \tag{D.70}$$

$$YAG_{rodb_k} := \begin{bmatrix} \cos\left(\frac{2}{\beta}\cdot x2_k\right) & \left(\frac{2}{\beta}\cdot n_0\right)^{-1}\cdot\sin\left(\frac{2}{\beta}\cdot x2_k\right) \\ -n_0\cdot\frac{2}{\beta}\cdot\sin\left(\frac{2}{\beta}\cdot x2_k\right) & \cos\left(\frac{2}{\beta}\cdot x2_k\right) \end{bmatrix} , \tag{D.71}$$

$$Q_{YAGrodb_k} := \frac{\left(YAG_{rodb_k}\right)_{0,0}\cdot q2_{Frodb} + \left(YAG_{rodb_k}\right)_{0,1}}{\left(YAG_{rodb_k}\right)_{1,0}\cdot q2_{Frodb} + \left(YAG_{rodb_k}\right)_{1,1}} \quad , \tag{D.72}$$

and

$$\omega_{Rfaceb_k} := \sqrt{\frac{-\lambda\cdot MSQ_{6,0}}{\pi\cdot\left(\mathrm{Im}\left(\frac{1}{Q_{YAGrodb_k}}\right)\right)}} \quad . \tag{D.73}$$

For input power of 16.5 kW:

$$\beta = 0.351 + 3.995i \times 10^{-4} \quad , \tag{D.74}$$

$$YAG_{rodc_k} := \begin{bmatrix} \cos\left(\frac{2}{\beta}\cdot x2_k\right) & \left(\frac{2}{\beta}\cdot n_0\right)^{-1}\cdot\sin\left(\frac{2}{\beta}\cdot x2_k\right) \\ -n_0\cdot\frac{2}{\beta}\cdot\sin\left(\frac{2}{\beta}\cdot x2_k\right) & \cos\left(\frac{2}{\beta}\cdot x2_k\right) \end{bmatrix} , \tag{D.75}$$

$$Q_{YAGrodc_k} := \frac{\left(YAG_{rodc_k}\right)_{0,0}\cdot q2_{Frodc} + \left(YAG_{rodc_k}\right)_{0,1}}{\left(YAG_{rodc_k}\right)_{1,0}\cdot q2_{Frodc} + \left(YAG_{rodc_k}\right)_{1,1}} \quad , \tag{D.76}$$

and

$$\omega_{Rfacec_k} := \sqrt{\frac{-\lambda \cdot MSQ_{10,0}}{\pi \cdot \left(Im\left(\frac{1}{Q_{YAGrodc_k}} \right) \right)}} \quad . \tag{D.77}$$

From the rear face of the crystal the *q*-value will also be incrementally propagated to the HR mirror.

Again the vector describing the propagation of the *q*-value to the HR mirror is defined as

$$j := 1 .. 21 \qquad x3_j := \frac{dc \cdot (j - 1)}{20} \quad . \tag{D.78}$$

Defining the vector in terms of an ABCD matrix we get

$$section5_j := \begin{pmatrix} 1 & x3_j \\ 0 & 1 \end{pmatrix} \quad . \tag{D.79}$$

The *q*-value is determined at the rear face of the crystal by directly propagating the *q*-value determined at the front face in Eq. D.63 through the length of the crystal as shown by

$$q2_{Rroda} := \frac{YAG(\beta a)_{0,0} \cdot q2_{Froda} + YAG(\beta a)_{0,1}}{YAG(\beta a)_{1,0} \cdot q2_{Froda} + YAG(\beta a)_{1,1}} \quad . \tag{D.80}$$

Propagating the *q*-value from the rear face of the crystal to the HR mirror we obtain

$$q_{plota_j} := \frac{(section5_j)_{0,0} \cdot q2_{Rroda} + (section5_j)_{0,1}}{(section5_j)_{1,0} \cdot q2_{Rroda} + (section5_j)_{1,1}} \quad . \tag{D.81}$$

Using the results from Eq. D.81 the beam size is determined to be

$$\omega_{HRa_j} := \sqrt{\frac{-\lambda \cdot MSQ_{0,0}}{\pi \cdot \left(Im\left(\frac{1}{q_{plota_j}} \right) \right)}} \quad . \tag{D.82}$$

The identical procedure is followed for higher input power values.

For input power of 12.5 kW:

$$q2_{Rrodb} := \frac{YAG(\beta b)_{0,0} \cdot q2_{Frodb} + YAG(\beta b)_{0,1}}{YAG(\beta b)_{1,0} \cdot q2_{Frodb} + YAG(\beta b)_{1,1}} \quad , \tag{D.83}$$

$$q_{plotb_j} := \frac{\left(section5_j\right)_{0,0} \cdot q2_{Rrodb} + \left(section5_j\right)_{0,1}}{\left(section5_j\right)_{1,0} \cdot q2_{Rrodb} + \left(section5_j\right)_{1,1}} \quad , \tag{D.84}$$

and

$$\omega_{HRb_j} := \sqrt{\frac{-\lambda \cdot MSQ_{6,0}}{\pi \cdot \left(Im\left(\frac{1}{q_{plotb_j}}\right)\right)}} \quad . \tag{D.85}$$

For input power of 16.5 kW:

$$q2_{Rrodc} := \frac{YAG(\beta c)_{0,0} \cdot q2_{Frodc} + YAG(\beta c)_{0,1}}{YAG(\beta c)_{1,0} \cdot q2_{Frodc} + YAG(\beta c)_{1,1}} \quad , \tag{D.86}$$

$$q_{plotc_j} := \frac{\left(section5_j\right)_{0,0} \cdot q2_{Rrodc} + \left(section5_j\right)_{0,1}}{\left(section5_j\right)_{1,0} \cdot q2_{Rrodc} + \left(section5_j\right)_{1,1}} \quad , \tag{D.87}$$

and

$$\omega_{HRc_j} := \sqrt{\frac{-\lambda \cdot MSQ_{10,0}}{\pi \cdot \left(Im\left(\frac{1}{q_{plotc_j}}\right)\right)}} \quad . \tag{D.88}$$

The results of the calculations in Eqs D.60 through D.62 are plotted in Fig. D.3.

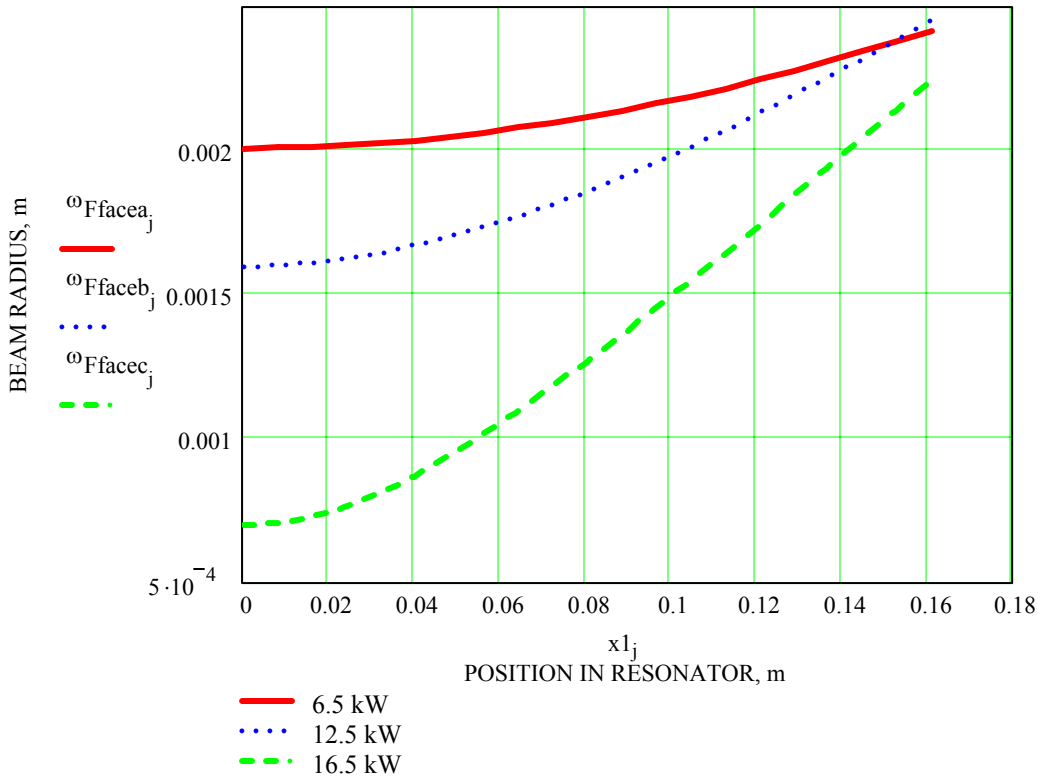

Fig. D.3. Beam size from AR mirror to front face of crystal.

The results of calculations based on Eqs D.69, D.73, and D.77 are shown in Fig. D.4

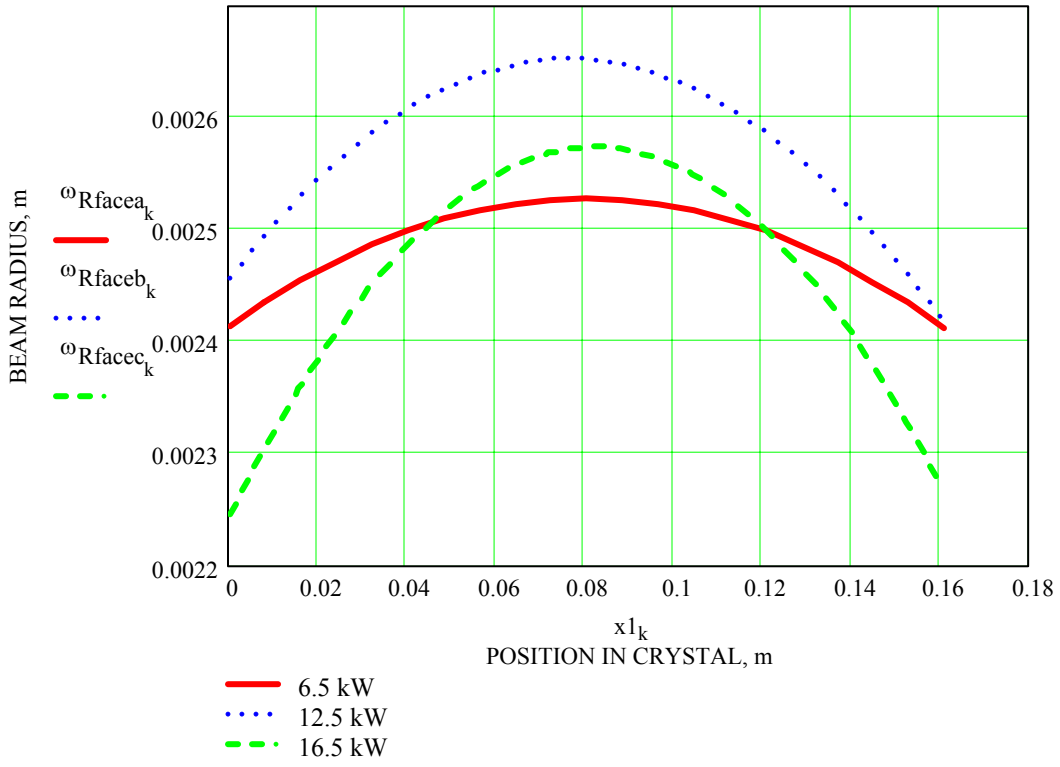

Fig. D.4. Beam size through Nd:YAG crystal.

The results of calculations based on Eqs D.82, D.85, and D.88 are shown in Fig. D.5

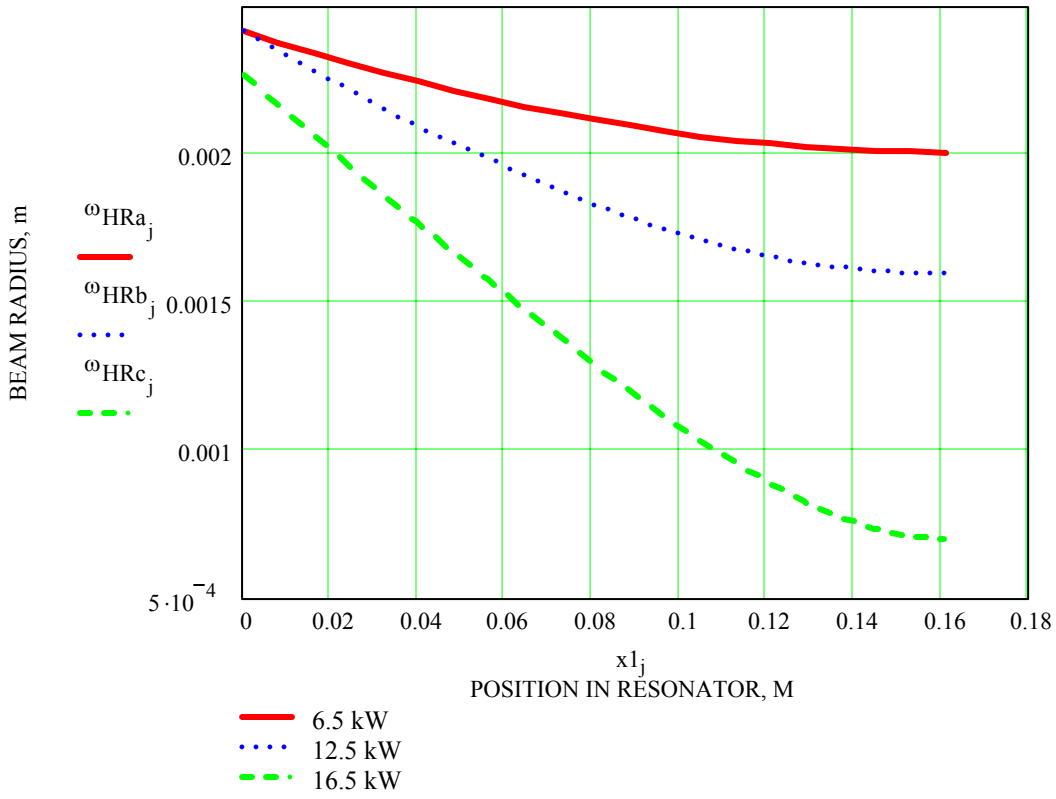

Fig. D.5. Beam size from rear face of crystal to HR mirror.

APPENDIX E. FOCAL LENGTH AND CRYSTAL SENSITIVITY FACTOR CALCULATION

In order to determine the crystal sensitivity factor, the focal length needed to be determined first. In order to accomplish this the complex beam parameter value at the FocusMonitor measuring plane was propagated to the AR mirror. At this point the resonator model was solved for the characteristic focal length, β, using the self-repeating q-value principle. Using the calculated characteristic focal length, the focal length of each crystal was determined. Following this, the crystal sensitivity factor was determined using the calculated power dependent focal lengths. This allowed for the determination of both the focal length and the crystal sensitivity parameter as a function of input power.

The data are presented for a sample crystal, number 261787f, that failed to meet the quality criteria imposed by the YAG production department at TRUMPF. When installed in a laser the crystal exhibited symmetric dips in the beam profile. Thus it was removed from the laser and deemed as unsuitable for 4 kW lasers. The experimental setup is shown in Fig. E.1, and the definition of each variable is presented in Table E.1.

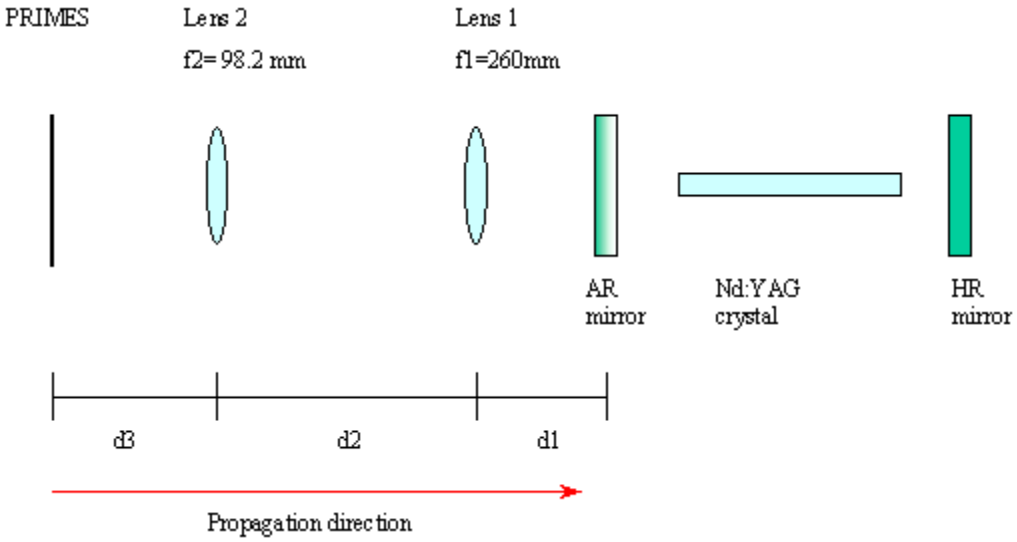

Fig. E.1. Experimental configuration.

Table E.1. Definitions of laser system variables.

Distance from AR mirror to lens 1	d1 = 0.260	m
Distance from lens 1 to lens 2	d2 = 0.9445	m
Focal length of lens 1	f1 = 0.260	m
Focal length of lens 2	f2 = 0.0982	m
Length of resonator	L = 0.5	m

The wavelength of the Nd:YAG laser is

$\lambda := 1.06 \cdot 10^{-6}$ m .

The measured values at the FocusMonitor measuring plane are then defined. The beam radius is expressed in meters, and the distance, d3, from the focusing lens to the FocusMonitor device is expressed in millimeters. All measured values are arranged as arrays to facilitate subsequent calculations.

The beam size, ω_P, beam focusability factor, M^2, and distance from the focusing lens to the FocusMonitor, d3, are defined as follows:

$\omega_P :=$

	0
0	0.000316
1	0.000339
2	0.000357
3	0.000356
4	0.000356
5	0.000376
6	0.000376
7	0.000384
8	0.000368
9	0.000333
10	0.000277
11	0.000238
12	

MSQ :=

	0
0	47.3
1	52.6
2	54.4
3	58.7
4	56.1
5	55.6
6	52
7	53.5
8	48.5
9	39.9
10	34.5
11	29.4
12	

d3 :=

	0
0	101.23
1	100.65
2	100.28
3	99.51
4	98.6
5	98.66
6	97.91
7	97.13
8	95.99
9	94.57
10	93.02
11	91.19
12	

The corresponding ABCD matrices for each component are defined as

$$M2 := \begin{pmatrix} 1 & 0 \\ \frac{-1}{f2} & 1 \end{pmatrix}, \tag{E.1}$$

$$M3 := \begin{pmatrix} 1 & d2 \\ 0 & 1 \end{pmatrix}, \tag{E.2}$$

$$M4 := \begin{pmatrix} 1 & 0 \\ \frac{-1}{f1} & 1 \end{pmatrix}, \tag{E.3}$$

and

$$M5 := \begin{pmatrix} 1 & d1 \\ 0 & 1 \end{pmatrix}. \tag{E.4}$$

Using the measured M^2 data and beam waist radii, the complex beam parameter at the measuring plane can be determined. The procedures outlined below show the calculation of the complex beam parameter for an input power of 6.5 kW. The procedure is repeated for higher power levels. The complex beam parameter is determined using

$$INVq6\_5 := \frac{-MSQ_{0,0} \cdot \lambda \cdot \sqrt{-1}}{\pi \cdot \left(\omega P_{0,0}\right)^2}, \tag{E.5}$$

and

$$q6\_5 := \frac{1}{INVq6\_5}. \tag{E.6}$$

In order to propagate the *q*-value through the optical system prior to the resonator, an additional matrix must be defined that will take into account the varying distance from the measuring plane of the FocusMonitor to the focusing optic. The corresponding ABCD matrix for an input power of 6.5 kW is

$$M6\_5 := \begin{pmatrix} 1 & \frac{d3_{0,0} + 10.5}{1000} \\ 0 & 1 \end{pmatrix}. \tag{E.7}$$

Following the determination of the distance "d3" the equivalent matrix representing the optical system prior to the resonator is determined to be

$$M_{eq6\_5} := M5 \cdot M4 \cdot M3 \cdot M2 \cdot M6\_5 \quad . \tag{E.8}$$

At this point, the complex beam parameter as measured at the FocusMonitor measurement plane and determined by Eq. E.6 is propagated to the AR mirror using

$$q2\_6\_5 := \frac{M_{eq6\_5_{0,0}} \cdot q6\_5 + M_{eq6\_5_{0,1}}}{M_{eq6\_5_{1,0}} \cdot q6\_5 + M_{eq6\_5_{1,1}}} \quad . \tag{E.9}$$

The calculated input power dependent complex beam parameter values at the AR mirror are then equal to

$q2\_values =$

	0
0	$7.143 \cdot 10^{-4} + 0.249i$
1	$7.144 \cdot 10^{-3} + 0.227i$
2	$8.537 \cdot 10^{-4} + 0.208i$
3	$0.026 + 0.194i$
4	$0.024 + 0.168i$
5	$4.427 \cdot 10^{-3} + 0.165i$
6	$-1.375 \cdot 10^{-3} + 0.147i$
7	$-5.482 \cdot 10^{-4} + 0.134i$
8	$-7.327 \cdot 10^{-4} + 0.116i$
9	$-1.474 \cdot 10^{-3} + 0.098i$
10	$0.011 + 0.075i$
11	$7.223 \cdot 10^{-3} + 0.054i$

. (E.10)

Following determination of the complex beam parameter at the AR mirror, the resonator model is established. The Nd:YAG crystal is modeled as a stable quadratic duct with two plane mirrors on either side shown in Fig. E.2. Matrix formulation was obtained from Siegman (1986). Resonator variables are defined in Table E.2.

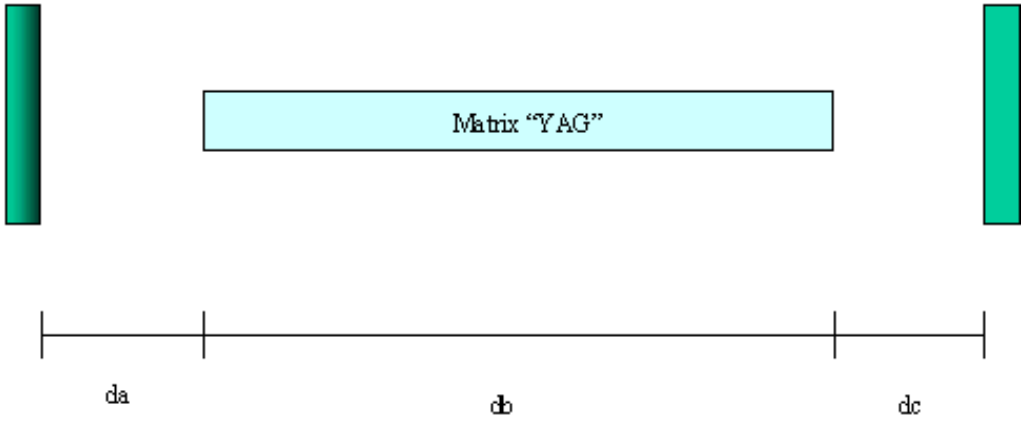

Fig. E.2. Resonator nomenclature.

Table E.2. Resonator constant values.

Distance from AR mirror to crystal	da = 0.161	m
Distance from HR mirror to crystal	dc = da	m
Length of crystal	db = 0.178	m
Index of refraction	$n_0 = 1.82$	

In order to make the quadratic duct model simpler to analyze the following substitutions were made. The transverse derivative *b*, is defined as

$$b(n_2) := \sqrt{\frac{n_2}{n_0}} \quad , \tag{E.11}$$

and can be related to the characteristic focal length β by

$$b = \frac{2}{\beta} \quad . \tag{E.12}$$

Therefore, the characteristic focal length of the crystal β, can be defined in terms of the index of refraction, n_0 and the downward curvature, n_2. The additional factor of 4 arises from the definition presented by Ifflaender (2001), i.e,

$$\beta^2 = 4 \frac{n_0}{n_2} \quad . \tag{E.13}$$

The matrix representing a one way pass through the YAG crystal that is modeled as a stable quadratic duct and is defined in terms of the characteristic focal length β is

$$YAG(\beta) := \begin{bmatrix} \cos\left(\frac{2}{\beta}\cdot db\right) & \left(\frac{2}{\beta}\cdot n_0\right)^{-1}\cdot\sin\left(\frac{2}{\beta}\cdot db\right) \\ -n_0\cdot\frac{2}{\beta}\cdot\sin\left(\frac{2}{\beta}\cdot db\right) & \cos\left(\frac{2}{\beta}\cdot db\right) \end{bmatrix} . \tag{E.14}$$

The corresponding distances from the crystal to each mirror are defined by the following ABCD matrices:

$$Mx := \begin{pmatrix} 1 & da \\ 0 & 1 \end{pmatrix} , \tag{E.15}$$

and

$$My := \begin{pmatrix} 1 & dc \\ 0 & 1 \end{pmatrix} . \tag{E.16}$$

The equivalent matrix for a round trip through the resonator is then determined by

$$M_{res}(\beta) := Mx\cdot YAG(\beta)\cdot My\cdot My\cdot YAG(\beta)\cdot Mx . \tag{E.17}$$

Using a guess value for the characteristic focal length based on values published in Ifflaender (2001), i.e.,

$$\beta := 0.37 , \tag{E.18}$$

the equivalent matrix representing the resonator shown in Eq. E.17 can be numerically evaluated to be

$$M_{res}(\beta) = \begin{pmatrix} 0.059 & -0.085 \\ 11.747 & 0.059 \end{pmatrix} . \tag{E.19}$$

Knowing that the *q*-value must self-repeat after a round trip through the resonator, equations are defined that will be used in subsequent calculations to ensure that this requirement is adhered to. The initial input power of 6.5 kW is used as an example, higher input powers follow the same procedure. One equation is required for each power level, i.e.,

$$Q2\_6\_5(\beta) := \frac{M_{res}(\beta)_{0,0} \cdot q2\_6\_5 + M_{res}(\beta)_{0,1}}{M_{res}(\beta)_{1,0} \cdot q2\_6\_5 + M_{res}(\beta)_{1,1}} \quad . \tag{E.20}$$

Individual solve blocks are defined in the MathCad software that will solve for the characteristic focal length of the crystal to ensure a self-repeating complex beam parameter. The initial guess value is defined in Eq. E.18. The solvers employed were the Conjugate gradient and Levenberg-Marquardt algorithms. Primarily the Levenberg-Marquardt nonlinear solver was used, however, the solutions obtained by this solver where sometimes grossly different from solutions obtained for adjacent power levels. In these case the solver was changed to the conjugate gradient method and solutions again followed the established pattern. This effect was primarily prevalent during low input powers and occasionally seen in the unstable region of the resonator. High input powers (>12.5 kW) were all solved using the Levenberg-Marquardt method.

For an input power of 6.5 kW, the solve block is setup to solve for β with initial conditions and requirements. The requirement that the q-value is self-repeating after a round trip through the resonator is given by

$$Q2\_6\_5(\beta) = q2\_6\_5 \ , \tag{E.21}$$

the MathCAD generated solution for β that fulfills the requirement presented in Eq. E.21 is obtained from

$$sol6\_5 := Find(\beta) \ , \tag{E.22}$$

evaluation leads to

$$sol6\_5 = 0.552 - 9.914i \times 10^{-4} \quad . \tag{E.23}$$

A check is performed to ensure that the complex beam parameter is indeed self-repeating. This is demonstrated by

$$q2\_6\_5 = 7.143 \times 10^{-4} + 0.249i \quad , \tag{E.24}$$

and

$$Q2\_6\_5(\beta 6\_5) = 7.143 \times 10^{-4} + 0.249i \quad . \tag{E.25}$$

The results of the calculations of all tested input power levels to ensure that the original q-values and those calculated using the calculated characteristic focal length β are indeed self repeating are shown as

q2_values =

	0
0	$7.143 \cdot 10^{-4} + 0.249i$
1	$7.144 \cdot 10^{-3} + 0.227i$
2	$8.537 \cdot 10^{-4} + 0.208i$
3	$0.026 + 0.194i$
4	$0.024 + 0.168i$
5	$4.427 \cdot 10^{-3} + 0.165i$
6	$-1.375 \cdot 10^{-3} + 0.147i$
7	$-5.482 \cdot 10^{-4} + 0.134i$
8	$-7.327 \cdot 10^{-4} + 0.116i$
9	$-1.474 \cdot 10^{-3} + 0.098i$
10	$0.011 + 0.075i$
11	$7.223 \cdot 10^{-3} + 0.054i$

, Q_calc =

	0
0	$7.143 \cdot 10^{-4} + 0.249i$
1	$7.144 \cdot 10^{-3} + 0.227i$
2	$8.537 \cdot 10^{-4} + 0.208i$
3	$0.026 + 0.194i$
4	$0.024 + 0.168i$
5	$4.427 \cdot 10^{-3} + 0.165i$
6	$-1.375 \cdot 10^{-3} + 0.147i$
7	$-5.482 \cdot 10^{-4} + 0.134i$
8	$-7.327 \cdot 10^{-4} + 0.116i$
9	$-1.474 \cdot 10^{-3} + 0.098i$
10	$0.011 + 0.075i$
11	$7.223 \cdot 10^{-3} + 0.054i$

.

The calculated values for the characteristic focal length β based on Eq. E.22 are defined in array form as

Beta =

	0
0	0.552
1	0.522
2	0.498
3	0.479
4	0.447
5	0.444
6	0.425
7	0.411
8	0.395
9	0.38
10	0.363
11	0.352

. (E.26)

The focal length of the crystal based on the value of the characteristic focal length can be determined using the approximation found in Koechner (1999). Only the real portion of the characteristic focal length β is considered. The approximation for the focal length is

$$f = \frac{\beta^2}{4\, n_0 \cdot L_{rod}} , \quad \text{(E.27)}$$

and solving for the focal length of the crystal with an input power of 6.5 kW we have

$$f6\_5 := \frac{Re(\beta 6\_5)^2}{4 \cdot n_0 \cdot L_{rod}} \quad . \tag{E.28}$$

The focal length based on the input power to the laser device is defined as an array of values to be

$$focal\_length = \quad . \tag{E.29}$$

	0
0	0.235
1	0.21
2	0.191
3	0.177
4	0.154
5	0.152
6	0.14
7	0.131
8	0.12
9	0.111
10	0.102
11	0.095

The calculation of the crystal sensitivity factor requires the definition of an index that will allow for simplified operation with arrays. In order to determine the crystal sensitivity factor, the difference between each calculated focal length was first determined. Defining the index as

$$i := 10 \qquad h := 1 .. i \quad . \tag{E.30}$$

The difference in focal length correspondent to each change in the input power to the laser is determined by

$$diff\_f_h := focal\_length_h - focal\_length_{h-1} \quad . \tag{E.31}$$

The change in the input power to the laser is determined by

$$diff\_P\_in_h := P\_in_h - P\_in_{h-1} \quad . \tag{E.32}$$

The crystal sensitivity factor is defined by

$$\text{Rod\_sens}_h := \frac{\frac{1}{\text{diff\_f}_h}}{\text{diff\_P\_in}_h \cdot 1000} \quad . \tag{E.33}$$

The variation in the focal length of the laser as calculated using Eq. E.31 is

$$\text{diff\_f}_h = \quad . \tag{E.34}$$

-0.025
-0.019
-0.014
-0.023
$-1.903 \cdot 10^{-3}$
-0.013
$-8.98 \cdot 10^{-3}$
-0.01
$-9.198 \cdot 10^{-3}$
$-9.602 \cdot 10^{-3}$

The crystal sensitivity factor, M^{-1}, is determined using Eq. E.33 and evaluated to be

$$\text{Rod\_sens}_h = \quad . \tag{E.35}$$

	0
0	-0.04
1	-0.053
2	-0.071
3	-0.044
4	-0.526
5	-0.078
6	-0.111
7	-0.098
8	-0.109
9	-0.104

APPENDIX F. CRYSTAL DATA

Crystal ID	*261067*		
Input power	M^2	focal pos. (mm)	waist radius (mm)
6.5	49.5	16.167	0.327
7.5	54.3	16.789	0.343
8.5	54	17.371	0.367
9.5	52.7	18.128	0.376
10.5	55.4	17.975	0.369
11.5	50	18.786	0.37
12.5	54.1	19.545	0.381
13.5	48.5	20.845	0.375
14.5	42.4	22.239	0.345
15.5	36.2	23.908	0.296
16.5	27.5	26.072	0.241
COMMENTS: Max power output; 819W @ 17.06 kW			

Crystal ID	*261127*		
Input power	M^2	focal pos. (mm)	waist radius (mm)
6.5	48.5	16.208	0.328
7.5	52.3	16.673	0.343
8.5	55	17.308	0.364
9.5	51.3	17.733	0.362
10.5	55.7	18.533	0.373
11.5	51	18.954	0.376
12.5	53.1	19.916	0.385
13.5	46.8	20.785	0.381
14.5	39.2	22.638	0.339
15.5	34.4	24.359	0.298
16.5	27.3	26.736	0.225
COMMENTS: Max power output; 842W @ 16.48kW			

Crystal ID	*261126*		
Input power	M^2	focal pos. (mm)	waist radius (mm)
6.5	49.4	16.114	0.318
7.5	50.9	16.545	0.341
8.5	51.7	17.167	0.362
9.5	50.9	17.775	0.36
10.5	52.8	18.474	0.368
11.5	50	19.024	0.373
12.5	53.4	19.797	0.377
13.5	48.3	20.846	0.377
14.5	38.1	22.54	0.341
15.5	33.6	24.378	0.275
16.5	25.3	26.367	0.228
17.5	25.1	27.321	0.208
COMMENTS: Max power output; 798W @ 17.47kW			

Crystal ID	*261133*		
Input power	M^2	focal pos. (mm)	waist radius (mm)
6.5	49.2	16.112	0.323
7.5	52.9	16.617	0.343
8.5	49.9	17.101	0.356
9.5	49.2	17.714	0.351
10.5	56.3	19.364	0.365
11.5	46.6	19.008	0.377
12.5	53	19.68	0.382
13.5	52.9	20.557	0.379
14.5	45.2	22.144	0.355
15.5	37.7	23.467	0.323
16.5	32.3	25.374	0.262
17.5	29.9	26.807	0.221
COMMENTS: Max power output; 783W @ 17.42kW			

Crystal ID *260787f*			
Input power	M^2	focal pos. (mm)	waist radius (mm)
6.5	47.3	15.767	0.316
7.5	52.6	16.349	0.339
8.5	54.4	16.723	0.357
9.5	58.7	17.488	0.356
10.5	56.1	18.402	0.356
11.5	55.6	18.337	0.376
12.5	52	19.091	0.376
13.5	53.5	19.87	0.384
14.5	48.5	21.011	0.368
15.5	39.9	22.427	0.333
16.5	34.5	23.976	0.277
17.5	29.4	25.815	0.238
COMMENTS: Max power output; 752W @ 17.62kW. Produced bad beam shape			

Crystal ID *260296f*			
Input power	M^2	focal pos. (mm)	waist radius (mm)
6.5	48	15.983	0.312
7.5	52.6	16.5	0.344
8.5	54.1	17.136	0.365
9.5	51	17.426	0.362
10.5	55.6	17.677	0.373
11.5	53.2	18.199	0.381
12.5	49.3	19.076	0.376
13.5	48.4	19.671	0.381
14.5	46.7	20.61	0.371
15.5	40.8	22.192	0.341
16.5	35	23.71	0.294
17.5	25.1	26.293	0.223
COMMENTS: Max power output; 774W @ 18.13kW. Produced bad beam shape			

Crystal ID *260489f*			
Input power	M^2	focal pos. (mm)	waist radius (mm)
6.5	43.8	16.219	0.312
7.5	49.6	16.479	0.339
8.5	51.9	17.731	0.345
9.5	53.3	17.675	0.359
10.5	52.4	17.925	0.371
11.5	52.4	18.252	0.375
12.5	48.7	18.783	0.373
13.5	50.8	19.416	0.383
14.5	49.4	20.213	0.373
15.5	44.3	21.568	0.353
16.5	38	23.149	0.324
17.5	30.7	25.051	0.259
COMMENTS: Max power output; 744W @ 17.98kW			

Crystal ID *252835f*			
Input power	M^2	focal pos. (mm)	waist radius (mm)
6.5	45	15.761	0.305
7.5	47.8	16.46	0.334
8.5	53	16.829	0.351
9.5	45.7	17.544	0.368
10.5	52.7	17.561	0.369
11.5	47.1	17.775	0.376
12.5	47.6	18.746	0.374
13.5	48.6	19.732	0.375
14.5	44.7	20.487	0.367
15.5	42.6	21.606	0.344
16.5	35.3	23.17	0.291
COMMENTS: Max power output; 699W @ 17.40kW			